



# **Electrochemical and Spectroscopic Analysis of Collagen Films and Lipid Bilayers on Biomaterial Surfaces**

Von der Fakultät für Mathematik und Naturwissenschaften  
der Carl von Ossietzky Universität Oldenburg  
zur Erlangung des Grades und Titels eines

Doktors der Naturwissenschaften (Dr. rer. nat.)

angenommene Dissertation

von

Dipl.-Chem. Michael Ahlers

geboren am 08. Juli 1983 in Bremen

Oldenburg, March 20, 2013



This work was carried out from February 2009 to January 2013 at the Carl von Ossietzky University of Oldenburg, Faculty of Mathematics and Science, Center of Interface Science (CIS), Department of Pure and Applied Chemistry. It was financed by the DFG grant BR 3961/21 with Dr. Izabella Brand as the principal investigator and under the supervision of Prof. Dr. Gunther Wittstock.

Gutachter:	Prof. Dr. Gunther Wittstock
Zweitgutachter:	Prof. Dr. Thorsten Klüner
Zusätzliches Gutachten:	Dr. Izabella Brand
Tag der Disputation:	15. März 2013



## Abstract

Upon implantation of a biomaterial into the human body, a cascade of subsequent reactions takes place at the implant surface. One crucial step towards biointegration is the adsorption of proteins. This thesis aims at the development of a stable and relatively simple system to model the native protein film on a biomaterial surface under the influence of electric fields. Collagen was chosen as the adsorbing protein and gold as the substrate material. Capacitance measurements, polarization modulation infrared reflection absorption spectroscopy (PM-IRRAS), surface plasmon resonance spectroscopy (SPR) and ellipsometry are employed to analyze the stability and structure of adsorbed collagen films.

The adsorbed collagen films are stable in contact with air for weeks and in contact with an electrolyte solution for several hours. The thermal stability of the collagen molecules is strongly enhanced when adsorbed on a gold surface. The expected denaturation of collagen at a temperature of 43 °C does not take place. Even temperatures of up to 50 °C do not lead to changes in the collagen structure.

A potential-dependent incorporation of the electrolyte solution into the adsorbed collagen film is observed. Increasing potentials result in a decrease of the electrolyte content in the collagen film and vice versa. Changing potentials destabilize the collagen films leading to desorption of the otherwise stable molecules from the gold surface at temperatures around 50 °C.

As enhancements of the model system, other substrate materials like Ti or  $\text{TiO}_x\text{C}_y$  are introduced and compared to the gold substrates. They mimic an implant material more closely and it is shown that the adsorption of collagen molecules to the  $\text{TiO}_2$  and  $\text{TiO}_x\text{C}_y$  surfaces is comparable to the adsorption on gold. However, both materials are not very suitable as an electrode material because titanium is covered with an insulating native oxide layer and the  $\text{TiO}_x\text{C}_y$  surfaces are still under development and do not yield reproducible results, yet. The transfer of a DMPC lipid bilayer onto the collagen covered gold surface to simulate the adhesion of a cell membrane is another extension of the model system. It is shown that collagen and DMPC can be detected and analyzed without mutual interference via PM-IRRAS. However, the transferred bilayers are not stable in contact with the electrolyte solution.



# Zusammenfassung

Nach der Implantation eines Biomaterials in den menschlichen Körper findet eine Kette von Folgereaktionen an der Implantatoberfläche statt. Ein wichtiger Reationsschritt in Richtung Biointegration ist die Adsorption von Proteinen. Ziel dieser Doktorarbeit ist die Entwicklung eines stabilen und relativ einfachen Modellsystems für den nativen Proteinfilm auf einer Biomaterialoberfläche unter dem Einfluß elektrischer Felder. Kollagen wurde als das adsorbierende Protein und Gold als das Substratmaterial ausgewählt. Kapazitätsmessungen, Polarisations Modulation Infrarot Reflektions-Absorptionsspektroskopie (PM-IRRAS), Oberflächen Plasmonen Resonanzspektroskopie (SPR) und Ellipsometrie wurden verwendet um die Stabilität und Struktur adsorbierter Kollagenfilme zu analysieren.

Unter Luftkontakt sind die adsorbierten Kollagenfilme für mehrere Wochen stabil, im Kontakt mit einer Elektrolytlösung für mehrere Stunden. Die thermische Stabilität der Kollagenmoleküle ist nach der Adsorption stark erhöht. Eine Denaturierung von adsorbiertem Kollagen, erwartet bei 43 °C, wurde nicht beobachtet. Stattdessen bleiben die Moleküle mindestens bis zu einer Temperatur von 50 °C stabil.

In Abhängigkeit von dem angelegten Potential ändert sich der Gehalt der Elektrolytlösung im Kollagenfilm. Höhere Potentiale resultieren in einem geringeren Elektrolytgehalt und umgekehrt. Zusätzlich wurde eine Destabilisierung des Kollagenfilms bei wechselnden Potentialen einhergehend mit der Desorption der Moleküle bei Temperaturen um 50 °C beobachtet.

Zur Verbesserung des Modellsystems wurden andere Substratmaterialien wie Titania und  $\text{TiO}_x\text{C}_y$  eingeführt und mit Goldoberflächen verglichen. Diese Materialien sind tatsächlichen Implnatatmeterialien ähnlicher und es wurde gezeigt, dass die Adsorption von Kollagen an deren Oberflächen vergleichbar zu der Adsorption an Gold abläuft. Allerdings sind weder Titania noch  $\text{TiO}_x\text{C}_y$  gut als Elektrodenmaterial für elektrochemische Messungen geeignet. Das Titan ist von einer isolierenden Oxidschicht umgeben und  $\text{TiO}_x\text{C}_y$ , ein Material, das sich noch in der Entwicklung befindet, führt noch nicht zu reproduzierbaren Ergebnissen. Zusätzlich werden DMPC Doppelschichten auf die adsorbierten Kollagenfilme übertragen um die Adhäsion von Zellmembranen zu simulieren. Es

wird gezeigt, dass Kollagen und DMPC mit Hilfe der PM-IRRAS parallel detektiert und analysiert werden können. Allerdings sind die DMPC Doppelschichten nicht stabil im Kontakt mit der Elektrolytlösung.

At this point I want to thank Prof. Dr. Gunther Wittstock and Dr. Izabella Brand for the opportunity to do research in a fascinating field of science with clear connections to applied sciences. Their never ceasing support for the presentation and discussion of my work at conferences as well as new ideas for continuing research was a great help during my studies.

I also want to thank my former and my current group members for the productive atmosphere and many inspiring conversations.

Special thank are addressed to Nicolas Stein, Laurent Broch and Al Saleh Keita from the University of Metz in France for their help, fruitful discussions and an overall very enjoyable time during my ellipsometry measurements.

I also have to thank Sabine Szunerits for the help with the surface plasmon resonance measurements I carried out during my stay at the University of Lille in France.

Last but not least, I want to thank the Deutsche Forschungsgemeinschaft (DFG) for financial support (BR 3961/21).



„Je n'ai pas besoin de cette hypothèse“

- Pierre S. de Laplace



## Table of Contents

<b>1</b>	<b>Introduction .....</b>	<b>- 1 -</b>
<b>2</b>	<b>Theory and Literature Review .....</b>	<b>- 3 -</b>
2.1	Biomaterials .....	- 3 -
2.2	Biointegration Cascade .....	- 5 -
2.3	Collagen .....	- 6 -
2.3.1	<i>Structure of Collagen.....</i>	<i>- 7 -</i>
2.3.2	<i>Application of Collagen in Research.....</i>	<i>- 9 -</i>
2.4	Ellipsometry .....	- 10 -
2.4.1	<i>Polarization of Light.....</i>	<i>- 11 -</i>
2.4.2	<i>Propagation of Polarized Light.....</i>	<i>- 13 -</i>
2.4.3	<i>Optical Elements.....</i>	<i>- 18 -</i>
2.4.4	<i>Ellipsometric Measurements.....</i>	<i>- 22 -</i>
2.5	Infrared Reflection Absorption Spectroscopy.....	- 23 -
2.5.1	<i>Polarization Modulation Infrared Reflection Absorption Spectroscopy .....</i>	<i>- 27 -</i>
2.5.2	<i>IR Spectroscopy of Proteins.....</i>	<i>- 30 -</i>
<b>3</b>	<b>Experimental Section .....</b>	<b>- 35 -</b>
3.1	Preparation of Collagen Films.....	- 35 -
3.2	Langmuir Blodgett and Langmuir Schaefer Transfer of a DMPC bilayer- -	36
3.3	Preparation of TiO <sub>x</sub> C <sub>y</sub> Surfaces.....	- 39 -
3.4	Ellipsometry .....	- 39 -
3.4.1	<i>Data Evaluation and Used Models.....</i>	<i>- 41 -</i>
3.5	Polarization Modulation Infrared Reflection Absorption Spectroscopy.	- 43 -
3.6	Electrochemical Experiments.....	- 46 -
3.6.1	<i>Alternating Current Voltammetry.....</i>	<i>- 47 -</i>
3.7	Surface Plasmon Resonance Experiments .....	- 48 -

<b>4</b>	<b>Results .....</b>	<b>- 51 -</b>
4.1	Collagen-coated Gold Surfaces Characterized in Air.....	- 51 -
4.1.1	<i>Time-Dependence of Collagen Adsorption on Gold.....</i>	<i>- 51 -</i>
4.1.2	<i>Dependence of Collagen Adsorption on Gold on the Collagen Concentration in the Solution .....</i>	<i>- 54 -</i>
4.1.3	<i>Properties of Collagen Films in Air.....</i>	<i>- 56 -</i>
4.2	Characterization of Collagen Films Adsorbed on Gold in Contact with an Electrolyte Solution .....	- 62 -
4.2.1	<i>Properties of a Collagen Film on Gold in Contact with an Electrolyte Solution at OCP .....</i>	<i>- 63 -</i>
4.2.2	<i>Capacitance and Ellipsometry Measurements of Collagen Films on the Gold Electrode Surface .....</i>	<i>- 66 -</i>
4.2.3	<i>Stability of Collagen Adsorbed on Gold in Contact with an Electrolyte Solution .....</i>	<i>- 69 -</i>
4.2.4	<i>Stability of the Collagen Film on Gold in the Electric Field.....</i>	<i>- 71 -</i>
4.2.5	<i>Model for the Behaviour of a Collagen Film on Gold under the Influence of an Electric Field.....</i>	<i>- 75 -</i>
4.2.6	<i>Thermal Stability of Collagen on Gold.....</i>	<i>- 76 -</i>
4.3	Studies on Collagen/Lipid Bilayer Films on the Gold Electrode Surface-	80
	-	
4.3.1	<i>Formation of the DMPC Monolayer on the Water Surface.....</i>	<i>- 81 -</i>
4.3.2	<i>PM-IRRA Spectra of a DMPC Bilayer on a Gold Surface .....</i>	<i>- 82 -</i>
4.3.3	<i>PM-IRRA Spectra of DMPC-Collagen Films on Gold in Air.....</i>	<i>- 84 -</i>
4.3.4	<i>PM IRRA Spectra of a DMPC-Collagen Film on Gold in Contact with Electrolyte .....</i>	<i>- 87 -</i>
4.4	TiO <sub>2</sub> and TiO <sub>x</sub> C <sub>y</sub> as a Substitute for the Au Substrate .....	- 89 -
<b>5</b>	<b>Conclusion and Outlook.....</b>	<b>- 93 -</b>
<b>6</b>	<b>Bibliography .....</b>	<b>- 97 -</b>
<b>7</b>	<b>Own Publications .....</b>	<b>- 103 -</b>
<b>8</b>	<b>Appendix – Abbreviations and Symbols.....</b>	<b>- 105 -</b>





# 1 Introduction

The application of biomaterials in medicine is widespread. It ranges from cannulae made from stainless steel to titanium or titanium alloy screws and plates for the fixation of bones after fractures and bypass stents or dental implants with ceramics and gold components<sup>[1]</sup>. The most common metallic biomaterials can be classified in three major groups: stainless steels, CoCr alloys and titanium and its alloys. Less common are materials containing gold, nickel or magnesium<sup>[2]</sup>.

Implant materials, made of titanium alloys or stainless steel, are used in every day surgery. The scientific knowledge concerning the processes and interactions that take place when a biomaterial comes into contact with a physiological system was poor when the implant materials were first introduced. For ca. 50 years implant materials made of titanium have been researched to fully understand the interaction of cells or proteins with the biomaterial surface<sup>[3, 4, 5, 6]</sup> and the influence of corrosion on the biointegration process<sup>[7, 8, 9, 10]</sup>. A lot of scientific attention has been focused on the optimization of the implant material surface to increase its biocompatibility. For example, the surface morphology and topography can be changed, meaning increased porosity or roughness for an increased overall surface area<sup>[2, 5]</sup>. Alternatively, an additional protein coating<sup>[6]</sup>, or a thick oxide layer<sup>[11]</sup> can be placed on the biomaterial surface to increase the biocompatibility.

This thesis focuses on the analysis of the changes which occur in a protein film that is adsorbed on a biomaterial surface under the influence of electric fields at different temperatures. These two parameters were selected for several reasons. Due to charges accumulated on lipid and protein molecules a biological interface is exposed to static electric fields in the order of  $10^7$  to  $10^9$  V m<sup>-1</sup><sup>[12]</sup>. Under such high electric fields the structure, orientation and hydration of a molecule may differ from that in the bulk phase<sup>[12, 13]</sup>. The preparation of a biological film on an electrode surface gives the possibility to study these assemblies exposed to physiological electric fields<sup>[13]</sup>. Moreover, movement induced wear can lead to significant local potential differences at a biomaterial interface<sup>[10, 14]</sup>. Little research was conducted so far on the analysis of the influence of an electric field on the structure and stability of adsorbed protein films. However, the understanding of the processes that take place at implant material surfaces

requires the knowledge of the influence electric fields have on adsorbed protein films.

Temperature is a factor that strongly influences the molecular structure and functioning of a protein [ 15, 16, 17]. Usually proteins are stable at temperatures around the body core temperature (~37 °C) and slightly above (up to 41 °C), which corresponds to an increased body temperature due to fever. A further temperature increase (43 °C – 50 °C) would result in most cases in changes in the protein tertiary structure, the so called denaturation. Accordingly, a change in the denaturation temperature of an adsorbed protein film in comparison to the protein in solution allows conclusions concerning changes in the molecular stability [ 18].

However, real physiological systems are very complex; e.g. native protein films formed at an implant surface within the human body depend strongly on the physicochemical surface properties of the biomaterial [ 1, 19]. Various proteins from the extracellular matrix adsorb on the implant surface “*in vivo*”. It is reasonable to abstract to a model system that gives a close resemblance to real systems. The model system used in this thesis consists of a film formed by adsorbed collagen molecules on a gold electrode surface, modeling the biomaterial substrate. Collagen was chosen because it is the most abundant protein in the human body and a major component of native protein films adsorbed on biomaterial surfaces. Although gold is not the most commonly used biomaterial it facilitates electrochemical and optical measurements because of its high conductivity and reflectivity of IR and UV/Vis light [ 20].

The stability of collagen films exposed to changing electric fields was studied. The structure and electrolyte content in the protein assembly in dependence on the applied potential were investigated “*in situ*” by means of infrared reflection absorption spectroscopy and ellipsometry. A potential dependent model of the implant interface was presented and discussed.

Nevertheless, the model system is very simple and at the end of this thesis a section will be dedicated to possible enhancements. Structure and stability of a lipid bilayer, modeling the adhesion of a cell to the protein film in the biointegration cascade, is studied.

## 2 Theory and Literature Review

### 2.1 Biomaterials

Literature provides several similar definitions of “biomaterials”, ranging from a “synthetic material to replace part of a living system or to function in contact with living tissue” [ 21] to the very broad definition of “any substance or combination of substances (other than drugs) synthetic or natural in origin, which can be used for a period of time, as a whole or as part of a system, which treats, augments or replaces any tissue, organ or function of the body” [ 22, 23]. Another definition is given by the Consensus Conference of the European Society for Biomaterials: a biomaterial is “a nonviable material used in a medical device, intended to interact with biological systems” [ 24]. These definitions cover a wide range of materials and it is not surprising that biomaterial research and development is an interdisciplinary endeavor. Materials science and engineering focus on the processing of these materials: the casting, composition, surface treatments. Chemistry and physics are necessary to understand the material properties: Conductivity, zeta potential, mechanical properties. On the other hand chemical and biological techniques are used to analyze the interaction of the material with physiological systems: formation of passivizing oxide layers, protein and cell adsorption, tissue growth. And finally the clinical studies convert all the information to medical applications.

Table 1 shows an overview of the most important medical applications of biomaterials and the used substances. The different categories correspond to different requirements besides biocompatibility that the applied biomaterials have to fulfill. Cardiovascular implants interact with blood and soft tissue and e.g. must be non-thrombogenic. Dental implants need a high mechanical stability and must be compatible to tooth enamel. Soft tissue implants on the other hand have to be elastic and true to the touch. Metals and alloys are usually used for orthopedic implants because they can be designed isoelastic to bone tissue. Ophthalmic implants need completely different properties like transparency to visible light.

**Table 1:** Biomaterial Applications [ 1, 23, 25, 26, 27]

<i>Application</i>	<i>Biomaterials</i>	<i>Remarks</i>
<b>Cardiovascular implants</b>		
Heart valves	Pyrolytic carbon, CoCr alloys, Titanium	Materials must be non thrombogenic Replace diseased heart valves
Pacemakers	Stainless steel, silicone rubber	Maintain heart rhythm
Vascular grafts	Polyurethanes, silicone rubber, Teflon, Hema-coated polymers, heparin coatings	Cure vascular disease
Stents	Ti, Ta, shape memory alloys (NiTi)	Open tiny arteries
Blood oxygenators	Polycarbonate and silicone	Replace the gas transfer function of the natural lungs during surgery
<b>Dental implants</b>		
Tooth replacement	Stainless steel, CoCrMo alloys, Ti, Ti alloys, bioglass	Replaces diseased, damaged, or loosened teeth
<b>Soft tissue implants</b>		
Breast prosthesis	Silicones	Augment or redefine the tissue
Artificial skin: nose, chin, other prostheses	Hydrogels, collagen	Replace lost soft tissue
<b>Ophthalmic implants</b>		
Contact lenses	Hydrogels, acrylics, silicones,	Improve vision
Intraocular lenses	Hydrogels, acrylics, silicones,	Replace natural lens with degraded vision
<b>Orthopedic Prostheses</b>		
Hip, Knee, Shoulder	Stainless steel, CoCr alloys, Ti, TiAlV alloy	Reconstruct and repair bony defects
Fixation	PMMA	
<b>Biotechnology</b>		
Sensors	Semiconductors	Diagnostics
Implanted batteries	Metals and semionductors	Drive implant devices
Electrodes	Pt, Ti, Au, Ta	Diagnostics, protein immobilization, cell function
Lab-on-a-chip	Glass, semiconductor, metals	Diagnostics

## 2.2 Biointegration Cascade

At the interface between biomaterial and body fluid several processes take place that ultimately lead to the integration of the biomaterial into the human body and thus can be called the biointegration cascade (Fig. 1). The first event that happens immediately when an implant is brought into contact with a human host is the chemisorption of water and the resulting formation of OH-groups at the biomaterial surface [ 28]. That process is followed by the slightly slower and electrostatically driven adsorption of ions onto the surface. Proteins are the next to adsorb on the implant surface (sometimes also called immobilization). The forces behind this process are usually neither the formation of chemical bonds nor electrostatic interactions but the dehydration of the protein and subsequent increase in entropy. Cell adhesion on the other hand is not determined by interactions between the cell and the biomaterial, instead the cells form bonds to the adsorbed proteins at the interface [ 1]. Finally, the immobilized cells start to proliferate and build tissues; the integration into a human host is successful.

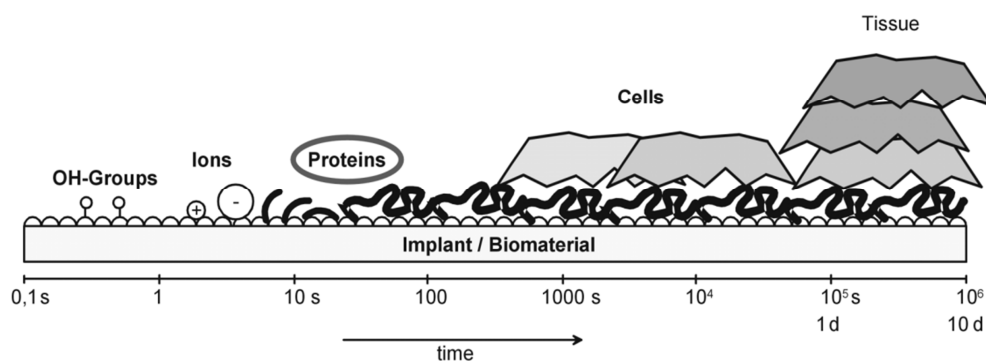


**Figure 1:** Scheme of the processes that take place on a biomaterial surface in contact with the human body. The processes are plotted in dependence of the time dimension in which they take place. (unpublished, with kind permission of D. Scharnweber, TU Dresden, Germany)

In order to study the complex biointegration process, a model system shall be used (Fig. 2). Important parameters, which have to be taken into account, are the electrolyte composition and pH, as well as the overall temperature of the system. Additionally, this thesis is focused on the influence of electric fields. The substrate biomaterial must be inert in contact with a human body and, for analytical purposes, well suited for electrochemical and spectroscopic measurements. Due to its high conductivity and reflectivity of IR and UV/Vis

light gold was chosen as the substrate material <sup>[ 20]</sup>. The chosen protein, collagen, is the most abundant protein in the human body as well as the main component of the extracellular matrix and native protein films on biomaterial surfaces..

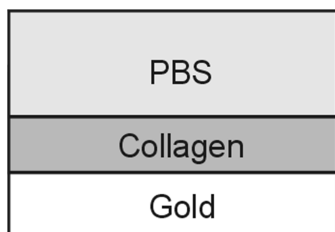


**Figure 2:** Proposed model system made of a gold substrate, a PBS bulk solution containing collagen and an adsorbed collagen film at the interface.

## 2.3 Collagen

Collagen is the most abundant protein in the human body. It is a major component of the extracellular organic matrix as well as of bone and skin tissue. Until now 28 different types of collagen have been identified (collagen I – collagen XXVIII) <sup>[ 29,30]</sup> and can be classified into several species (Tab. 2). Among those species the fibrillar (or fibril-building) collagens are characterized most extensively. In this thesis the fibrillar collagen type I is used. It is the organic compound of bone tissue and makes up the largest fraction of human body collagen <sup>[ 31]</sup>. Especially implants in contact with bone tissue, like hip joints and surgical stents and screws, are exposed to collagen I adsorption. Although collagen VII is called the anchoring collagen, it is not significantly involved in implant body interaction. The name stems from the function of collagen VII as an anchor between the epidermis and dermis of the skin <sup>[ 32]</sup>.

**Table 2:** Classification of collagen in basic species and their corresponding types. <sup>[ 30]</sup>

<i>Species</i>	<i>Type</i>
Fibrillar collagen	Collagen type I, II, III, V and XI
Network building collagen	Collagen type IV, VIII, X
Fibril associated collagen	Collagen type IX, XII, XIV, XXII
Transmembrane collagen	Collagen type XIII, XVII, XXIII, XXV
Anchoring collagen	Collagen type VII

### 2.3.1 Structure of Collagen

One collagen molecule, also called tropocollagen, consists of three helical polypeptide chains that form a semiflexible triple helical tertiary structure (Fig. 3) [33]. This structure was first elucidated by X-ray fiber diffraction studies on native collagen [34, 35, 36, 37] and later confirmed through X-ray crystallographic studies on synthetic collagen-like peptides [38, 39, 40, 41]. The triple helix consists of three left-handed ( $\alpha$ )-helices that are supercoiled in a right-handed manner. Collagen I forms fibrils with a periodicity of 64 nm [37]. On the amino acid chain level the most significant feature is the regularly repeating sequence Gly-X-Y, with peptide X often being proline (Pro) and Y often being hydroxyproline (Hyp) [42]. The glycine (Gly) present at every third position promotes the helical secondary structure of collagen. A higher Hyp content results in an increased stability of the triple helix [18]. The helices are stretched too far for any intrahelical interactions on the amino acid chain level [31, 37]. Regularly appearing interhelical H-bonds can only be formed between the Gly amine of one chain and the carbonyl of the amino acid in X-position of another chain in the triple helix (Fig. 4) [36, 37, 43]. The molecular weight of one collagen molecule is ca. 285 kDa. Its shape can be described simply as rope-like or spaghetti-like with a length of about 300 nm and a diameter of 1.5 nm [31].

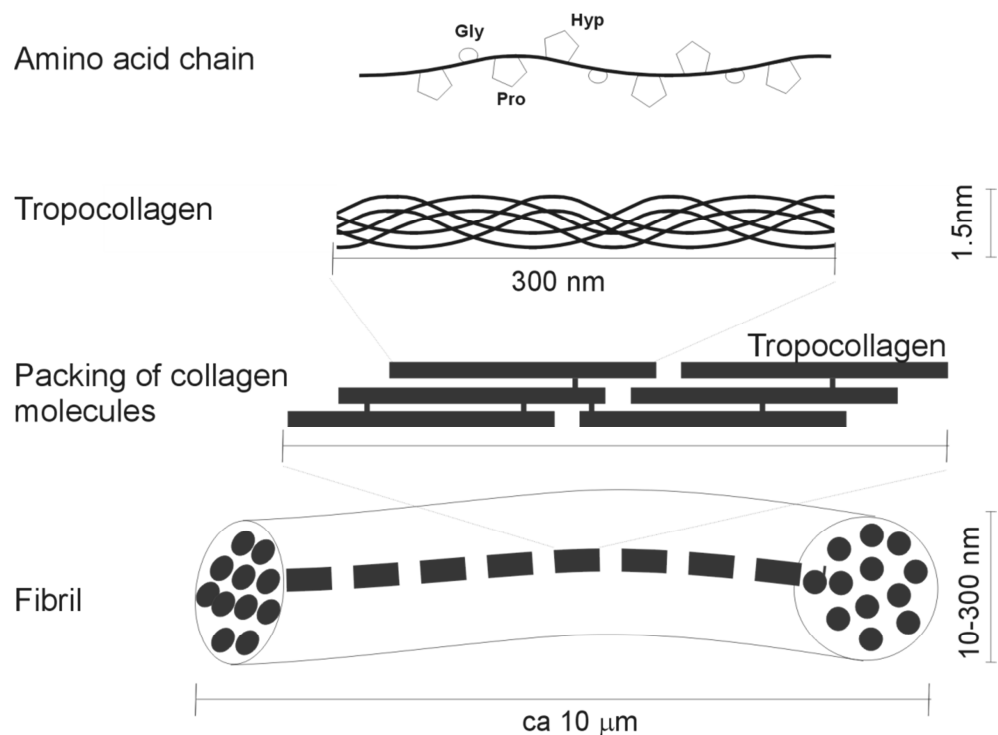


**Figure 3:** Different levels of collagen structure.

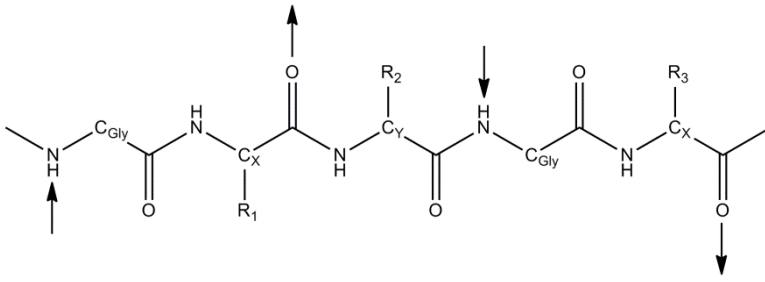


**Figure 4:** Scheme of one polypeptide chain in a collagen molecule. The shown amino acid sequence is Gly-X-Y-Gly-X. Arrows mark the H-bonds to the two other chains.

Under physiological conditions (36 °C, pH = 7.4) tropocollagen assembles in ordered structures to form fibrils (Fig. 3). These fibrils have structural features that cannot be explained by the structure of the tropocollagen. Atomic force microscopy (AFM) images of collagen fibrils show regularly appearing dents on the fibrils (Fig. 5) [ 3]. Hulmes et al. [ 44] developed a model that explained the dents as spaces between the packed molecules. The exact three dimensional packing of the tropocollagen molecules is still unknown and different models from a quasi-hexagonal packing to micro fibrils are discussed in the literature [ 44, 45, 46].

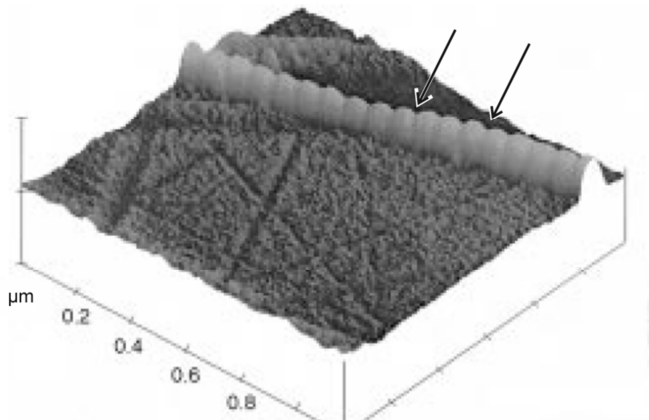


**Figure 5:** AFM image of a collagen fibril. The periodically appearing dents (marked by arrows) are clearly visible [ 3]. (With permission of Kluwer Academic Publishers, © 1999 Kluwer Academic Publishers)

At higher temperatures collagen molecules irreversibly denaturize (43 °C for collagen I) [ 15] leading to at least a partial disintegration of the triple helix. At this state collagen is better known under its trivial name: gelatine. Cooling down

of gelatine does not yield collagen fibrils, instead the single amino acid chains stay separate and solidify<sup>[15]</sup>.

### **2.3.2 Application of Collagen in Research**

Collagen is widely used and investigated in research. The CAPLUS chemical abstracts database records over 280 000 entries linked to the keyword “collagen”<sup>[47]</sup>. Due to the wide use of collagen in science it is not possible to give an overview of all its applications. Some selected examples of collagen application in science that are related to the topic of this thesis are presented below.

The structural analysis of collagen molecules and fibrils was discussed in the previous section. The process of fibrillogenesis and the behaviour of the newly formed fibrils in various environments are widely studied<sup>[31, 48, 49, 50]</sup>. Research is also conducted concerning the influence of collagen on the biocompatibility of biomaterials by means of enhanced osteointegration<sup>[51, 52, 53]</sup>. The authors proposed, that a collagen precoating on a biomaterial surface greatly enhances the adhesion and proliferation of bone tissue. Furthermore, the collagen adsorption behavior and film stability on different kinds of surfaces ranging from metal and metal alloy oxides<sup>[31, 54, 55, 56]</sup>, to inorganic crystal layers made of hydroxyapatite<sup>[5]</sup> and mixed hydroxyapatite/protein layers<sup>[57]</sup>, were studied intensely. A more exotic, but intriguing example of the applications of collagen in research is the electrochemically induced synthesis of collagen membranes developed by Baker et al.<sup>[58]</sup>. This study differs from most others in two ways. They did not try to simulate physiological conditions and they used electric fields to manipulate collagen growth. A pH gradient was created between two electrodes by water electrolysis. The collagen molecules in the solution are differently charged depending on pH, and migrate towards the oppositely charged electrode. They traverse the electrolyte solution until a point of zero charge is reached. At this point the collagen molecules stop migrating and agglomerate, ultimately forming a membrane. Some work was done on the influence of an electric field on the process of collagen adsorption<sup>[54]</sup>. However, to the author’s knowledge there is

no study concerning the behaviour of an already adsorbed collagen film under the influence of electric fields.

Collagen has found many applications in biology and medicine. It is applied as an organic matrix for enzyme immobilization <sup>[ 59]</sup> allowing for the localized analysis of active agents at interfaces. It is also used as a scaffold material for cell cultures and tissue engineering <sup>[ 60, 61, 62, 63]</sup>, which in turn are widely used for biological and medical research purposes. Both applications use the very good biocompatibility of collagen to create a quasi-physiological environment. Especially useful for the work with cells is the property of collagen to facilitate cell adhesion and proliferation. Collagen-coated nanoparticles are investigated as drug carriers for medical application <sup>[ 64]</sup>. Again the collagen coating increases the biocompatibility while it functions at the same time as a substrate for drug immobilization. The role of collagen in the human body and connected diseases like, osteogenesis imperfecta <sup>[ 65]</sup>, collagen-disease <sup>[ 66]</sup> and arthritis <sup>[ 67]</sup> is another important field of research.

## 2.4 Ellipsometry

In the late 19<sup>th</sup> century ellipsometry was developed by the German physicist Paul Drude <sup>[ 68]</sup>. This method is based on the change of the polarization state of the perpendicular components of linearly polarized light. If there is a phase shift between the two components the resulting beam is called elliptically polarized, thus the name ellipsometry. It allows analysis of very thin layers (with a thickness of several  $\mu\text{m}$  to a few  $\text{\AA}$ ) assembled on a reflecting solid surface. Ellipsometry became popular in the 1960's together with the development of thin film transistors <sup>[ 69]</sup>. A second important factor for the flourishing of ellipsometry was the upcoming of computers during that time, which allowed for the fast and simple realization of the required calculations.

The following summary of formal representation of light transmission through optical media follows the description of Tompkins, Irene <sup>[ 68]</sup> and Fujiwara <sup>[ 69]</sup> in their textbooks.

## 2.4.1 Polarization of Light

A transverse wave that propagates in the  $z$  direction can be described by the superposition of two perpendicular electric fields  $E_x$  and  $E_y$  corresponding to the  $x$  and  $y$  axes, that depend on time ( $t$ ) and the vertical space coordinate  $z$ :

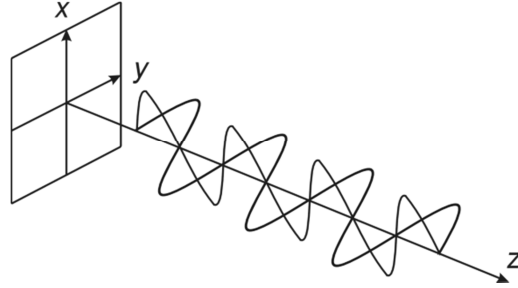


**Figure 6:** Schematic representation of light propagation in a Cartesian coordinate system.

$$\begin{aligned}
 E(z, t) &= E_x(z, t) + E_y(z, t) & (1) \\
 &= [E_{x0} e^{i(\omega t - pz + \delta_x)}]x + [E_{y0} e^{i(\omega t - pz + \delta_y)}]y
 \end{aligned}$$

where  $x$  and  $y$  are unity vectors perpendicular to the propagation direction,  $p = 2\pi/\lambda$  is the propagation number,  $E_{x0}$  and  $E_{y0}$  are the amplitudes,  $\omega$  the angular frequency and  $\delta_x$  and  $\delta_y$  are the initial phases of the respective waves. The absolute values of  $\delta_x$  and  $\delta_y$  are irrelevant when describing light polarization. Instead the phase difference  $\Delta = \delta_x - \delta_y$  is usually used. The phase difference is one of the parameters that are determined by spectroscopic ellipsometry.

For  $p = 1$  and  $E_{x0} = E_{y0}$  three principal states of polarization can be discerned. The resulting projections of the electric field vector in the  $x,y$ -plane are shown in Figure 7:

- Linear polarization (Fig. 7 a,b) means that  $\Delta = 0$  or  $\pi$ . In these cases the resulting wave  $E(t)$  is described by a line.

- Circular polarization (Fig. 7 c,d) means that  $\Delta = \frac{\pi}{2}$  or  $\frac{3\pi}{2}$  which leads to right-circularly polarized light for  $\Delta = \frac{\pi}{2}$  and left-circularly polarized light for  $\Delta = \frac{3\pi}{2}$ .
- The most general case is elliptical polarization (Fig. 7 e,f) which covers all other possible  $\Delta$  values. A distinction between right-elliptically polarized light ( $0 < \Delta < \pi$ ) and left-elliptically polarized light ( $\pi < \Delta < 2\pi$ ) is possible in the same way as for circularly polarized light.

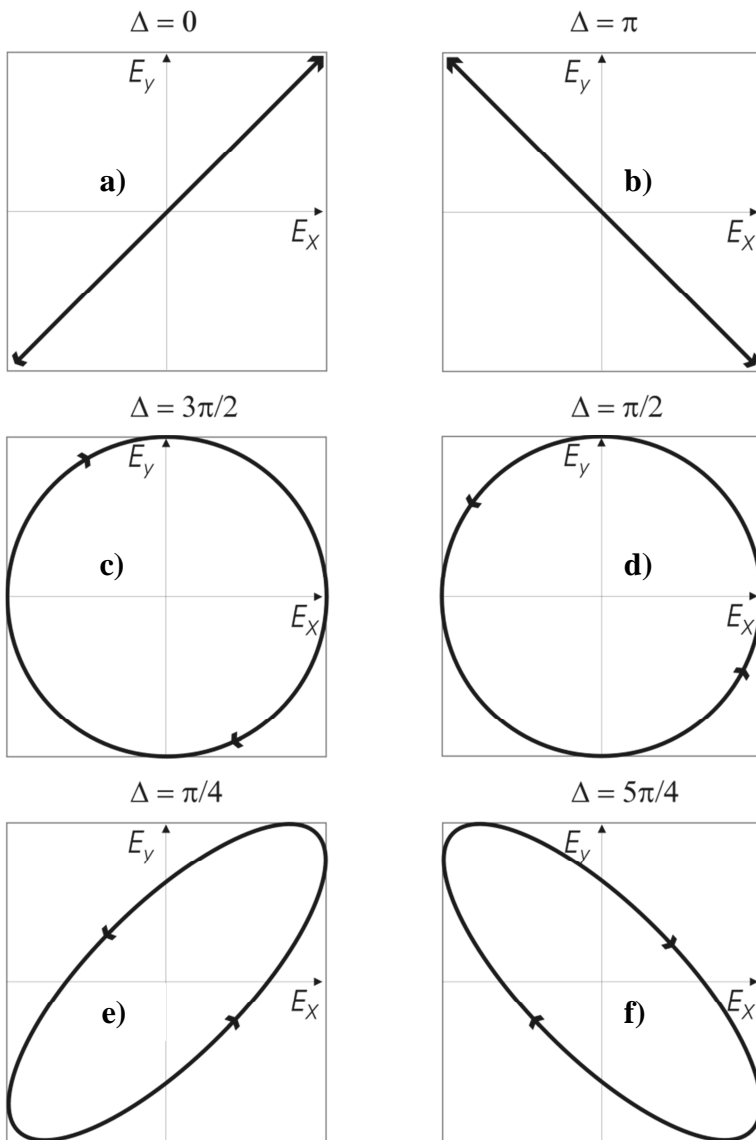


**Figure 7:** Polarization states of a light beam with a) and b) linear polarization, c) and d) right and left circular polarization and e) and f) left and right elliptic polarization.

Besides the phase shift, the state of polarization is determined by the amplitudes  $E_{x0}$  and  $E_{y0}$ . To be more precise, it is the relative amplitude  $E_{x0}/E_{y0}$  that is of analytical importance for ellipsometry and can be described by the angle  $\psi$  as:

$$\tan \psi = E_{x0}/E_{y0} \quad (2)$$

$\psi$  is the second parameter that is experimentally determined by ellipsometric spectroscopy.  $\Delta$  and  $\psi$  are called the ellipsometric angles. By fitting the experimental data of  $\Delta$  and  $\psi$  to a model the optical properties or thickness and morphology of a system can be analyzed as described in chapter 3.4.1.

## 2.4.2 Propagation of Polarized Light

To describe the propagation of polarized light through an ellipsometer a model is used that allows the description of the interaction between light and optical components such as a polarizer. Jones vectors and linear operations, represented by Jones matrices, are applied for pure elliptic polarizations. Another system consists of Stokes vectors and Mueller matrices, which are more suitable for practical purposes.

### Jones Vector

In reference to equation 1 the state of polarization can be written as a vector with two complex components.

$$\begin{bmatrix} E_x \\ E_y \end{bmatrix} = e^{i(\omega t - kz)} \begin{bmatrix} E_{x0} e^{i\delta_x} \\ E_{y0} e^{i\delta_y} \end{bmatrix} \quad (3)$$

The light intensity is given by

$$I = I_x + I_y \sim E_{x0}^2 + E_{y0}^2 \quad (4)$$

With

$$E_{x0}^2 + E_{y0}^2 = |E_x|^2 + |E_y|^2 \quad (5)$$

Only relative changes in amplitude and phase are used in conventional ellipsometric measurements. Absolute intensity values are not necessary since Jones Vectors are normalized ( $I = 1$ ). In this case, the linear polarization along the  $x$  and  $y$  direction can be expressed as:

$$\mathbf{E}_{\text{linear},x} = \begin{bmatrix} 1 \\ 0 \end{bmatrix} \quad \mathbf{E}_{\text{linear},y} = \begin{bmatrix} 0 \\ 1 \end{bmatrix} \quad (6)$$

Linearly polarized light at  $45^\circ$  angle with  $I = 1$  can be denoted as

$$\mathbf{E}_{45^\circ} = \frac{1}{\sqrt{2}} \begin{bmatrix} 1 \\ 1 \end{bmatrix} \quad (7)$$

Right circular polarization ( $\mathbf{E}_R$ ) and left circular polarization ( $\mathbf{E}_L$ ) are expressed by the following equations:

$$\mathbf{E}_R = \frac{1}{\sqrt{2}} \begin{bmatrix} 1 \\ i \end{bmatrix} \quad \mathbf{E}_L = \frac{1}{\sqrt{2}} \begin{bmatrix} 1 \\ -i \end{bmatrix} \quad (8)$$

One example of elliptic polarization described by the ellipsometric angles  $\Delta$  and  $\psi$  is:

$$\mathbf{E}_{\text{elliptic}} = \begin{bmatrix} \sin \psi_{xy} \exp(i\Delta_{xy}) \\ \cos \psi_{xy} \end{bmatrix} \quad (9)$$

When (9) is compared to (3) the number of real values needed to describe the polarization state is reduced from four to two. This is possible because, on the one hand Jones vectors have normalized intensities and on the other hand the absolute phase values are irrelevant and instead the phase shift is used.

## Jones Matrices

When light interacts with a polarizing optical element, the polarization state and light intensity change. Assuming only linear changes the transformation of a Jones vector (3) can be expressed in form of a matrix:

$$\begin{bmatrix} E'_\xi \\ E'_\eta \end{bmatrix} = \hat{f} \begin{bmatrix} E_x \\ E_y \end{bmatrix} = \begin{bmatrix} J_{11} & J_{12} \\ J_{21} & J_{22} \end{bmatrix} \begin{bmatrix} E_x \\ E_y \end{bmatrix} \quad (10)$$

The modified field amplitudes are, in general, related to another coordinate system  $\xi - \eta$  chosen in the plane of polarization. The 2 x 2 matrix  $\hat{f}$  of (10) is called Jones matrix of the element.

One example for such a transformation is the rotation of the coordinate system by an angle  $\alpha$  as illustrated by equation (11) and Figure 8:

$$\begin{bmatrix} E'_\xi \\ E'_\eta \end{bmatrix} = \hat{R}(\alpha) \begin{bmatrix} E_x \\ E_y \end{bmatrix} = \begin{bmatrix} \cos -\alpha & \sin -\alpha \\ -\sin -\alpha & \cos -\alpha \end{bmatrix} \begin{bmatrix} E_x \\ E_y \end{bmatrix} \quad (11)$$

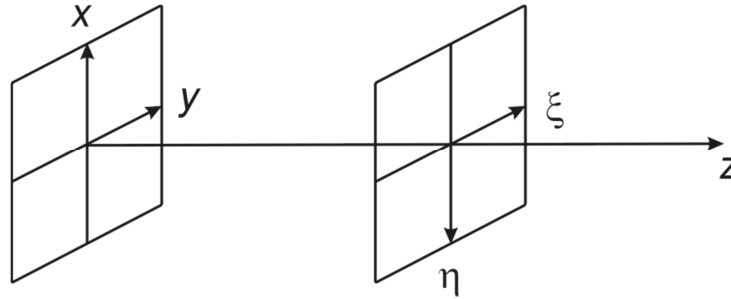


**Figure 8:** Clockwise rotation of the  $xyz$ -coordinate system around the  $z$ -axis by  $90^\circ$  leads to the  $\xi\eta z$ -coordinate system.

A slightly more complex example shows how a cascade of several operations transforms an input Jones Vector ( $\mathbf{E}_{in}$ ) into an output Jones Vector ( $\mathbf{E}_{out}$ ). This example consists of two linear polarizers (a and b) whose transmission axes are rotated by the angle  $\alpha$ . The second polarizer's (b)  $x$ -axis is rotated by the angle of  $\varphi$  in comparison to the light detector. The resulting transformation is given by the following equation:

$$\mathbf{E}_{out} = \hat{R}(\varphi)\hat{f}(b)\hat{R}(\alpha)\hat{f}(a)\mathbf{E}_{in} \quad (12)$$

## Stokes Vector

Jones vectors describe polarized light. But they cannot be used for the description of unpolarized or partially polarized light. For this purpose Stokes parameters are used. They consist of four real and experimentally accessible quantities, which have the dimension of intensity. A Stokes vector  $\mathbf{S}$  with the four Stokes Parameters  $S_0 - S_3$  is given below

$$\mathbf{S} = \begin{bmatrix} S_0 \\ S_1 \\ S_2 \\ S_3 \end{bmatrix} = \begin{bmatrix} I_0 \\ I_x - I_y \\ I_{\pi/4} - I_{-\pi/4} \\ I_R - I_L \end{bmatrix}, \quad (13)$$

with  $I_0$  being the total intensity of the beam.  $I_x, I_y, I_{\pi/4}$  and  $I_{-\pi/4}$  are the light intensities, which are transmitted through linear polarizers at the angles of  $0, \pi/2, \pi/4$  and  $-\pi/4$  respectively.  $I_R$  and  $I_L$  are the intensities passing through right- and left-circular polarizers. This also means that

$$I_0 = I_x + I_y = I_{\pi/4} + I_{-\pi/4} = I_R + I_L. \quad (14)$$

For unpolarized light there is no difference between the intensities denoting  $S_2 - S_3$ , thus the Stokes vector is described by the following equation:

$$\mathbf{S}_{unpolar} = S_0 \begin{bmatrix} 1 \\ 0 \\ 0 \\ 0 \end{bmatrix} \quad (15)$$

Linear polarization with the azimuth  $\varphi$  is written as

$$\mathbf{S}_{lin} = S_0 \begin{bmatrix} 1 \\ \cos 2\varphi \\ \sin 2\varphi \\ 0 \end{bmatrix}, \quad (16)$$

while the Stokes vectors of left- ( $\mathbf{S}_L$ ) and right-circular polarization ( $\mathbf{S}_R$ ) are

$$\mathbf{S}_L = S_0 \begin{bmatrix} 1 \\ 0 \\ 0 \\ -1 \end{bmatrix} \quad \mathbf{S}_R = S_0 \begin{bmatrix} 1 \\ 0 \\ 0 \\ 1 \end{bmatrix}. \quad (17)$$

Using the ellipsometric angles  $\Delta$  and  $\psi$  for elliptic polarization leads to the following Stokes vector:

$$\mathbf{S}_{ell} = S_0 \begin{bmatrix} 1 \\ -\cos 2\psi \\ \sin 2\psi \cos \Delta \\ -\sin 2\psi \sin \Delta \end{bmatrix} \quad (18)$$

### Mueller Matrix

The Mueller matrix is a 4 x 4 matrix with a function analogous to the Jones Matrix. It allows the description of the interaction of a light beam (represented by a Stokes vector) with optical elements.

$$\mathbf{S}' = \begin{bmatrix} S'_0 \\ S'_1 \\ S'_2 \\ S'_3 \end{bmatrix} = \hat{M} \begin{bmatrix} S_0 \\ S_1 \\ S_2 \\ S_3 \end{bmatrix} = \begin{bmatrix} M_{11} & M_{12} & M_{13} & M_{14} \\ M_{21} & M_{22} & M_{23} & M_{24} \\ M_{31} & M_{32} & M_{33} & M_{34} \\ M_{41} & M_{42} & M_{43} & M_{44} \end{bmatrix} \begin{bmatrix} S_0 \\ S_1 \\ S_2 \\ S_3 \end{bmatrix} \quad (19)$$

To rotate the coordinate system by the angle  $\alpha$  the following Mueller matrix is used in the same way as the rotation matrix (11)

$$\hat{M}(\alpha) = \begin{bmatrix} 1 & 0 & 0 & 0 \\ 0 & \cos 2\alpha & \sin 2\alpha & 0 \\ 0 & -\sin 2\alpha & \cos 2\alpha & 0 \\ 0 & 0 & 0 & 1 \end{bmatrix} \quad (20)$$

The similarity to the Jones formalism also includes the cascade of  $n$  consecutive transformations leading from an input Stokes vector ( $\mathbf{S}_{in}$ ) to an output Stokes vector ( $\mathbf{S}_{out}$ )

$$\mathbf{S}_{out} = \hat{M}_n \dots \hat{M}_2 \hat{M}_1 \mathbf{S}_{in} \quad (21)$$

### 2.4.3 Optical Elements

The following section introduces the optical elements used in the ellipsometry and PM-IRRAS experiments conducted in this thesis. All optical elements are assumed to behave ideally, meaning that there is no significant attenuation of the light wave due to an interaction with the optical element. Their use in the optical setup is described in detail below. The rotation of the coordinate system (Tab. 3) usually accompanies the theoretical treatment of optical elements to facilitate the description of the light beam after interaction, e.g. reflection.

#### Polarizer (Analyzer)

Polarizers generate linearly polarized light from any input polarization. Several kinds of polarizers can be distinguished. A Mueller matrix describing this transformation is listed in Table 3. Different physical properties can be applied for this effect, e.g. the birefringence of calcite ( $\text{CaCO}_3$ ) is employed in Glan-Taylor prisms, or the dichroism in wire-grid polarizers.

**Table 3:** Optical elements and examples for the corresponding Jones matrices and Mueller matrices.

<i>Optical Element</i>	<i>Jones Matrix</i>	<i>Mueller Matrix</i>
Linear polarizer (Analyzer)	$\begin{bmatrix} 1 & 0 \\ 0 & 0 \end{bmatrix}$	$\frac{1}{2} \begin{bmatrix} 1 & 1 & 0 & 0 \\ 1 & 1 & 0 & 0 \\ 0 & 0 & 0 & 0 \\ 0 & 0 & 0 & 0 \end{bmatrix}$
Compensator (Retarder)	$\begin{bmatrix} 1 & 0 \\ 0 & \exp(-i\delta_c) \end{bmatrix}$	$\begin{bmatrix} 1 & 0 & 0 & 0 \\ 0 & 1 & 0 & 0 \\ 0 & 0 & \cos \delta_c & \sin \delta_c \\ 0 & 0 & -\sin \delta_c & \cos \delta_c \end{bmatrix}$
Photoelastic modulator	$\begin{bmatrix} 1 & 0 \\ 0 & \exp(i\delta) \end{bmatrix}$	$\begin{bmatrix} 1 & 0 & 0 & 0 \\ 0 & 1 & 0 & 0 \\ 0 & 0 & \cos \delta & -\sin \delta \\ 0 & 0 & \sin \delta & \cos \delta \end{bmatrix}$

Coordinate rotation	$\begin{bmatrix} \cos \alpha & \sin \alpha \\ -\sin \alpha & \cos \alpha \end{bmatrix}$	$\begin{bmatrix} 1 & 0 & 0 & 0 \\ 0 & \cos 2\alpha & \sin 2\alpha & 0 \\ 0 & -\sin 2\alpha & \cos 2\alpha & 0 \\ 0 & 0 & 0 & 1 \end{bmatrix}$
Isotropic reflecting surface	$\begin{bmatrix} -r_x \exp(i\delta_x) & 0 \\ 0 & r_y \exp(i\delta_y) \end{bmatrix}$	$\frac{r_x^2}{2 \cos^2 \psi} \begin{bmatrix} 1 & N & 0 & 0 \\ N & 1 & 0 & 0 \\ 0 & 0 & C & S \\ 0 & 0 & S & C \end{bmatrix}$
	$r_x, r_y$ are the reflectivities in the coordinate directions	$N = -\cos 2\psi$ $C = \sin 2\psi \cos \Delta$ $S = \sin 2\psi \sin \Delta$

Analyzers are technically identical to polarizers. Polarizers are positioned between the light source and the sample, analyzer are located between sample and detector. For ellipsometry the analyzer is rotated by  $45^\circ$  and  $-45^\circ$  from the beam y-axis. From the differences in the beam intensities the Stokes parameters and ellipsometric angles can be calculated.

### Compensator (Retarder)

A compensator also called retarder, transforms light of linear polarization into elliptically or circularly polarized light. A birefringent crystal leads to a phase shift  $\delta_C$  between the components of linearly polarized light in the direction of the fast and slow axis. This phase difference is expressed by the following equation:

$$\delta_C = \frac{2\pi}{\lambda} |n_C - n_0| d \quad (22)$$

where  $d$  denotes the thickness of the compensator,  $|n_C - n_0|$  is the difference between the refractive indices of the experimental environment ( $n_0$ ) and the crystal ( $n_C$ ). The corresponding Jones and Mueller matrices are provided in Table 3.

## Photoelastic Modulator

Application of a stress to an optically isotropic material causes a deformation, which leads to a change of electron density in the direction of the stress. In consequence the material becomes optically anisotropic. This behaviour is called photoelasticity. The resulting birefringence is proportional to the applied stress and one optical axis coincides with the direction of the stress. The difference to the functionality of a compensator is that the birefringence does not need to be constant in time.

A typical photoelastic modulator (PEM) setup is shown in Figure 9. A block of crystalline quartz is used as piezoelectric transducer for the mechanical stress. When an electric field is applied at resonance frequency the resulting vibration is directed along the long axis of the crystal. A fused quartz with the same resonance frequency is connected to the crystal quartz on one side and interacts with the transmitted light. The resonance of the transducer leads to a periodic stress in the fused quartz and thus a change of the retardation of transmitted light along the slow and fast axes of the crystal.

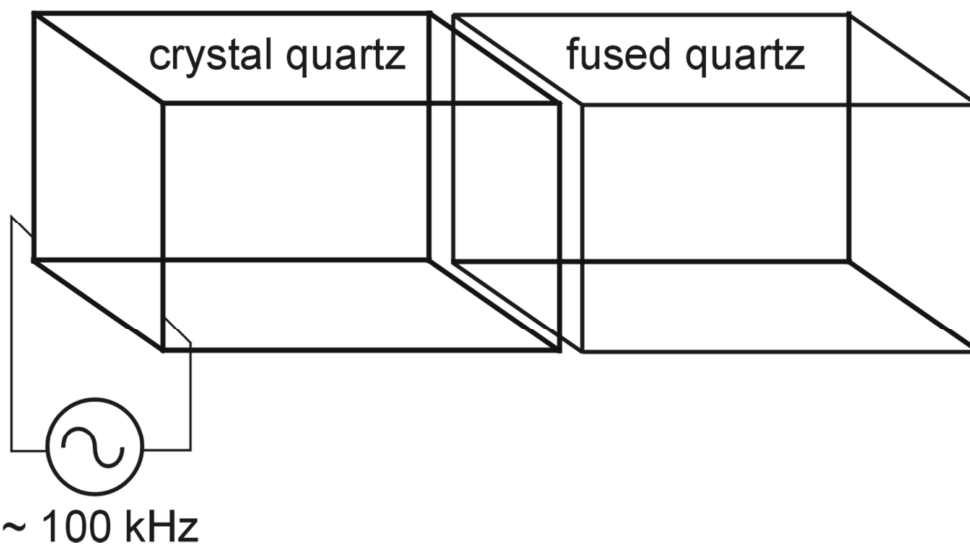


**Figure 9:** Components of a photoelastic modulator. (adapted from <sup>[68]</sup>)

The time dependent phase difference  $\delta_{PEM}$  between the fast and slow axis of the fused quartz are described by:

$$\delta_{PEM} = F \sin(\omega t) \quad (23)$$

Where  $F$  represents the phase amplitude and  $\omega = 2\pi\nu$  with  $\nu$  the resonance frequency. The Jones and Mueller matrices representing a PEM are given in Table 3.

For the PM-IRRAS technique the PEM is used as a half wave retarder. This means that at the extreme points of compression, the light wave passing through the fused quartz is retarded by half its wavelength along the slow axis of the PEM (Fig. 10). For an input light wave, that is polarized linearly at  $45^\circ$  it is hence possible to switch between two orthogonal states of polarization (p- and s-polarization). If for example the half wave retardation is set at  $1600\text{ cm}^{-1}$  ( $\lambda = 6250\text{ nm}$ ), then  $\delta_{PEM}$  is equal to  $3125\text{ nm}$ .

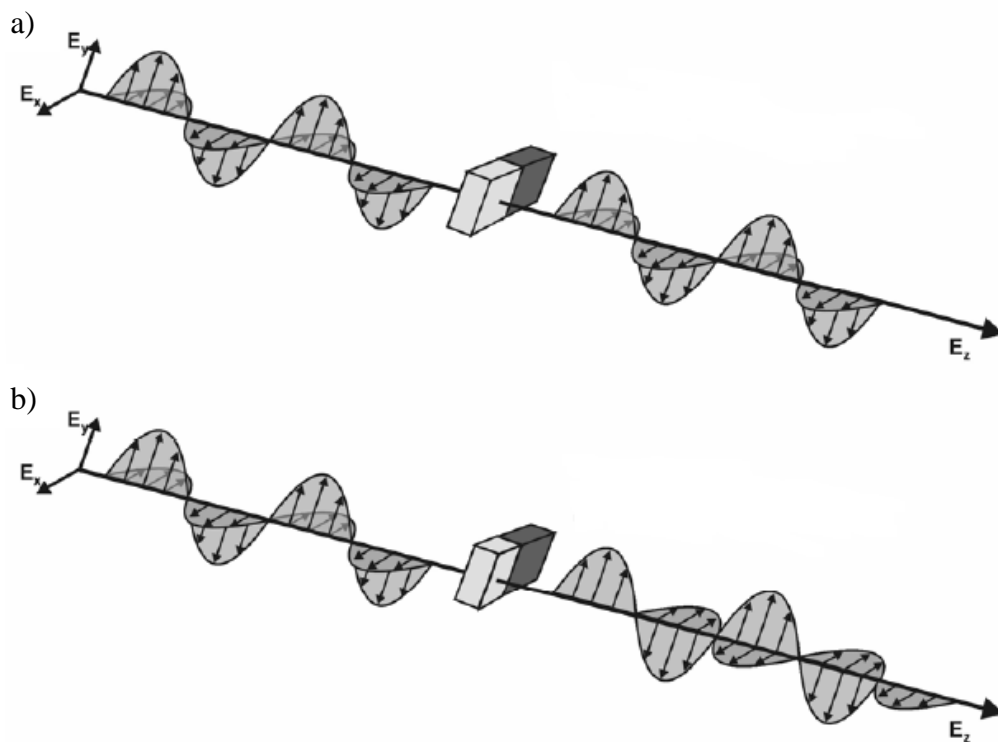


**Figure 10:** Half wave retardation in a PEM, for a relaxed crystal a) there is no change in the state of polarization. For a compressed crystal b) the component of the light wave along the slow axis is retarded by half its wave length. (Adapted from <sup>[70]</sup>)

### Isotropic Reflecting Surface

The reflection of a light wave on a planar surface changes the state of polarization of an incoming light beam. For an oblique angle of incidence (i.e. other than  $90^\circ$ ) the coordinate systems in the plane of polarization of the incident and reflected wave change. Even for normal incidence the  $x$  or  $y$  axis must be of

opposite sign after reflection to keep the right-handed  $x$ - $y$ - $z$  system preserved. The Mueller and Jones matrices that describe this transformation, using the ellipsometric angles  $\psi$  and  $\Delta$ , are given in Table 3.

## 2.4.4 Ellipsometric Measurements

In ellipsometry the change of a light wave's state of polarization after reflection from the sample is the observable (Fig. 11). The measurement of the change of light polarization distinguishes this technique from other optical methods (e.g. IR spectroscopy), in which the change of light intensity is measured. The state of polarization is determined by measuring orthogonal components of the light wave. Preferably the p- and s-components, where p- means the electric field oscillates parallel (German: **p**arallel) to the plane of incidence and the s-component oscillates perpendicular (German: **s**enkrecht) to the plane of incidence. The p- and s-polarized light is reflected differently at a surface. This means that after reflection a linearly polarized light wave is, usually, transformed into an elliptically polarized one, hence the name ellipsometry. This change can be expressed via the ellipsometric angles  $\psi$  and  $\Delta$ .  $\Delta$  correlates to the attenuation coefficient  $k$  and  $\psi$  is related to the amplitude ratio of p- and s-polarized light (see Eq. 2). The refractive index  $n$  can be derived from this angle [ 68, 69].

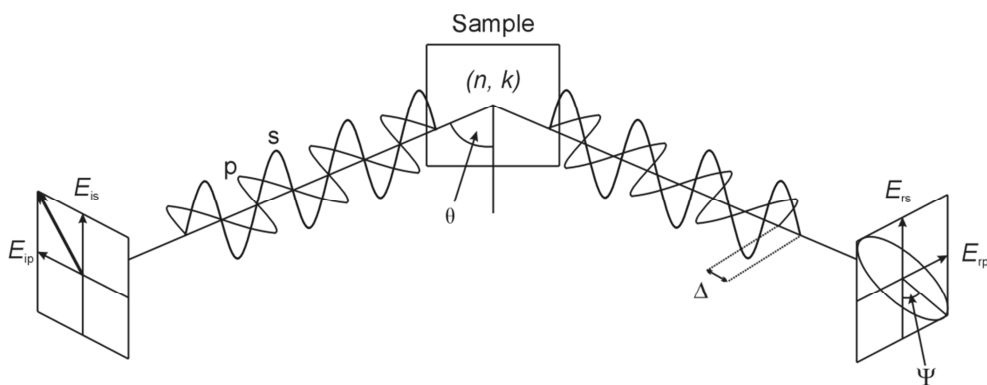


**Figure 11:** Schematic representation of the principle of ellipsometry. Different reflection of p- and s-components of incident linearly polarized light leads to elliptic polarization of the reflected light with ellipsometric angles  $\psi$  and  $\Delta$ .

The reflectivity from a surface is also dependent on the angle of incidence ( $\theta$ ). The angle, at which the largest difference between the reflectivity of p- and s-

polarized light is reached, is called the Brewster angle. Ellipsometric measurements are usually performed at this angle.

The direct results from an ellipsometric measurement are the ellipsometric angles  $\psi$  and  $\Delta$ . However, the desired results are usually the refractive index  $n$  and attenuation coefficient  $k$ . If both are known, the film thickness and porosity can be determined. In order to extract any of those values, the experimental data have to be fitted to an optical model.

## 2.5 Infrared Reflection Absorption Spectroscopy

Infrared spectroscopy (IRS) is a broadly used technique, which can be regarded as one of the most important non-destructive analytical tools used in science <sup>[71]</sup>. The largest field of application is the qualitative analysis of organic substances. IR spectra are rich in information about the presence of structural elements and functional groups. Furthermore, single substances can be identified via their fingerprint-like IR spectrum. Information concerning the structure of complex macromolecules like proteins can be gained <sup>[72]</sup>. Several reflection methods have been developed in the late 20<sup>th</sup> century, because of their high sensitivity and their application for interface analysis <sup>[20]</sup>.

In the 1960s Greenler published calculations and first measurements that were the foundation for the development of the infrared reflection absorption spectroscopy (IRRAS) <sup>[73, 74]</sup>. He demonstrated that upon reflection of p-polarized light from a gold surface, a constructive interference with the incident beam occurs (Fig. 12a), resulting in an increased intensity of the electric field perpendicular to the surface. s-polarized light, on the other hand, is about 180° phase-shifted upon reflection and destructive interference cancels the electric field at the surface (Fig. 12b). This phenomenon is often referred to as the surface selection rule, meaning that only p-polarized light can interact with a sample at the surface <sup>[75]</sup>. In addition, this also means that only molecules with a transitional dipole moment that has a component normal to the surface can be detected by IRRAS methods.

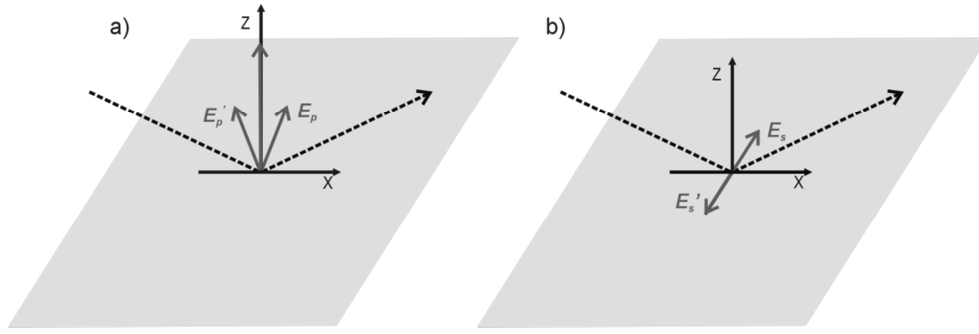


**Figure 12:** Electric field vectors at the surface. a) enhanced electric field vector of p-polarized light due to constructive interference directly at the surface. b) the electric field vectors of incident and reflected s-polarized light interfere destructively at the surface.

The IRRAS aims at the analysis of thin films deposited on reflecting surfaces. A p-polarized beam is reflected at the substrate surface and subsequently detected (Fig. 13). To obtain any quantitative information the angle of incidence  $\theta_i$  and the complex refractive index  $N_m$  of the different phases  $x$  have to be known.

$$N_m = n_m + ik_m \quad (24)$$

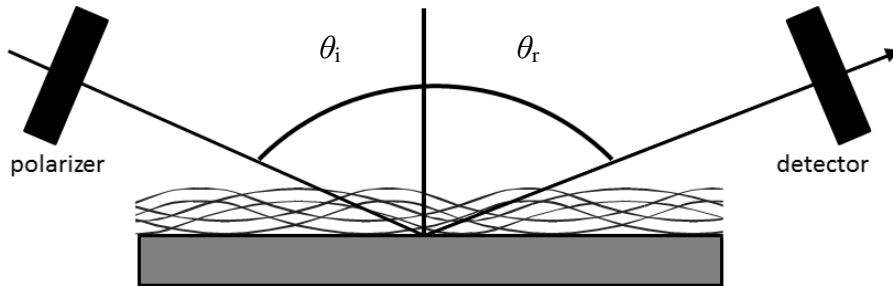


**Figure 13:** Scheme of the IRRAS setup on the air solid interface.

A mathematical description of the reflectivity and transmittance of an IR beam reflected from an interface (Fig. 14) are given by the Fresnel equations <sup>[76]</sup>. For the interface between the phases 1 and 2 and p-polarized light the resulting reflection and transmission coefficients are:

$$r_{\parallel 12} = \frac{\varepsilon_2 \xi_1 - \varepsilon_1 \xi_2}{\varepsilon_2 \xi_1 + \varepsilon_1 \xi_2} \quad (25)$$

$$t_{\parallel 12} = 2 \frac{\varepsilon_2 \xi_1}{\varepsilon_2 \xi_1 + \varepsilon_1 \xi_2} \quad (26)$$

With the complex dielectric constant  $\epsilon_m$  for the phase  $m$  and the refraction coefficient  $\xi_m = N_m \cos \theta_m$ . The reflection and transmission coefficient of s-polarized light are:

$$r_{\perp 12} = \frac{\mu_2 \xi_1 - \mu_1 \xi_2}{\mu_2 \xi_1 + \mu_1 \xi_2} \quad (27)$$

$$t_{\perp 12} = 2 \frac{\mu_2 \xi_1}{\mu_2 \xi_1 + \mu_1 \xi_2} \quad (28)$$

with the magnetic permeability  $\mu_m$ . For the systems discussed in this thesis  $\mu$  equals one and has no influence on the equations.

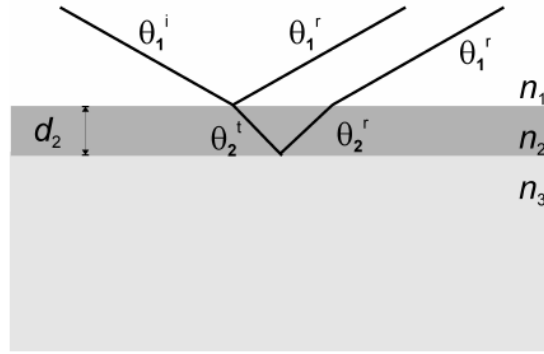


**Figure 14:** Reflected and transmitted beam in a three phase model.

If the system is expanded from a single interface to a three phase system with the thickness  $d_2$  of the second layer and the attenuation coefficient  $\beta$  of the light within this phase

$$\beta = 2\pi \frac{d_2}{\lambda} \xi_2 \quad (29)$$

yields the reflection and transmission coefficients for p- and s-polarized light <sup>[76]</sup>:

$$r_{\parallel} = \frac{r_{\parallel 12} + r_{\parallel 23} e^{-2i\beta}}{1 + r_{\parallel 12} r_{\parallel 23} e^{-2i\beta}} \quad (30)$$

$$t_{\parallel} = \frac{t_{\parallel 12} + t_{\parallel 23} e^{-2i\beta}}{1 + r_{\parallel 12} r_{\parallel 23} e^{-2i\beta}} \quad (31)$$

$$r_{\perp} = \frac{r_{\perp 12} + r_{\perp 23} e^{-2i\beta}}{1 + r_{\perp 12} r_{\perp 23} e^{-2i\beta}} \quad (32)$$

$$t_{\perp} = \frac{t_{\perp 12} + t_{\perp 23} e^{-2i\beta}}{1 + r_{\perp 12} r_{\perp 23} e^{-2i\beta}} \quad (33)$$

From the Fresnel equations it is possible to calculate the transmittance  $T$  and reflectivity  $R$  of p- and of s-polarized light respectively. Only the reflectivity is relevant for IRRAS measurements.

$$R = |r|^2 \quad (34)$$

The Fresnel equations also allow the calculation of the mean electric fields of the different polarization at the surface in comparison to the incident electric field  $\langle (E_1^o)^2 \rangle^{1/2}$ :

$$\frac{\langle (E_{\perp 1})^2 \rangle}{\langle (E_{\perp 1}^o)^2 \rangle} = (1 + R_{\perp}) + 2R_{\perp}^{1/2} \cos \left[ \delta_{\perp}^r - 4\pi \left( \frac{z}{\lambda} \right) \xi_1 \right] \quad (35)$$

$$\frac{\langle (E_{\parallel 1x})^2 \rangle}{\langle (E_{\parallel 1x}^o)^2 \rangle} = \cos^2 \theta_1 \left\{ (1 + R_{\parallel}) - 2R_{\parallel}^{1/2} \cos \left[ \delta_{\parallel}^r - 4\pi \left( \frac{z}{\lambda} \right) \xi_1 \right] \right\} \quad (36)$$

$$\frac{\langle (E_{\parallel 1z})^2 \rangle}{\langle (E_{\parallel 1z}^o)^2 \rangle} = \sin^2 \theta_1 \left\{ (1 + R_{\parallel}) + 2R_{\parallel}^{1/2} \cos \left[ \delta_{\parallel}^r - 4\pi \left( \frac{z}{\lambda} \right) \xi_1 \right] \right\} \quad (37)$$

with  $\delta^r$  being the phase shift of the electric field after reflection. The shift is defined by the real and imaginary parts of the Fresnel coefficients:

$$\delta_{ab}^r = \arg(r_{ab}) = \tan^{-1} \left[ \frac{\text{Im}(r_{ab})}{\text{Re}(r_{ab})} \right] \quad (38)$$

The enhancement of the electric field close to the surface for p-polarized light, together with a longer beam path through the sample, increases the sensitivity of this technique significantly in comparison to transmission techniques. This allows the analysis of organic samples of a thickness of a single-molecule layer <sup>[77, 78]</sup>. However, separate background spectra have to be recorded for each sample introducing a systematic error to the IRRAS measurement.

## 2.5.1 Polarization Modulation Infrared Reflection Absorption Spectroscopy

In the early 1980's Golden and co-workers developed the polarization modulation infrared reflection absorption technique (PM-IRRAS) [79]. They used the fact that s-polarized light does not interact with the sample at the surface. While p-polarized light contains information about the background and the sample, s-polarized light only contains background information. By fast modulation between s- and p-polarized light it is possible to quasi simultaneously measure background and sample spectra. This allows for a much faster and exacter measurement of films with a thickness in the monolayer range compared to conventional IRRAS techniques [80, 81]. For the instrumental realization a photoelastic modulator is inserted into the beam path behind the polarizer and a lock-in amplifier is used as a filter to demodulate the beam (Fig. 15).

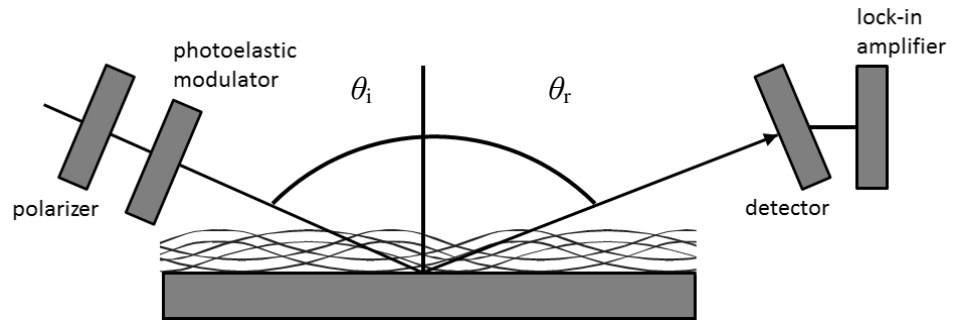


**Figure 15:** Scheme of the PM-IRRAS setup.

At the detector p- and s-polarized light are not measured separately. Instead the ratio of the difference  $|R_s - R_p|$  of the reflected s- and p-polarized light and the average  $(R_s + R_p)/2$  of both signals are measured [80, 81, 82]. In theory this can be described in terms of intensity [81]:

$$\left(\frac{\Delta I}{\langle I \rangle}\right)_{theor.} = 2 \frac{I_s - I_p}{I_s + I_p} \quad (39)$$

With  $\Delta I$  as the difference in intensity and  $\langle I \rangle$  the average intensity. In practice the detected signal has to be demodulated to gain two intensities  $\Delta I(\omega)$  and  $\langle I \rangle(\omega)$  as a function of the excitation frequency  $\omega$  of the photoelastic

modulator. These are linked to the first ( $J_1(\phi_0)$ ) and second ( $J_2(\phi_0)$ ) order Bessel functions with  $\phi_0$  being the maximum shift of the incident light by the PEM <sup>[82]</sup>.

$$\langle I \rangle(\omega) = \frac{I_s(\omega) + I_p(\omega)}{2} + \frac{|I_s(\omega) - I_p(\omega)|}{2} J_1(\phi_0) \quad (40)$$

$$\Delta I(\omega) = |I_s(\omega) - I_p(\omega)| J_2(\phi_0) \quad (41)$$

The equations 40 and 41 can be reduced to <sup>[82]</sup>

$$\langle I \rangle(\omega) = \langle I \rangle + \frac{\Delta I}{2} J_1(\phi_0) \quad (42)$$

$$\Delta I(\omega) = \Delta I J_2(\phi_0) \quad (43)$$

On highly reflective surfaces  $\Delta I$  is much smaller than  $\langle I \rangle$ . Thus, the second term in (42) is negligible compared to  $\langle I \rangle$  and (42) can be simplified to.

$$\langle I \rangle + \frac{\Delta I}{2} J_1(\phi_0) \approx \langle I \rangle \quad (44)$$

The intensity average and intensity difference spectra are plotted in (Fig. 16 a). The resulting experimental spectrum is the ratio of  $\Delta I(\omega)$  and  $\langle I \rangle(\omega)$

$$\left( \frac{\Delta I(\omega)}{\langle I \rangle(\omega)} \right)_{exp.} = \frac{\Delta I}{\langle I \rangle} J_2(\phi_0) \quad (45)$$

In other words: the experimental spectra are the product of the theoretical spectrum with the second order Bessel function (Fig. 16 b). The Bessel function describes how well the PEM is able to switch between the two states of polarization. The retardation of a light beam depends on the wavelength <sup>[81]</sup>. Correspondingly, the main maximum of the Bessel function is found at the wavelength for which the switching between s- and p-polarization was done. The intensity declines to higher wavenumbers indicating, that the difference between the polarizations becomes smaller until it drops to zero. At this point there is no difference between the two polarizations and hence no change in polarization.

Accordingly, only the region around the main maximum can be used (Fig. 16 b). The half wave retardation of the PEM, that is the point at which p- and s-polarization works ideally, has to be set to the wavelength of interest before the spectrum is recorded.

To extract the absorption spectrum, the raw data have to be corrected for the Bessel function (Fig. 16 c). The Bessel function can be calculated <sup>[ 83]</sup>. However, for this thesis a polynomial was determined to fit the Bessel function manually.

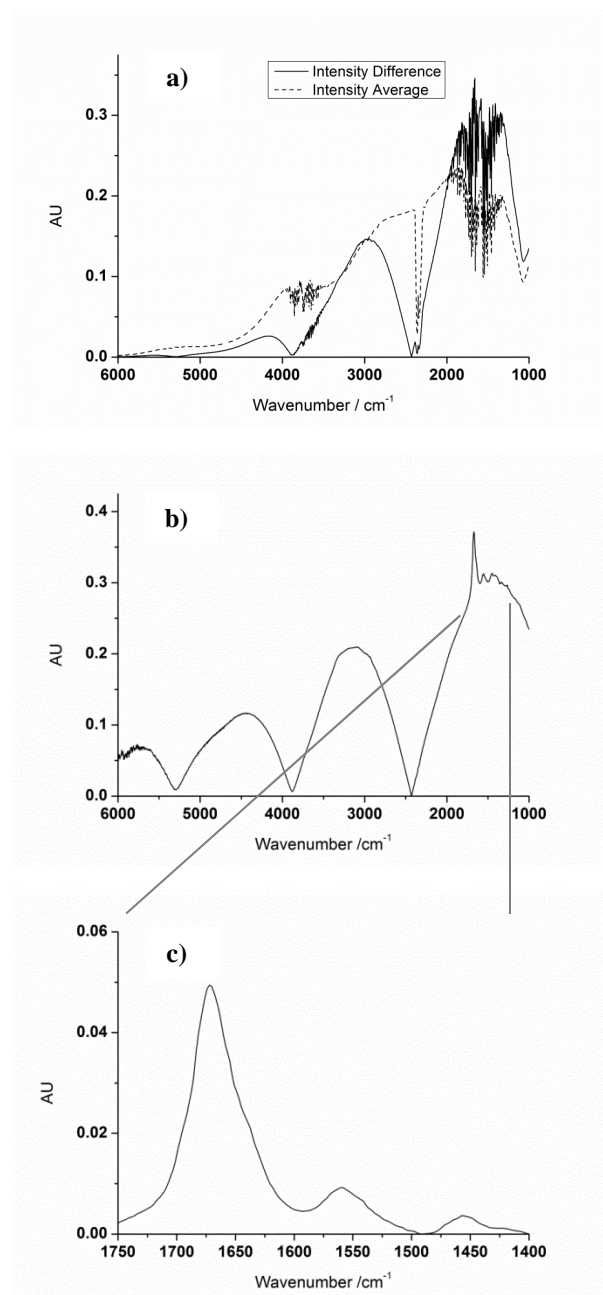


**Figure 16:** Steps in PM-IRRA spectrum development. a) Intensity average and intensity difference spectrum. b) Intensity ratio including Bessel function. c) Final spectrum of the amide I region (1750 cm<sup>-1</sup> – 1400 cm<sup>-1</sup>) after correction for the Bessel function.

## 2.5.2 IR Spectroscopy of Proteins

All proteins have one common feature: they are built of amino acids connected via amide bonds. Accordingly, the amide bands, of which nine are distinguished in literature (Tab. 4), are the most prominent contributions to a protein infrared spectrum. Another spectral feature of proteins, shared with all carbohydrates, are the CH<sub>2</sub>/CH<sub>3</sub>-vibrational modes (Tab. 5). However, most of those modes do not yield any structural information concerning proteins.

The protein structure is a complex system. The primary structure describes the amino acid sequence of the protein backbone. The secondary structures are locally formed by hydrogen bonding. Examples for such structural elements are  $\alpha$ -helix,  $\beta$ -sheet, random coil and  $\beta$ -turn<sup>[84, 85]</sup>. The overall structure of a protein is called the tertiary structure. Finally, the quaternary structure describes the interaction between protein molecules, like the formation of fibrils. The three dimensional structure of proteins under physiological conditions is referred to as the native structure. If the ambient conditions change (e.g. temperature, pH, pressure, solvent composition)<sup>[16, 17, 86, 87, 88, 89, 90, 91, 92]</sup>, a protein may unfold (i.e. it loses features of its secondary to quaternary structure) leading to a denaturated protein.

**Table 4:** Amide vibrational modes of proteins<sup>[93, 94]</sup>.

<i>Vibrational Mode Designation</i>	<i>Wavenumber / cm<sup>-1</sup></i>	<i>Nature of Vibrations</i>
A	3300	N-H stretching, in
B	3100	resonance with Amide II overtone
I	1653	80% C=O stretching, 10% C-N stretching, 10% N-H bending
II	1567	60% N-H bending, 40% C-N stretching

<i>Vibrational Mode Designation</i>	<i>Wavenumber / cm<sup>-1</sup></i>	<i>Nature of Vibrations</i>
III	1299	30% C-N stretching, 30% N-H bending, 10% C=O stretching, 10% O=C-N bending, 20% other
IV	627	40% O=C-N bending, 60% other
V	725	N-H bending
VI	600	C=O bending
VII	200	C-N torsion

**Table 5:** Acyl chain modes <sup>[95]</sup>.

<i>Vibrational Mode</i>	<i>Wavenumber / cm<sup>-1</sup></i>
$\nu_{as}(\text{CH}_3)$ asymmetric stretch	2950-2980
$\nu_{as}(\text{CH}_2)$ asymmetric stretch	2915-2924
$\nu_s(\text{CH}_3)$ symmetric stretch	2860-2885
$\nu_s(\text{CH}_2)$ symmetric stretch	2848-2854
$\delta(\text{CH}_2)$ scissoring	1462-1474 1468 1473
$\delta_{as}(\text{CH}_3)$ bending	1450
<i>roc.</i> (CH <sub>2</sub> ) rocking	720, 728

The amide I band is especially suitable to analyse the secondary structure of a protein <sup>[96, 97, 98, 99, 100]</sup>. This usually broad absorption band is composed of several overlapping bands. Deconvolution yields signals that can be assigned to different structural elements (Tab. 6). However, these assignments are based on empirical data obtained from polypeptides or proteins with only one dominant structural element and can be used only with caution. For instance, the amide I bands of myoglobin and haemoglobin, both purely  $\alpha$ -helical proteins, have a

component in the 1640  $\text{cm}^{-1}$  - 1620  $\text{cm}^{-1}$  region, which would indicate a  $\beta$ -structure<sup>[96, 101]</sup>.

**Table 6:** Amide I frequencies of secondary protein structure<sup>[84, 85]</sup>.

<i>Wavenumber / <math>\text{cm}^{-1}</math></i>	<i>Assignment</i>
1621-1627	$\beta$ -Structure
1628-1634	
1635-1640	
1641-1647	random Coil
1651-1657	$\alpha$ -Helix
1658-1666	turns and bends
1668-1671	
1671-1679	$\beta$ -Structure
1681-1685	turns and bends
1687-1690	
1692-1696	

## IR Spectroscopy of Collagen

Due to its unique composition and structure, the amide I band of the IR spectrum of collagen differs significantly from IR spectra of other proteins. There have been several attempts to explain the amide I band components by assigning them to different systems of H-bonds in the literature<sup>[15, 102, 103]</sup>. The amide I band analysis carried out in this thesis will refer to the band assignments developed by Lazarev et al.<sup>[102]</sup> and Payne et al.<sup>[15]</sup> (Tab. 7), because of their good correlation to the widely accepted structural model of collagen developed by Ramachandran<sup>[43]</sup>. They identified three to four major amide I band components and correlated them to inter helical H-bonds and H-bonds to water molecules. The strongest component around 1660  $\text{cm}^{-1}$  is related to  $\nu(\text{CO})$  in the X-position involved in interhelical H-bonds with the Gly amine group (2.3.1) and vanishes during denaturation<sup>[15]</sup>. The second component of the amide I band is located around 1630-1633  $\text{cm}^{-1}$  and appears due to the contribution of imino acid (Pro and Hyp)

carbonyls H-bonded to water. This was verified by the dependence between band intensity and imino acid fraction in the collagen molecules [102]. The two remaining minor bands are not defined consensually in literature [15, 102]. While Lazarev et al. [102] correlated the band at 1670  $\text{cm}^{-1}$  to carbonyl groups of the remaining amino acids H-bonded to water, Payne et al. [15] on the other hand observed a small band in that region but did not attribute it to any structural element. The same authors attributed a component at 1643  $\text{cm}^{-1}$  to Gly carbonyls that have formed H-bonds to water. That band was not observed at all by Lazarev et al. [102]

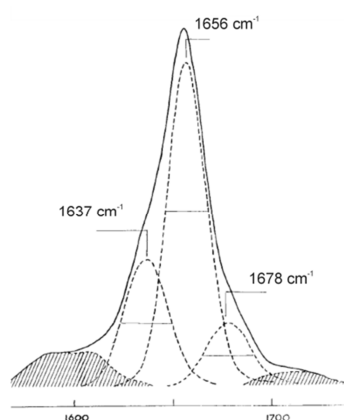


**Figure 17:** Amide I band and deconvolution by Lazarev et al. (adapted from [102])

**Table 7:** Amide I frequencies of collagen [15, 102].

<i>Wavenumber / <math>\text{cm}^{-1}</math></i>	<i>Assignment</i>
1630-1633	H-Bonds between HYP and Water
1643	H-Bonds between GLY and water
1656-1660	inter helical H-bonds
1670	H-Bonds of other amino acids to water



## 3 Experimental Section

### 3.1 Preparation of Collagen Films

Three kinds of substrates were used to investigate collagen molecules adsorbed on gold surfaces: two polycrystalline gold disc electrodes with diameters of 15 mm and 4 mm and 100 nm gold films vapour deposited on a glass slide with a 1-3 nm chromium adhesive layer on glass. Prior to every measurement, the disc electrodes were rinsed with deionized water (Elga Purelab Classic UV) and ethanol (VWR International, Germany) and annealed in a flame (to oxidize organic residues on the surface). The hot discs were cooled gradually under a flow of argon (Air Liquide Deutschland GmbH, Germany). The evaporated gold film was rinsed with deionized water and ethanol and afterwards put into an UV.TC.EU.003 UV TipCleaner (Bioforce Nanosciences, Inc., Ames, IA, USA) for 30 minutes.

Collagen adsorption was carried out in a protein solution (Collagen I, rat tail in 0.02 M acetic acid, BD Biosciences, Germany) diluted in PBS (pH 7.4) to a concentration of  $0.1 \text{ mg ml}^{-1}$  and at constant temperature  $T = 4 \text{ }^{\circ}\text{C}$ . It has the physiological pH-value (7.4) and an ion concentration and composition similar to body fluids. It is prepared by dissolution of 8 g NaCl (Sigma Aldrich Chemie GmbH, Germany), 0.2 g KCl (Karl Roth GmbH & Co, Germany), 1.44 g  $\text{Na}_2\text{HPO}_4$  (Scharlau Chemie S. A., Germany) and 0.24 g  $\text{KH}_2\text{PO}_4$  (Sigma Aldrich Chemie GmbH, Germany) filling up to 1 l in deionized water. Alternatively, a commercially available PBS mixture (P-5368, Sigma Aldrich Chemie GmbH, Germany) was used, that already contained all salts in the necessary amounts.

The cleaned substrates were immersed into the solution for 10 min and afterwards rinsed with water and dried under argon flow. The experimental parameters for the protein concentration and time dependent measurements of collagen adsorption are listed in Table 8.

**Table 8:** Experimental parameters for concentration-dependent and time-dependent collagen adsorption.

<i>Concentration dependence</i>	<i>Concentration</i> <i>/ <math>\mu\text{g ml}^{-1}</math></i>	<i>Time dependence</i>	<i>Adsorption time</i> <i>/ min</i>
Adsorption time = 10 min	1	Concentration = 100 $\mu\text{g/ml}$	2
	10		5
	100		10
			20

### **3.2 Langmuir-Blodgett and Langmuir-Schaefer Transfer of a DMPC bilayer**

For the transfer of ordered lipid bilayers a commercially available Langmuir trough (KSV Instruments LTD, Helsinki, Finland) was used as schematically illustrated in Figure 18. It consists of a rectangular Teflon trough with movable barriers on two sides. The surface pressure was measured with a Wilhelmy plate, which is connected to an electronic balance. In order to transfer a monolayer the substrate was attached to a dipper with an electro motor. Depending on the hydrophobicity of the substrate it was immersed into the solution or withdrawn.

For Langmuir-Blodgett and Langmuir-Schaefer transfers 1,2-Dimyristoyl-sn-glycero-3-phosphocholin (DMPC, Fig. 19) (Sigma Aldrich Chemie GmbH, Germany) as well as perdeuterated d54-DMPC (Sigma Aldrich Chemie GmbH, Germany) (Fig. 20) dissolved in chloroform (Sigma Aldrich Chemie GmbH, Germany) was used. The concentration of the lipid in the chloroform solution was 1.0 mg/ml.

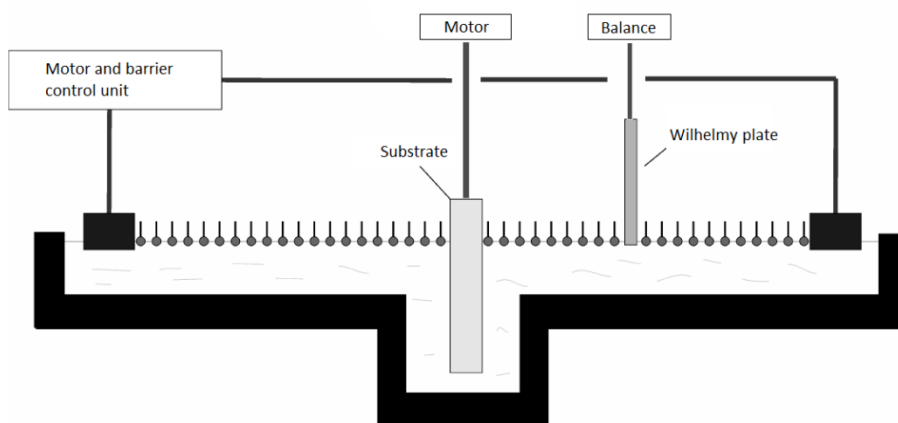


**Figure 18:** Scheme of the Langmuir trough used in this thesis. (Adapted from <sup>[104]</sup>)

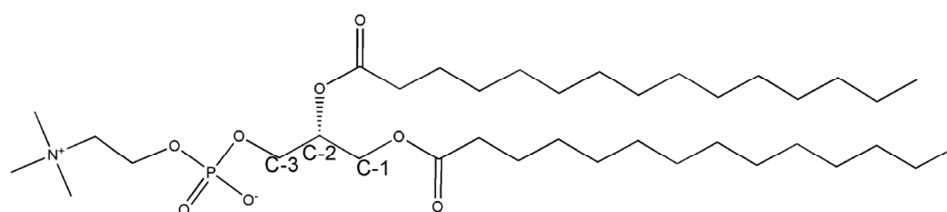


**Figure 19:** Lewis structure of 1,2-Dimyristoyl-sn-glycero-3-phosphocholin (DMPC).

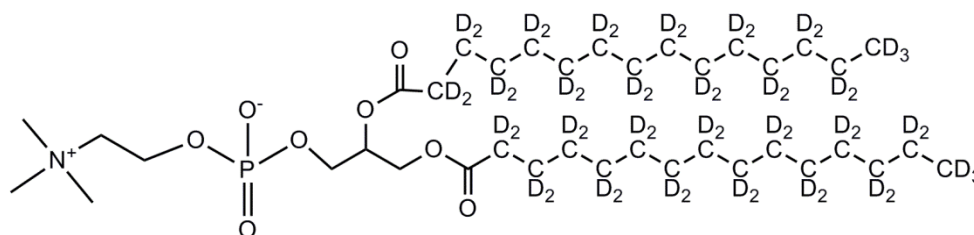


**Figure 20:** Structure of per deuterated d54-DMPC.

Before every experiment, the trough and the barriers were cleaned thoroughly. First they were rinsed with deionized water and ethanol. Then it was swept with a tissue drenched in chloroform followed by rinsing with ethanol and water. The Wilhelmy plate was cleaned by spraying it with ethanol and flame annealing. Small Teflon parts like substrate holders were cleaned for 20 minutes in a UV.TC.EU.003 UV TipCleaner (Bioforce Nanosciences, Inc., Ames, IA, USA). The trough was filled with deionized water until the water level rose slightly above the trough borders. The water surface was cleaned, by moving the trough barriers together and subsequently siphoning off of the surface water layer. The cleanliness of the water was checked by the measurement of the surface pressure at the air water interface. If the surface pressure increased by more than

0.6 mN/m upon compression of the surface, the cleaning procedure would have to be repeated. After retraction of the barriers the trough was ready to start the experiment. A few microliters of the DMPC solution were dropped onto the water surface. The system was left for 10 minutes to evaporate the chloroform. Finally, the barriers were slowly closed (10 mm/min) and the surface pressure was measured in dependence on the surface area. If impurities were present on the surface, the Langmuir isotherm would show irregularities.

It is not possible to transfer a lipid bilayer onto a gold substrate with the Langmuir-Blodgett method <sup>[105]</sup>. Instead a combination of the Langmuir-Blodgett and Langmuir-Schaefer techniques was used. The first layer was transferred at a surface pressure  $\pi = 42$  mN/m with the Langmuir-Blodgett technique. For this the substrate was immersed into the trough prior to spreading the DMPC on the water surface. After formation of an ordered monolayer on the surface, the substrate was slowly (5 mm/min) withdrawn from the water phase. The DMPC monolayer was transferred with its hydrophilic head groups oriented towards the substrate surface (Fig. 21). After drying under argon flow for one hour to remove traces of water in the monolayer the sample was ready for the transfer of the second layer. The Langmuir-Schaefer <sup>[106]</sup>, or horizontal touch, technique was used to transfer the second layer (Fig. 22).

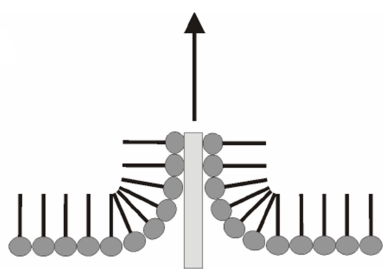


**Figure 21:** Langmuir-Blodgett technique. (adapted from <sup>[104]</sup>)

For the Langmuir-Schaefer technique an ordered DMPC monolayer was formed at  $\pi = 42$  mN/m at the water surface of the Langmuir trough. Then the sample obtained with the Langmuir-Blodgett technique was carefully positioned parallel and close to the water surface (Fig. 22a). It was slowly lowered until contact with the surface occurred (Fig. 22b). After retraction a bilayer was formed on the substrate (Fig. 22c,d).

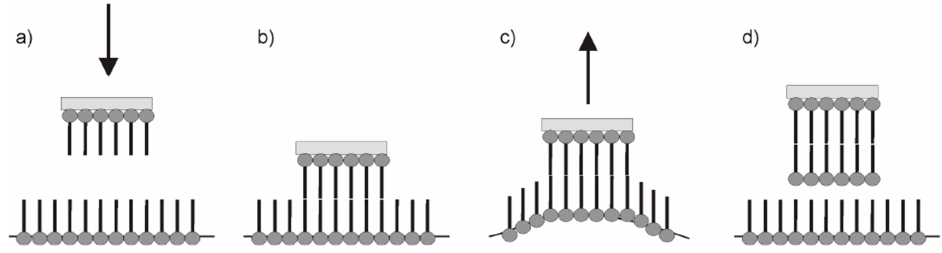


**Figure 22:** Langmuir-Schaefer technique. a) The substrate monolayer is positioned parallel to the water surface with an ordered monolayer on it. b) and c) Substrate and water surface are brought into contact followed by immediate retraction of the substrate. d) Formed bilayer. (Adapted from [104])

### 3.3 Preparation of $\text{TiO}_x\text{C}_y$ Surfaces

The  $\text{TiO}_x\text{C}_y$  surface used in this thesis were produced by Celine Ruediger from the Technical University Munich [107]. Titanium plates were electropolished in 40% perchloric acid mixed with methanol and butoxyethanol. The applied bias was 60 V. A ca. 60 nm thick oxide layer was formed on the polished surface by anodic oxidation in 0.1 M  $\text{H}_2\text{SO}_4$  at 60 V for 10 minutes. The freshly prepared surfaces were transferred into an oven and annealed at 850 °C for 1 hour in an argon atmosphere. To introduce the carbon into the oxide layer 0.1%  $\text{C}_2\text{H}_2$  was streamed over the surface for 5 min. After that the sample was annealed at 850 °C for another hour, followed by a slow cool down. The resulting films are not carbon-doped (which would happen at lower temperatures [108]) but instead a carbon rich Magnèli-type [109] phase with semi-metallic properties is formed [110].

### 3.4 Ellipsometry

For ellipsometric experiments a „real time spectroscopic rotating compensator ellipsometer” (RTSRCE) (Fig. 23) was used. A formal representation of this system can be constructed with the help of Stokes vectors and Mueller matrices. The stokes vector  $\mathbf{S}_i$  describing the incident light is transformed to the Stokes vector  $\mathbf{S}_t$  of the transmitted light by the following equation [111]:

$$\mathbf{S}_t = \widehat{M}_A \widehat{R}(A) \widehat{M}_S \widehat{R}^{-1}(C) \widehat{M}_C \widehat{R}(C) \widehat{R}^{-1}(P) \widehat{M}_P \mathbf{S}_i, \quad (46)$$

where  $\hat{M}_A, \hat{M}_S, \hat{M}_C$  and  $\hat{M}_P$  are the Mueller matrices of the analyzer, the sample, the rotating compensator and the polarizer. The rotation matrices  $\hat{R}(A), \hat{R}^{-1}(C), \hat{R}(C)$  and  $\hat{R}^{-1}(P)$  perform the transformation of  $S$  from a frame of reference to another. The used system is a modified commercially available RCE system (Horiba Jobin-Yvon, France). The beam path contains a polarizer, a rotating compensator (a quarter wave plate made of quartz), a sample and an analyzer. A 75 W xenon lamp was used as a light source. A spectrometer model CP140 from Horiba Jobin-Yvon (France) with a CCD detector (charge coupled device) was applied for the signal detection. This setup allows the recording of ellipsometric data in the 400-800 nm spectral range. All optical components are computer controlled via a serial RS 232 port.

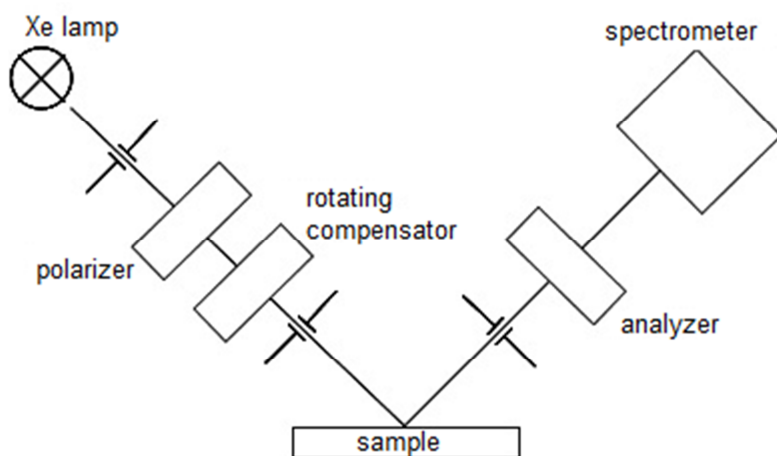


**Figure 23:** Setup for an ellipsometric experiment.

To perform electrochemical and ellipsometric measurements simultaneously, a specifically designed electrochemical cell was used <sup>[111]</sup> (Fig. 24). This cell, with a volume of ca. 100 ml, has three windows made of quartz glass, two of which allow a light beam to pass at an angle of incidence of 66°. The middle window is used for precise positioning of the cell. The three electrode setup consists of a gold covered glass slide as the working electrode (WE), a platinum mesh as the auxiliary electrode (CE) and a Ag|AgCl|3M KCl reference electrode (RE). The electrodes are connected to a Radiometer PGP 24-1 potentiostat/galvanostat. The experimental data are recorded at the analogue output by a data acquisition device (National Instruments PCI-6221) and digitalized for further processing with a computer.

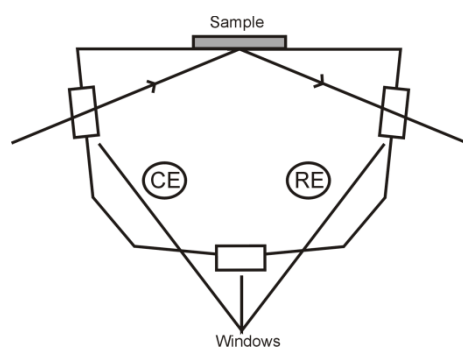


**Figure 24:** Electrochemical cell for ellipsometry.

Before any measurements were conducted the position of the sample and the exact angle of incidence was determined with a goniometer. To estimate the signal-to-noise ratio of the device, spectra were recorded twice at the same spot. Also anisotropic effects were ruled out by rotating the sample by  $90^\circ$  between measurements. A  $3 \times 3$  ellipsometry image was recorded to check the homogeneity of the adsorbed collagen film (Fig. 25).

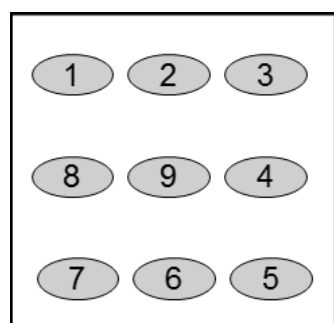


**Figure 25:** Principle of ellipsometry  $3 \times 3$  image measurement. The single spots are marked and numbered.

### 3.4.1 Data Evaluation and Used Models

Ellipsometry is a so called indirect technique, i.e. the desired information is not directly obtained from the measured data but by fitting this data to an optical model.

The experimental data was fitted with the Delta Psi software (Horiba Jobin-Yvon France). Three kinds of optical models were employed. Two of them were built as a three-layer-system (Fig. 26a,b). The substrate was an infinitely thick gold layer, followed by a thin homogeneous collagen layer and an infinite water bulk layer. The difference between the two models was the upper bulk

material. One model used air, the other one water. If this model would be fitted without additional information, nine parameters corresponding to the layers' thicknesses, refractive indices and attenuation coefficients would be unknown. The third model had infinite gold substrate and water bulk layers. But the interface layer was built of a mixture of protein and water with a variable ratio (Fig. 26c). This model would use ten parameters, nine for the three layer materials and an additional one for the interface layer ratio. Some parameters were available from literature (Tab. 9). This significantly reduced the number of fitting parameters and increased the accuracy of the result. However, using literature values always introduces a potentially big systematic error, because the experimental conditions are usually not the same as for the experiments presented here.

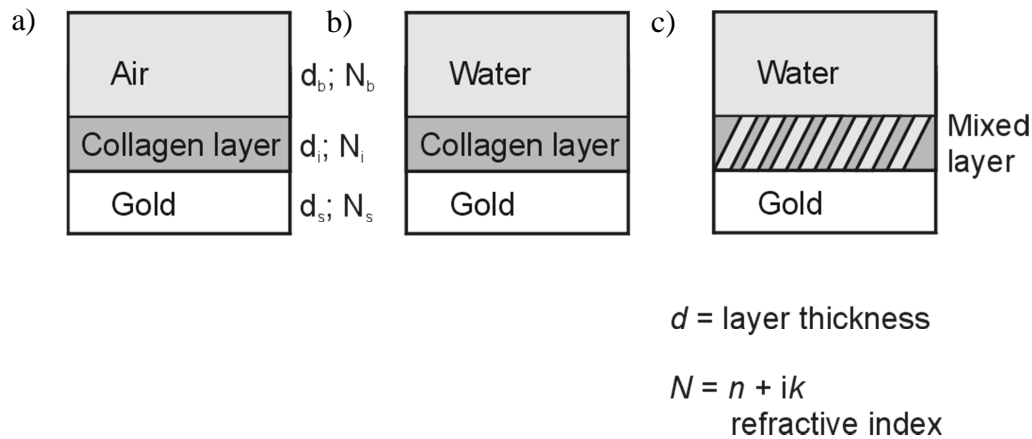


**Figure 26:** Optical models used to fit the data of the ellipsometry experiments.

**Table 9:** Components of the optical models used to fit ellipsometric data and their corresponding fitting parameters

<i>Material</i>	<i>Parameters</i>	<i>Note</i>
Gold, Air, Water	Thickness Dielectric function	Infinite Software Database <sup>[112]</sup>
Collagen	Thickness Refractive index Attenuation coefficient Ratio (Collagen/H <sub>2</sub> O)	Fitted 1.42 <sup>[113]</sup> 0 (transparent film) Fitted

### 3.5 Polarization Modulation Infrared Reflection Absorption Spectroscopy

PM-IRRAS measurements were carried out with a Bruker Vertex 70 IR spectrometer (Bruker Optics, Ettlingen, Germany). Beam modulation was realized with an external PMA 50 module (Bruker Optics, Ettlingen, Germany), which contains a photoelastic modulator model II/ZS50 (Hinds Instruments, Hillsboro, USA), a DSP lock in amplifier model SR830 (Stanford Research Systems, Sunnyvale, USA) and a D313/BQ MCT detector with barium fluoride windows.

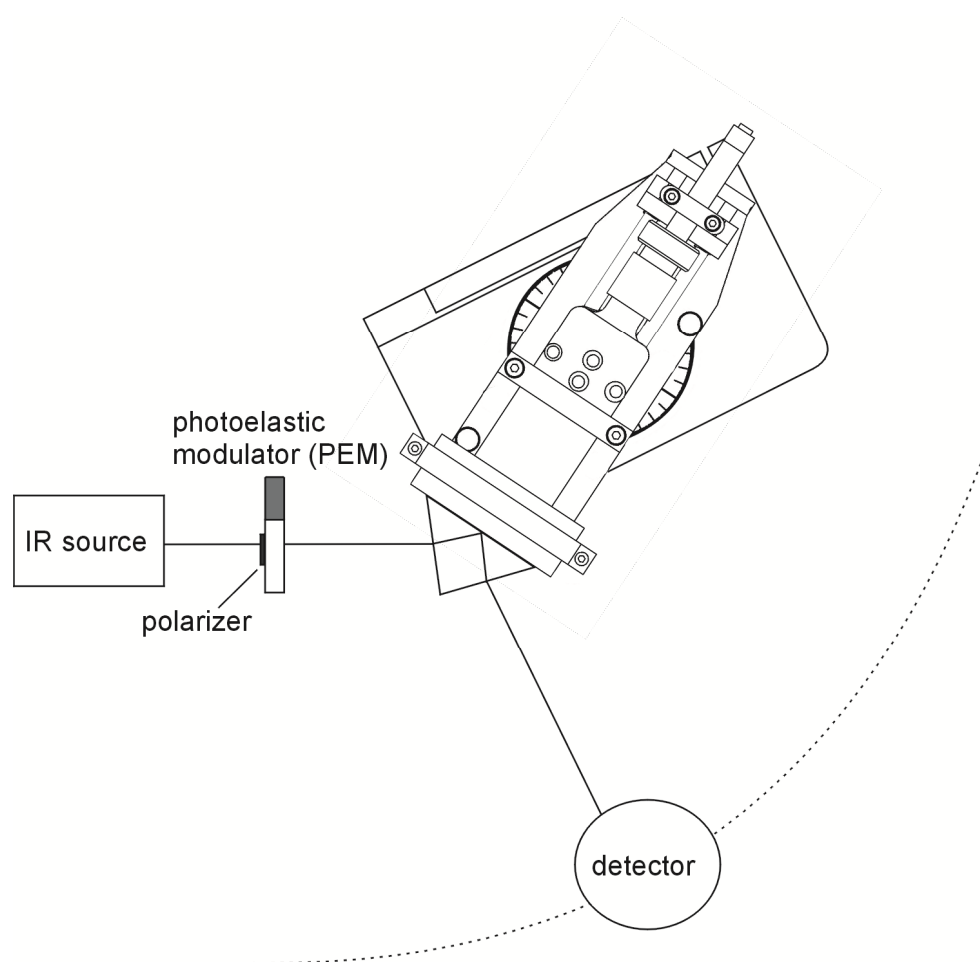


**Figure 27:** PM-IRRAS setup, including the spectroelectrochemical cell (upper right part).

Sample holder and detector are movable to adjust the angle of incidence of the IR beam. All spectra were recorded with a resolution  $4\text{ cm}^{-1}$ . If not mentioned otherwise, an averaging of 2000 spectra was done. The half wave retardation was set to  $1600\text{ cm}^{-1}$  to analyze the amide I band region of the protein and it was set to  $3000\text{ cm}^{-1}$  for CH-stretching and amide A/B modes.

Processing and evaluation of the recorded spectra was realized with the OPUS software version 5.5.1 (Bruker Optics, Ettlingen, Germany). Additional visual basic macros were used to calculate the absorbance spectra and for baseline and intensity correction. The deconvolution of selected bands was carried out with the method described by Singh <sup>[ 114]</sup> employing second order derivatives after 8 point smoothing. The position of band components is determined by the minima of the second order derivative of the PM-IRRAS spectrum in the band region. Besides the band positions three more parameters were used: the band height (intensity), the band width and the band shape. The band heights and full widths at half maximum (FWHM) were allowed to vary freely with the limitation, that all bands had to be similar in width. The band shape could have both Gaussian and Lorentzian components.

A specially designed spectroelectrochemical cell (Fig. 28) was used for measurements at the substrate/electrolyte interface. This cell allows for a potential to be applied at the sample surface during spectroscopic measurements. After insertion of the collagen-covered gold sample and filling of the cell with the electrolyte (NaF solution in D<sub>2</sub>O) it could be purged with argon to remove oxygen from the electrolyte. The electrolyte contained 0.1 mol/l sodium fluoride due to solubility problems with the used BaF<sub>2</sub> prism. Deuterated water was used to minimize the interference of water absorption bands with the vibrational bands of the sample.

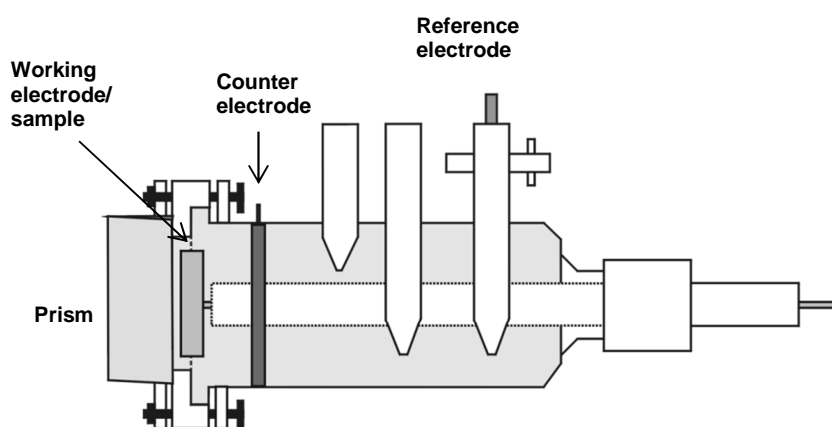


**Figure 28:** Spectroelectrochemical cell for the *in situ* PM-IRRAS experiment.

Additionally, the spectroelectrochemical cell had a glass mantle that could be used to control the temperature of the solution. Most experiments concerning

this thesis were conducted at room temperature (*rt*) (Tab. 10). Because of that, *rt* is chosen as the temperature of reference for experiments under controlled temperature, although it has no physiological importance. The experiments were performed at the following temperatures: at 37 °C because it corresponds to the normal body core temperature of humans, which lies between 36.5 and 37 °C. At 43 °C, the human body breaks down due to protein denaturation. Additionally, Payne <sup>[ 15]</sup> found this to be the temperature at which collagen in aqueous solution irreversibly denaturizes to gelatine. The last temperature level at 50 °C was chosen as a situation in which the collagen was anticipated to have lost its tertiary structure completely.

**Table 10:** Temperature values and their meaning for experimental conditions

<i>Temperature / °C</i>	<i>Note</i>
Room temperature ( <i>rt</i> )	Standard condition for most experiments conducted in this thesis
37	Body temperature
43	Partial denaturation of collagen in solution <sup>[ 15]</sup>
50	Upper reference, complete denaturation <sup>[ 15]</sup>

The spectroelectrochemical measurements were carried out using either fixed potentials or a potential program (Fig. 29), in which the sample was pretreated for 120 seconds at a given potential before recording the spectrum. Three different potentials were used for this program: -0.8 V, 0.0 V and 0.4 V vs. Ag|AgCl. The extreme values give the range at which the gold electrode could be used without electrolysis of the electrolyte whilst at 0.0 V the system was basically allowed to relax.

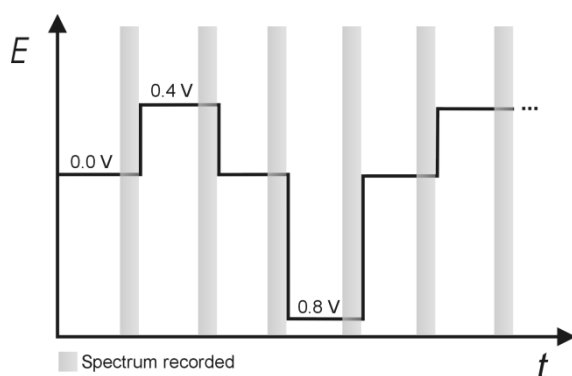


**Figure 29:** Potential program for spectroelectrochemical experiments.

### 3.6 Electrochemical Experiments

For electrochemical measurements a three electrode setup with a gold wire as counter electrode, a silver silver chloride reference electrode (Ag|AgCl|3M KCl) connected to the cell via a salt bridge and a gold disc electrode connected as working electrode to a CH 660a potentiostat (CH Instruments, Austin, USA) was used. The working electrode was employed in the hanging meniscus configuration [ 115] (Fig. 30). The electrode was slightly retracted from the electrolyte surface. Thus, only the modified surface was in contact with the electrolyte solution and edge effects were avoided. For all electrochemical experiments conducted throughout this thesis, the cell was closed and was purged with argon to remove oxygen from the electrolyte solution.

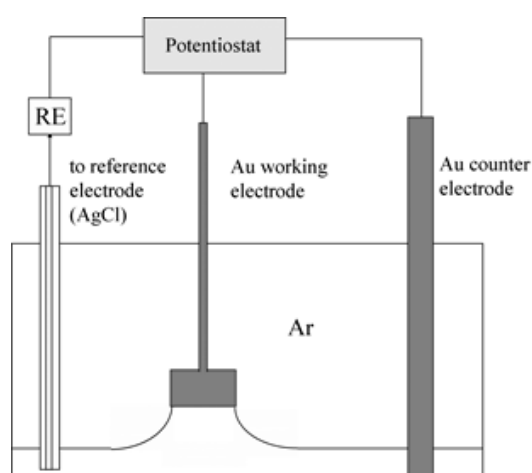


**Figure 30:** Schematic representation of the hanging meniscus configuration for capacitance and charge measurements.

### 3.6.1 Alternating Current Voltammetry

In the AC voltammetry a linear DC sweep is superimposed with a fast oscillating AC signal (Fig. 31). Because the frequency of the AC signal is higher than the step rate of the linear DC sweep, the DC potential  $E_{DC}$  sets up surface concentrations that appear as bulk concentrations to the AC signal. As a result the AC current in dependence on  $E_{DC}$  and the phase difference between the AC currents and the applied AC signal are measured. The main strength of this technique is the precision of the information about electrode processes it can yield.

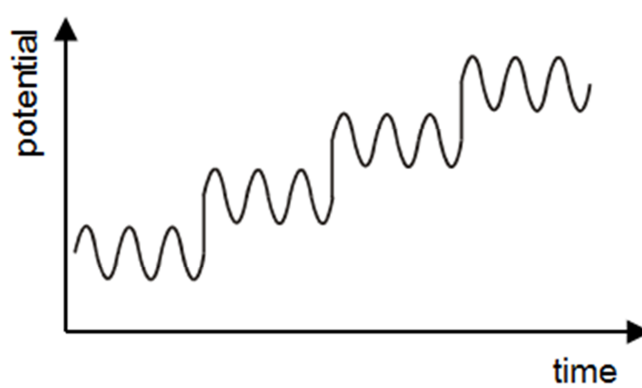


**Figure 31:** Scheme of the excitation signal for linear sweep AC voltammetry

The application of AC voltammetry for the calculation of the capacitance is based on the requirement that the experimental setup behaves as a series of a resistor and a capacitor (Fig. 32, right).  $R_S$  represents the resistance of the electrolyte and  $C_{dl}$  is the capacitance of the electrochemical double layer. Compared to the equivalent circuit of an ordinary electrochemical reaction (Fig. 32, left) no electrochemical reaction takes place at the electrode surface. This means that the charge transfer resistance  $R_{ct}$  is infinitely large. The electrode behaves ideally polarizable over the potential range of the experiment. For the systems that are analysed in this thesis the model is not exactly true at the edges of the potential range due to water electrolysis.

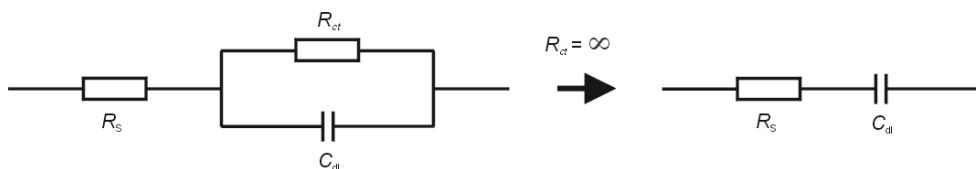


**Figure 32:** Equivalent circuit for an electrochemical cell (left) and the equivalent circuit describing AC voltammetry experiments (right).

With the in-phase current  $i_{in}$  and the out-of-phase current  $i_{out}$  the specific capacitance of the double layer can be calculated with the following equation:

$$C_{dl} = \frac{i_{in}^2 + i_{out}^2}{2\pi i_{out}^2 0.63662 E f A} \quad (47)$$

where  $E$  and  $f$  are the amplitude and frequency of the AC signal and  $A$  is the contact area of the electrode with the electrolyte.

### 3.7 Surface Plasmon Resonance Experiments

For SPR measurements an Autolab Esprit Instrument (Eco Chemie, Utrecht, Netherlands) was used. The instrument is equipped with an open cuvette system of 20-150  $\mu\text{L}$  sample volume <sup>[116, 117]</sup>.

Before every measurement the hemispherical borosilicate prism was cleaned with water and isopropanol. An oil with the same refractive index as the prism was applied to the prism and the sample was deposited with the glass side on the oil covered prism. This prevents an air-filled gap between the prism and the glass slide. The presence of a gap would make the optical model of the setup more complex. Both were transferred to the measurement cell, which was filled with 25  $\mu\text{l}$  of the PBS solution. The plasmon was localized at the reflectivity minimum. The system was left for 30 min to reach equilibrium. After that 25  $\mu\text{l}$  of 0.2 mg/ml collagen solution in PBS were added for an overall collagen concentration of 0.1  $\mu\text{g/ml}$ .

The resulting SPR spectra were fitted with the freely available Winspall software in order to obtain the thickness of the adsorbed collagen film. The optical constants used for the fitting process are listed in Table 11.

**Table 11:** Optical parameters used to fit the SPR spectra.

	$d / nm$	$n$	$k$
glass	0*	1.52	0
gold	50	0.194	3.664
collagen	x	1.42	0
water	0*	1.33	0

\* a thickness  $d = 0$  is interpreted by the software as an infinitely thick layer.



## 4 Results

### 4.1 Collagen-coated Gold Surfaces Characterized in Air

The dependence of the adsorption of collagen films on the adsorption time and on the collagen concentration in the bulk solution was determined. PM-IRRAS at the gold|air interface was used to follow the adsorption process. Considering the structure, size and flexibility of collagen molecules, it can be assumed that they do not form ordered layers on a surface. The extent of this inhomogeneity and the reproducibility of the film formation were investigated by means of PM-IRRAS and ellipsometry. All the analysis was done in air.

#### 4.1.1 Time-Dependence of Collagen Adsorption on Gold

The influence of the adsorption time on the formation of stable collagen films on gold surfaces was investigated. PM-IRRA spectra were employed to follow the collagen film formation for varying times of adsorption. Criteria taken into account are the position and intensity of characteristic amide bands and CH-vibrational modes.

The spectral region from  $3450\text{ cm}^{-1}$  to  $2800\text{ cm}^{-1}$  (Fig. 33a) contains the amide A and amide B bands at  $3331\text{ cm}^{-1}$  and  $3080\text{ cm}^{-1}$ . The bands between  $3000\text{ cm}^{-1}$  and  $2800\text{ cm}^{-1}$  originate from  $\text{CH}_2$ - and  $\text{CH}_3$ -stretching modes of collagen. The PM-IRRA spectra in the wavenumber region from  $1800\text{ cm}^{-1}$  to  $1400\text{ cm}^{-1}$  (Fig. 33b) show the characteristic amide I and amide II bands centered at  $1672\text{ cm}^{-1}$  and  $1555\text{ cm}^{-1}$  as well as the  $\text{CH}_2$ -scissoring band at  $1453\text{ cm}^{-1}$ . The intensity of these signals increases with the adsorption time of the protein. Because the amide I mode is about ten times stronger than all the other signals in the spectrum, its intensity has the best signal to noise ratio and accordingly, is best suited for quantitative analysis. The largest increase in the integrated intensity is observed during the first minutes of collagen adsorption (Fig. 33, inset). The amide I band intensity reaches a plateau after ca. ten minute of adsorption. This indicates a

saturation of collagen on the surface. While the deduction of a saturation process is reasonable, it is not easily possible to obtain surface concentrations from IR spectra because a doubled intensity does not necessarily reflect the same increase in adsorbed collagen. Other factors, like changes in the molecular structure or molecular orientation, can influence the intensity of an IR band [ 15, 118]. In principle, this process could also be an equilibrium between adsorption and desorption of collagen instead of a saturation, but measurements of collagen films stored in PBS for several hours showed almost no loss of the amide I signal intensity. If the collagen adsorption could be described as an equilibrium, the signal intensity should have been decreased due to protein desorption. This result is unexpected because earlier experiments conducted with other biomaterials (titanium alloys) as substrate material indicated that some desorption does in fact take place [ 14, 31].

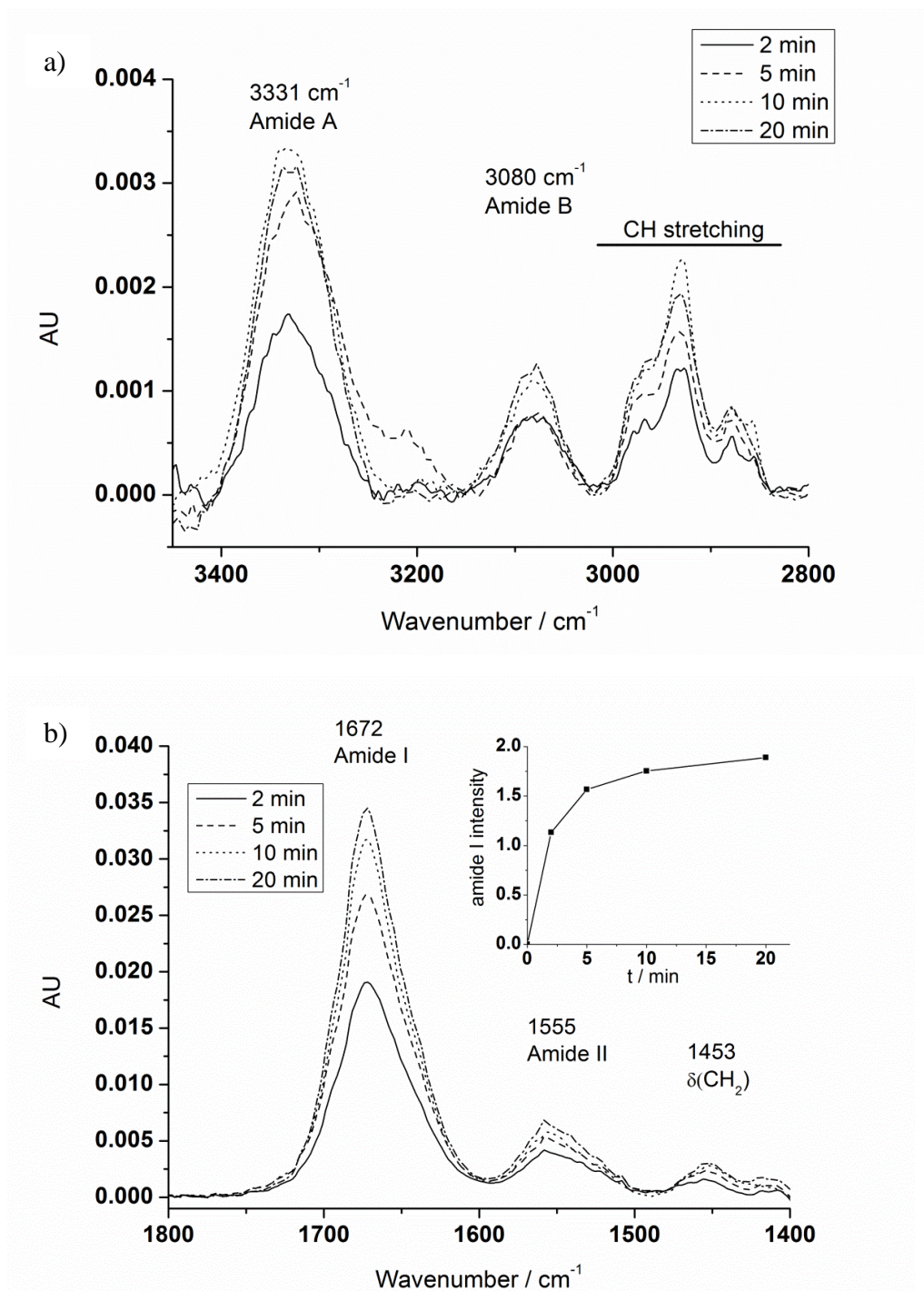


**Figure 33:** PM-IRRA spectra of a) amide A/B bands as well as CH-stretching modes and b) amide I/II bands and  $\text{CH}_2$ -scissoring mode of collagen films on gold after different times of adsorption. The collagen concentration in the bulk solution during adsorption was 0.1 mg/ml. The inset shows the integral signal intensity of the amide I band for varying adsorption times.

#### 4.1.2 Dependence of Collagen Adsorption on Gold on the Collagen Concentration in the Solution

The dependence of the collagen concentration in the bulk solution during adsorption on the formation of adsorbed collagen films was investigated. Figure 34 shows IR spectra recorded of collagen films assembled on gold from solutions of various concentrations for 10 minutes in the spectral region from 3500  $\text{cm}^{-1}$  to 2800  $\text{cm}^{-1}$  (Fig. 34a) and from 1800  $\text{cm}^{-1}$  to 1500  $\text{cm}^{-1}$  (Fig. 34b). The integral amide I band intensities were compared (Fig. 34b, inset). For the lowest concentration (10  $\mu\text{g/ml}$ , dash-dot-dot line) the amide I and amide II signals are very weak indicating that there is only few protein adsorbed on the surface. Increasing bulk concentrations lead to an increase of the amide I band intensities by 125.3% for 50  $\mu\text{g/ml}$  (dash-dot line). If the concentrations 50  $\mu\text{g/ml}$  and 100  $\mu\text{g/ml}$  (dotted line) are compared, the signal intensity increased by 22.5%. There is a small but insignificant decrease in the integral amide I band intensity for higher concentrations (250  $\mu\text{g/ml}$ , dashed line, -1.6%; 500  $\mu\text{g/ml}$ , solid line, -1.2%). The relative changes are given in correspondence to the amide I band intensity obtained for the lower concentration value. No peak shifts are observed.

If the results from concentration-dependent adsorption and time-dependent adsorption measurements are compared, both experiments show a saturation level for the amount of collagen that can adsorb on the gold surface. Higher collagen concentration in the bulk solution, as well as longer times of adsorption, do not result in thicker protein films. The collagen film preparation for all following experiments was conducted from a bulk solution with a concentration 100  $\mu\text{g/ml}$  and over a time period of 10 minutes. This should result in a film with the saturation concentration.

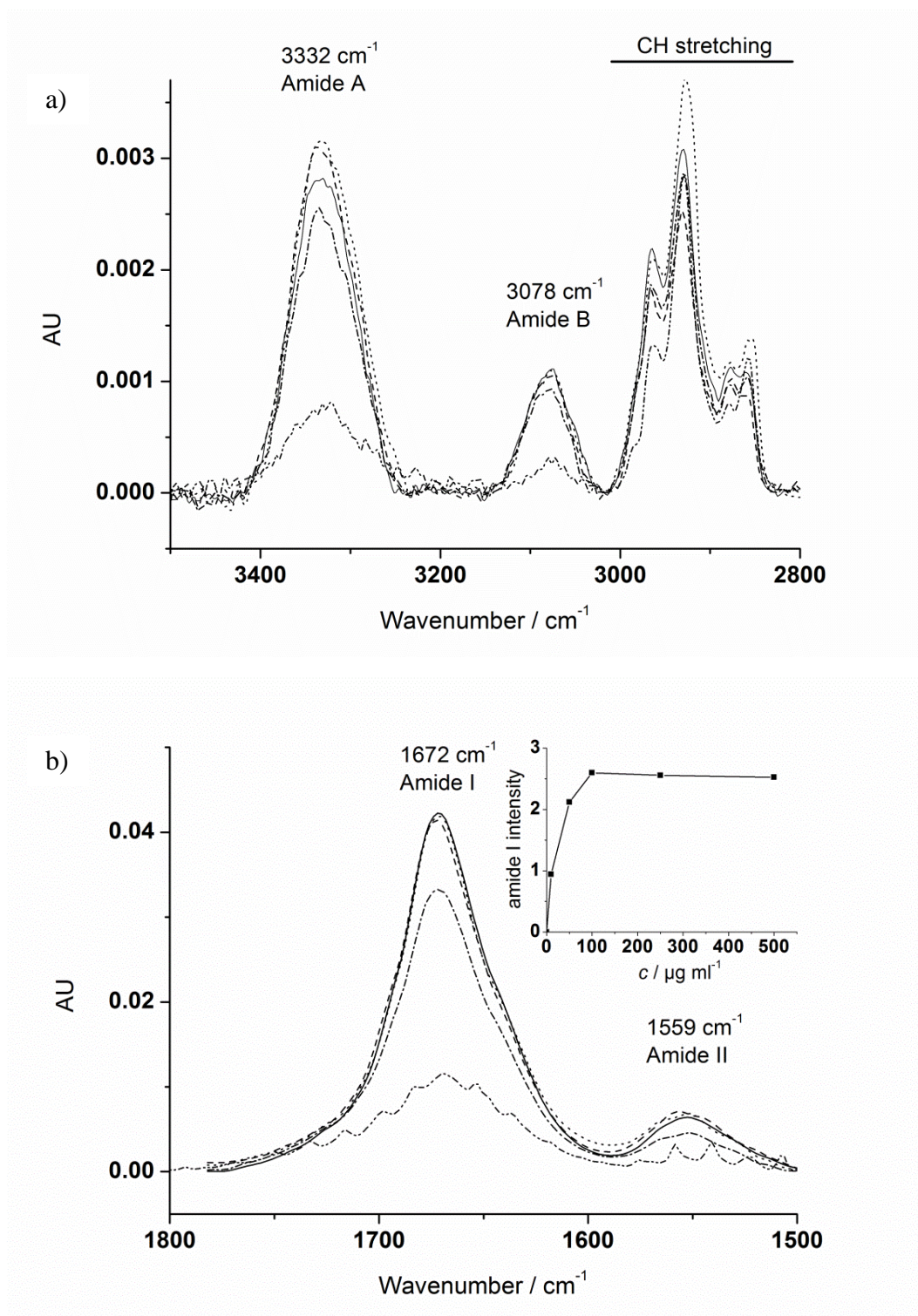


**Figure 34:** PM-IRRA spectra of collagen adsorbed on gold from solutions of various concentrations in: a) the spectral region from 3500 cm<sup>-1</sup> to 2800 cm<sup>-1</sup> and b) the spectral region from 1800 cm<sup>-1</sup> to 1500 cm<sup>-1</sup>. 500  $\mu\text{g/ml}$  (solid), 250  $\mu\text{g/ml}$  (dashed), 100  $\mu\text{g/ml}$  (dotted), 50  $\mu\text{g/ml}$  (dash dot), 10  $\mu\text{g/ml}$  (dash-dot-dot). The adsorption time was 10 min. The inset shows the integral amide I band intensities.

### 4.1.3 Properties of Collagen Films in Air

The PM-IRRA spectra recorded of the collagen films in air are shown in Figure 35 and Figure 36. The two bands at  $3332\text{ cm}^{-1}$  and  $3078\text{ cm}^{-1}$  can be assigned to the amide A and amide B modes respectively (Fig. 35). In comparison to the literature values given in Table 4, both band positions are shifted. The amide A band is shifted to higher, the amide B band to lower wavenumbers<sup>[93,94]</sup>. This can be explained qualitatively by the different environments of the collagen molecules, namely dry films in air in this study and dissolved in aqueous solution in the literature reference. Furthermore, the positions of the amide bands may vary slightly depending on the investigated protein. The wavenumber region from  $3000\text{ cm}^{-1}$  to  $2850\text{ cm}^{-1}$  represents the CH-stretching modes of the collagen molecule. The asymmetric stretching modes of  $\text{CH}_2$ - and  $\text{CH}_3$ -groups are located at  $2929\text{ cm}^{-1}$  and  $2964\text{ cm}^{-1}$  and the symmetric stretching modes of  $\text{CH}_3$ - and  $\text{CH}_2$ -groups are found at  $2878\text{ cm}^{-1}$  and at  $2858\text{ cm}^{-1}$ .

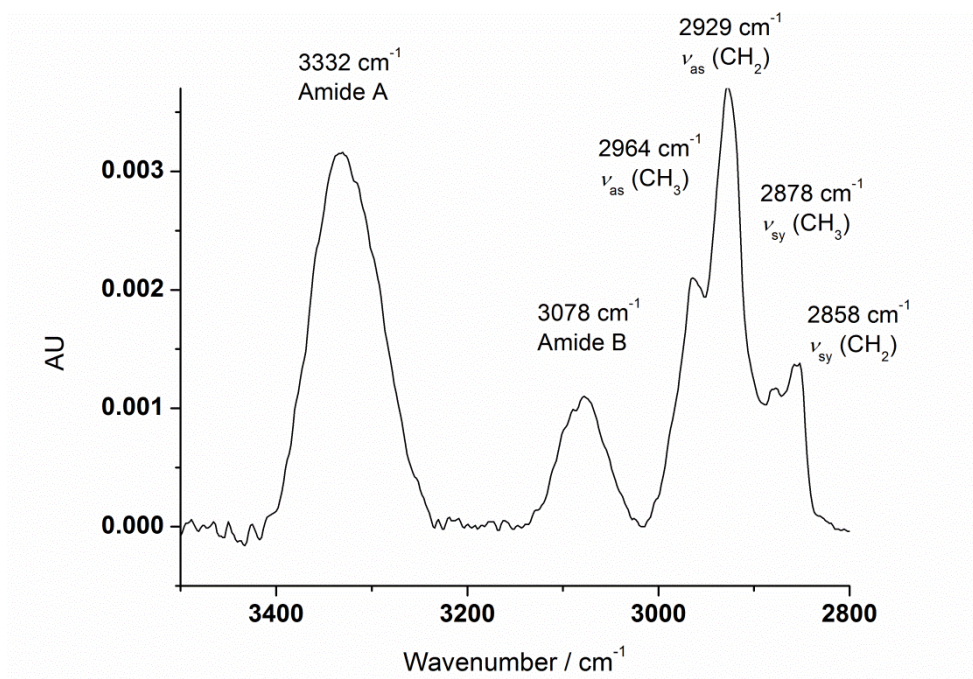


**Figure 35:** The PM-IRRA spectrum in the amide A, B and CH-stretching region of collagen in air. The molecules were adsorbed on gold for 10 min from a solution with a concentration of 0.1 mg/ml. The spectra were recorded in air.

In the spectral region from  $1750\text{ cm}^{-1}$  to  $1400\text{ cm}^{-1}$ , three major IR absorption bands are observed (Fig. 36). The strongest absorption band, centred at

1672  $\text{cm}^{-1}$ , originates from the amide I mode. In comparison to the literature values this band is blue shifted by  $\sim 20 \text{ cm}^{-1}$  [93,94]. The amide II mode is located at 1555  $\text{cm}^{-1}$  and is red shifted by 10  $\text{cm}^{-1}$  compared to the literature values. The weak absorption band at 1453  $\text{cm}^{-1}$  appears due to the  $\text{CH}_2$ -scissoring vibration ( $\delta(\text{CH}_2)$ ).

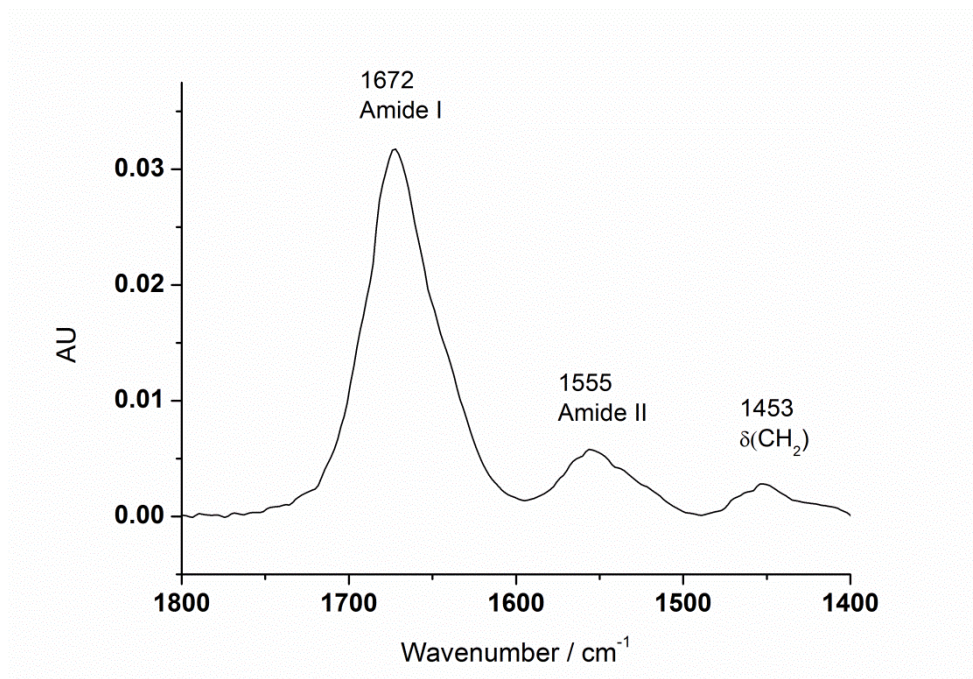


**Figure 36:** The PM-IRRA spectrum in the amide I and amide II region of collagen. The molecules were adsorbed on gold for 10 min from a solution with a concentration of 0.1 mg/ml. The spectra were recorded in air.

The deconvolution of the amide I band was ambiguous. As an example two PM-IRRA spectra of the same collagen-covered surface recorded within two days were compared (Fig. 37a). The differences can be attributed to the background correction and slightly different experimental conditions (temperature, humidity). The second order derivatives of both spectra (Fig. 37b) show three major minima corresponding to components of the amide I band, which agree well with the results of Lazarev et al. [102]. However, the positions of the minima vary slightly for both spectra. The first spectrum (solid line) has three minima at 1637  $\text{cm}^{-1}$ , 1673  $\text{cm}^{-1}$  and 1698  $\text{cm}^{-1}$ . The second spectrum (dashed line) has three minima at 1640  $\text{cm}^{-1}$ , 1674  $\text{cm}^{-1}$  and 1695  $\text{cm}^{-1}$ . Comparison of seven PM-IRRA spectra of collagen films adsorbed on gold in air lead to the following average peak positions: 1696.1  $\text{cm}^{-1} \pm 1.7 \text{ cm}^{-1}$ ; 1673.7  $\text{cm}^{-1} \pm 2.1 \text{ cm}^{-1}$ ; 1637.7  $\text{cm}^{-1} \pm 1.6 \text{ cm}^{-1}$ . Peak shifts of a few  $\text{cm}^{-1}$  lie well within the errors margins, thus larger shifts of at

least several  $\text{cm}^{-1}$  are necessary to indicate changes in the state of the collagen film.

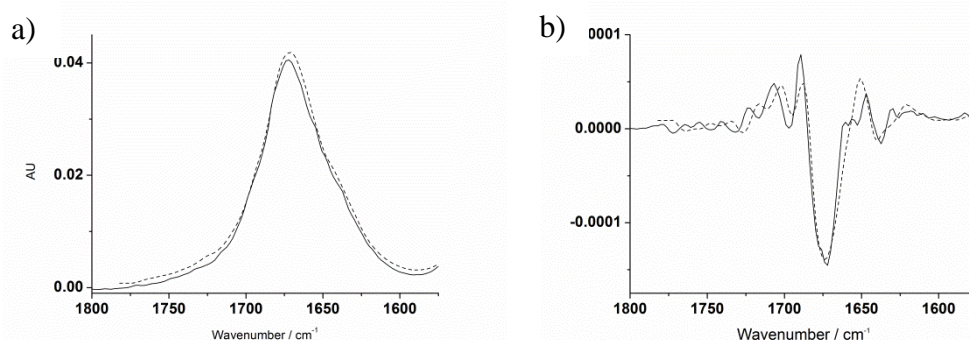


**Figure 37:** a) Two PM-IRRA spectra of a collagen covered gold surfaces. The molecules were adsorbed from a 0.1 mg/ml solution for 10 min. b) Second order derivatives of the spectra after 8 point smoothing.

The resulting bands after amide I band deconvolution are shown in Figure 38 for one exemplary spectrum. This fit used only the band positions as fixed parameters leading to an unreasonably small FWHM for the band at  $1698 \text{ cm}^{-1}$ . A physically more reasonable fit is obtained if all bands have similar FWHMs (Fig. 39,  $\text{FWHM} = 40 \text{ cm}^{-1} \pm 2 \text{ cm}^{-1}$ ). The margins were set in accordance with the results of Lazarev et al. <sup>[102]</sup>. The band shapes were fitted with a mixed Lorentzian and Gaussian function. Purely Lorentzian band shapes apply typically to molecules in the gas phase, where the incoherence due to rotation and collisions plays a strong role <sup>[119]</sup>. Gaussian band shapes on the other hand are usually correlated to solid samples, where the relaxation of the excited states occurs before incoherence becomes a significant factor. The application of a mixed Gaussian and Lorentzian band shape was sensible because the properties of adsorbed collagen molecules lie between a perfect solid state and a gas phase. Although the band shapes tended to have a higher Gaussian fraction, the shapes varied between purely Gaussian and purely Lorentzian. This occurred probably due to the uncertainty in the background correction of the original spectra leading to different band shapes and the complex structure of the amide I band, where no reference to simpler bands was easily available. The average band intensity and integral intensity for the three major amide I band components obtained from the PM-IRRA spectra of seven collagen-covered gold surfaces after deconvolution, are listed in Table 12. The most significant difference to the deconvolution results of Lazarev et al. <sup>[102]</sup>

(Fig. 17) is the weak band centered at  $1696\text{ cm}^{-1}$ , which they attributed to amino acid C=O groups H-bonded to water. However, from the IR-spectroscopic data no explanation for the significant decrease in the integral intensity of only one amide I band component could be obtained. The strongest band at ca.  $1674\text{ cm}^{-1}$  is attributed to C=O groups that participate in interhelical H-bonds indicating that the collagen molecules do not denaturate during adsorption. The band around  $1638\text{ cm}^{-1}$  is correlated to imino acid C=O groups (like Pro and Hyp), which would be H-bonded to water in an aqueous environment. The slight differences in the original spectra, due to different experimental conditions and uncertainties in the background correction, lead to relatively large deviations in the fit results of the amide I band deconvolution. Because of this high relative error in the analysis of spectra with small differences, deconvolution will only be used in this thesis when the amide I band changes significantly (see 4.2.1). The relatively large error margins for the different fit parameters might also explain why, to the author's knowledge, no studies on collagen exist that take all the fit parameters explicitly into account for their amide I band deconvolution. The sensitivity of ordinary IR instruments might not be high enough to obtain reproducible and exact data of complex molecules.

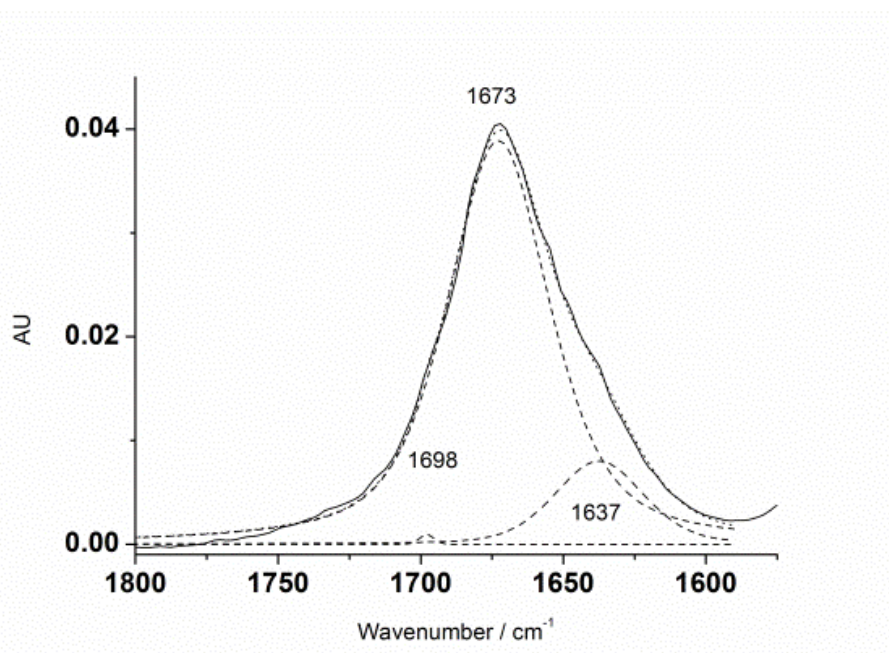


**Figure 38:** Deconvolution of the amide I band of a collagen-covered gold surface. Only the peak positions were used as fixed parameters for the fit. The band intensities, FWHMs and the mixed Gaussian and Lorentzian band shapes were allowed to vary freely. The solid line represents the original spectrum, dashed lines correspond to the three major components of the amide I band and the dotted plot is the sum of the single bands.

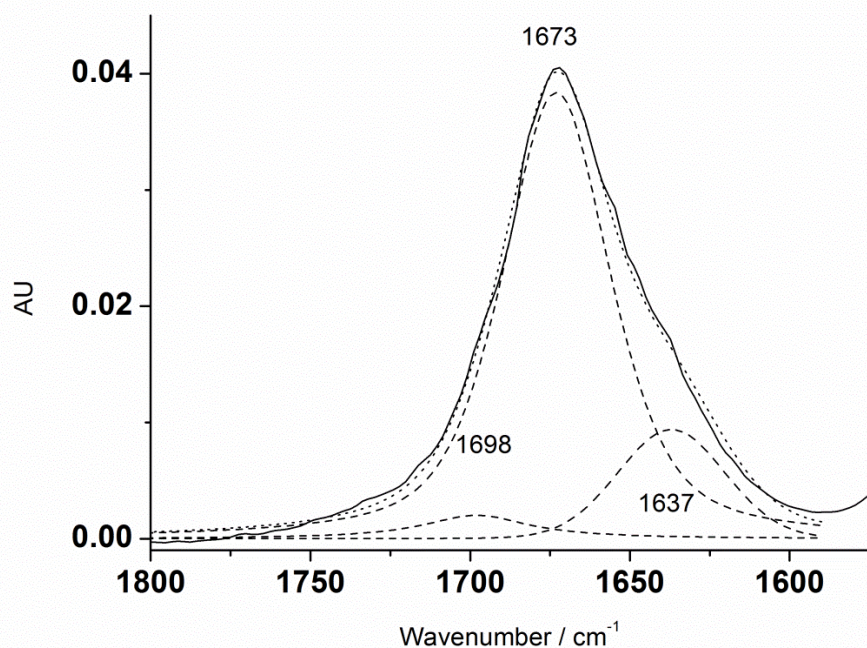


**Figure 39:** Deconvolution of the amide I band of a collagen-covered gold surface. The peak positions were used as fixed parameters and the FWHMs ranged around  $40 \text{ cm}^{-1} \pm 2 \text{ cm}^{-1}$ . The band intensities and the mixed Gaussian and Lorentzian band shapes were allowed to vary freely. The solid line represents the original spectrum, dashed lines correspond to the three major components of the amide I band and the dotted plot is the sum of the single bands.

**Table 12:** Average fit Results for the amide I band deconvolution.

<i>Band component position / <math>\text{cm}^{-1}</math></i>	<i>Average intensity</i>	<i>Average integral intensity</i>
1696	$0.0023 \pm 0.0022$	$0.131 \pm 0.134$
1674	$0.0514 \pm 0.0156$	$2.488 \pm 0.587$
1638	$0.0146 \pm 0.0054$	$0.753 \pm 0.324$

Ellipsometry experiments were performed to determine the thickness of the adsorbed protein film. The experimental data were fitted with the three layer optical model shown in Figure 26a. For ten samples the obtained film thicknesses varied between  $d_{\min} = 3.1 \text{ nm}$  and  $d_{\max} = 6.7 \text{ nm}$  with an average  $d_{\text{av}} = 4.8 \text{ nm} \pm 1.8 \text{ nm}$ . Additionally, a low resolution ellipsometry image consisting of nine data points (3x3) was recorded to estimate the variation of film thickness on one substrate (Fig. 40). The measured thickness of the collagen film varied between 4.4 nm and 6.8 nm with an average of  $5.5 \text{ nm} \pm 0.9 \text{ nm}$ .

The average film thickness is higher than it would be expected for an ordered monolayer of collagen molecules adsorbed along their long axis (1.5 nm). Together with the high variation of thicknesses for different samples and also for

different spots on one sample, the formation of an inhomogeneous protein film is suggested. The molecules lie unordered on the surface. A good visualization appears to be the image of spaghetti randomly strewn over a surface. Wolf-Brandstetter<sup>[31]</sup> was able to record atomic force microscopy images of adsorbed collagen films on titanium surfaces and collagen dimers on mica that agree very well with these results.

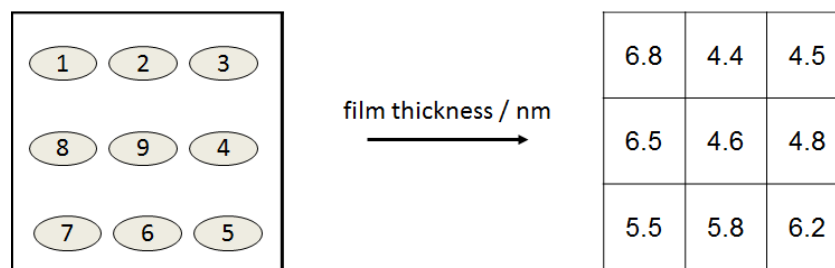


**Figure 40:** Film homogeneity of collagen on gold analyzed via “imaging” ellipsometry. The spots on the left depict the nine positions of the light beam.

However, the variability of the collagen film thicknesses complicates the comparability of results for different samples. This means that absolute values given in the following sections have to be considered with some caution. Instead, the focus of this thesis lies on the investigation of the qualitative behaviour of adsorbed collagen films under the influence of electric fields.

After the determination of the parameters for the adsorption of a collagen film on the gold substrate, its stability was tested. Figure 41 shows the amide I bands of a collagen film adsorbed on a gold surface for 10 minutes from a bulk concentration of 100 µg/ml. One spectrum was recorded directly after the film preparation (solid line) the other one was recorded after about 3 weeks of storage in air (dashed line). The amide I band was chosen as an indicator, because its components can be linked to structural elements of the molecule and the band intensity allows qualitative deductions about the amount of the adsorbed protein (Chapter 2.5.2). The spectra overlap, indicating that the collagen films are very stable in air over long periods of time and no structural, chemical or orientational changes occur.

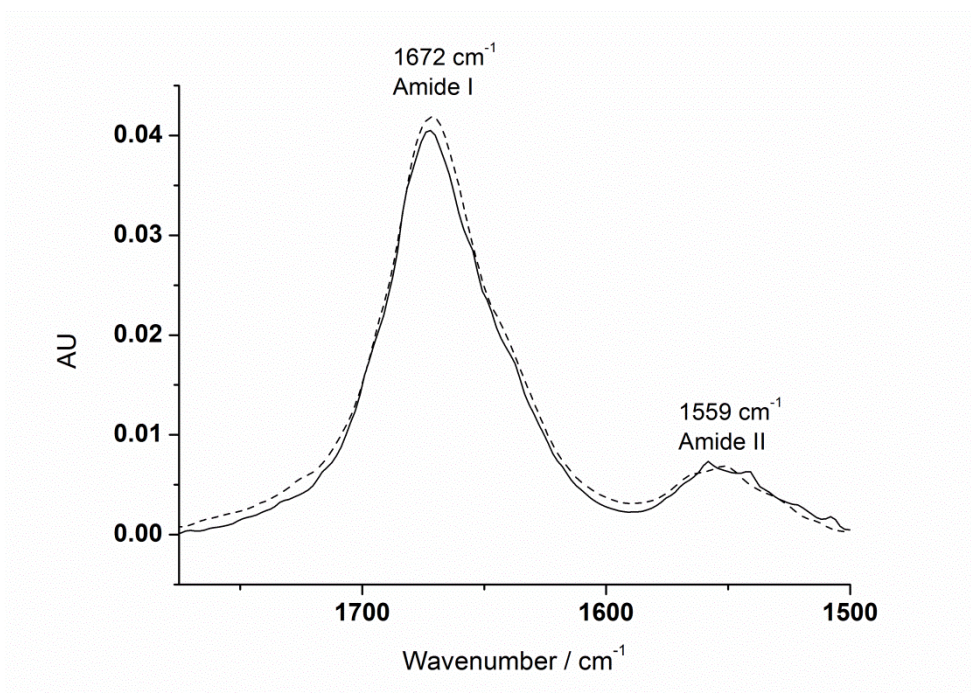


**Figure 41:** The PM-IRRA spectrum in the amide I region of a freshly adsorbed collagen film (solid line) and of the same film after 3 weeks of storage in air (dashed line). The molecules were adsorbed on gold for 10 min from a solution with a concentration of 0.1 mg/ml. The spectra were recorded in air.

## 4.2 Characterization of Collagen Films Adsorbed on Gold in Contact with an Electrolyte Solution

In the next step the behaviour of the collagen film in contact with an electrolyte solution was studied. The most suitable candidates would be solutions with a composition and pH similar to body fluids, like a phosphate buffered saline (PBS) [7, 8] or simulated body fluid (SBF) [119]. Several arguments speak against their use. The prism used in the spectroelectrochemical measurements (Fig. 28) is made of barium fluoride and starts to dissolve in the absence of fluoride ions in the solution. Additionally, the adsorption of Cl<sup>-</sup> ions from the solution on the gold surface would interfere with electrochemical measurements. Due to the strong IR absorption bands of water in the spectrum it is necessary to use D<sub>2</sub>O instead of H<sub>2</sub>O as the solvent. Moreover, ions present in the PBS and SBF solutions absorb IR radiation and would complicate the analysis. Thus, a 0.1 M NaF solution in water was chosen as the electrolyte solution.

#### 4.2.1 Properties of a Collagen Film on Gold in Contact with an Electrolyte Solution at OCP

IR spectra of collagen films on the gold electrode surface in contact with electrolyte (NaF/D<sub>2</sub>O) were recorded at OCP (open circuit potential, 0.2 V vs. Ag|AgCl|3M KCl). Figure 42 shows the PM-IRRA spectra in the region from 1750 cm<sup>-1</sup> to 1400 cm<sup>-1</sup> of a collagen film in the electrolyte solution (dashed line) in comparison to a dry sample (solid line). The three characteristic bands in this region are present: amide I at 1657 cm<sup>-1</sup>, amide II at 1568 cm<sup>-1</sup> and CH<sub>2</sub>-scissoring vibration at 1463 cm<sup>-1</sup>. The amide I band in contact with electrolyte is red-shifted by 15 cm<sup>-1</sup> compared to a dry film. The amide II band is blue-shifted by 10 cm<sup>-1</sup> and the CH<sub>2</sub>-scissoring mode by 11 cm<sup>-1</sup>. It was noted earlier, that the positions of these bands for dried samples do not coincide with the positions found in the literature, where collagen was analyzed in solution<sup>[93, 94]</sup>. The band positions of collagen in contact with the electrolyte solution exactly fit the literature values. This can be explained by the hydration of the collagen molecules in the film. H-bonds formed between the amide C=O and water reduce the strength of the C=O double bond and decreases the energy needed to excite the vibration. This shifts the amide I band to lower wavenumbers. The formation of H-bonds also shifts the NH bending modes to higher frequencies<sup>[120]</sup>.

The same analysis is not possible in the spectral region from 3500 cm<sup>-1</sup> to 2800 cm<sup>-1</sup>. Figure 43 shows the PM-IRRA spectrum in this region for a collagen film in contact with the electrolyte. The signal-to-noise ratio in this region is much lower compared to the amide I band. The only band that can be distinguished here is the amide A band centered at 3332 cm<sup>-1</sup>. The amide B band, expected at 3082 cm<sup>-1</sup>, is not visible in the spectrum. The CH-stretching modes, present between 3000 cm<sup>-1</sup> and 2800 cm<sup>-1</sup>, have a very irregular shape. The sensitivity of the PM-IRRAS appears not sufficient to obtain reasonable information from these signals.

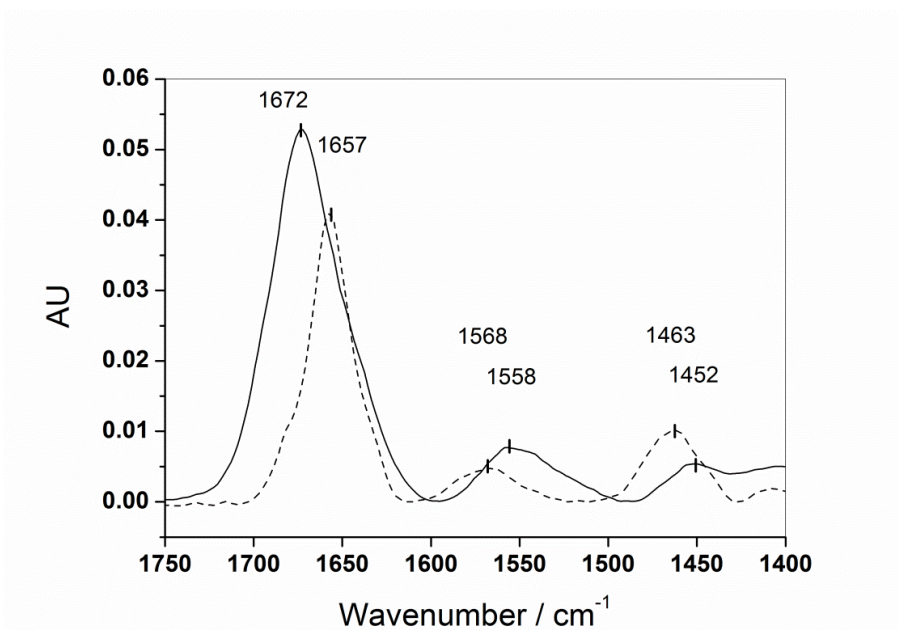


**Figure 42:** PM-IRRA spectra of the amide I/II region of a collagen-covered gold surface in contact with air (solid line) and in contact with electrolyte (dashed line). The molecules were adsorbed on gold for 10 min from a solution with a concentration of 0.1 mg/ml.

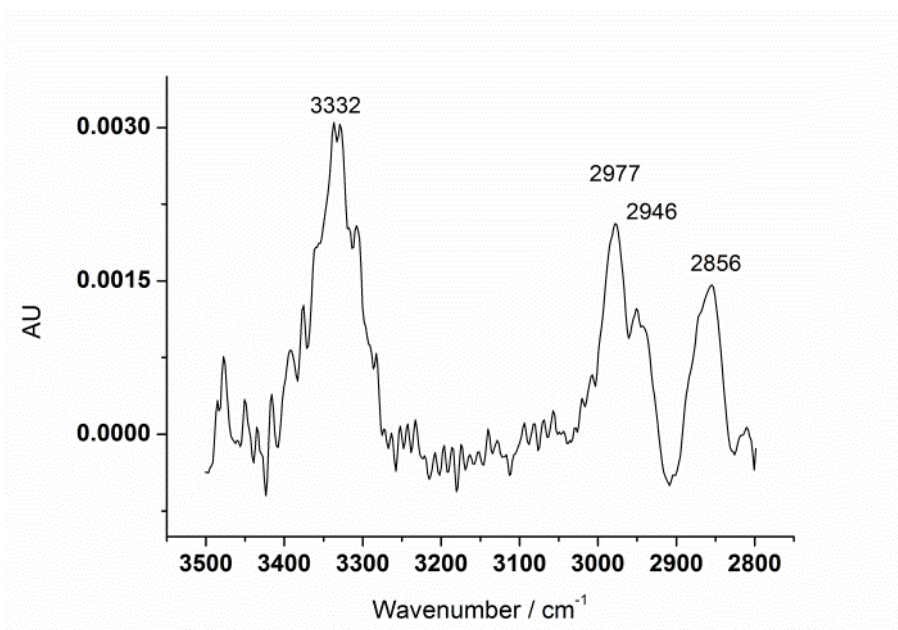


**Figure 43:** PM-IRRA spectra of a collagen-covered gold surface in contact with electrolyte. The amide B band ( $3080\text{ cm}^{-1}$ ) is not visible. The CH-stretching modes ( $2850\text{ cm}^{-1}$  -  $3000\text{ cm}^{-1}$ ) are distorted. Only the amide A band ( $3332\text{ cm}^{-1}$ ) is distinguishable. The molecules were adsorbed on gold for 10 min from a solution with a concentration of 0.1 mg/ml.

The deconvolution of the amide I band results in three major band components at  $1632\text{ cm}^{-1}$ ,  $1658\text{ cm}^{-1}$  and  $1684\text{ cm}^{-1}$  (Fig. 44). Their positions and intensities agree much better with the results of the deconvolution conducted by Lazarev et al. <sup>[102]</sup> compared to the deconvolution of the amide I band of a dry collagen film

on gold. Deviation of the peak positions by a few  $\text{cm}^{-1}$  and differences in the peak intensities are within the limits of experimental uncertainty as shown above (4.1.3). These results indicate that the collagen molecules adsorbed on the gold surface in contact with the electrolyte solution are in the same state of hydration and conformation as collagen in solution.

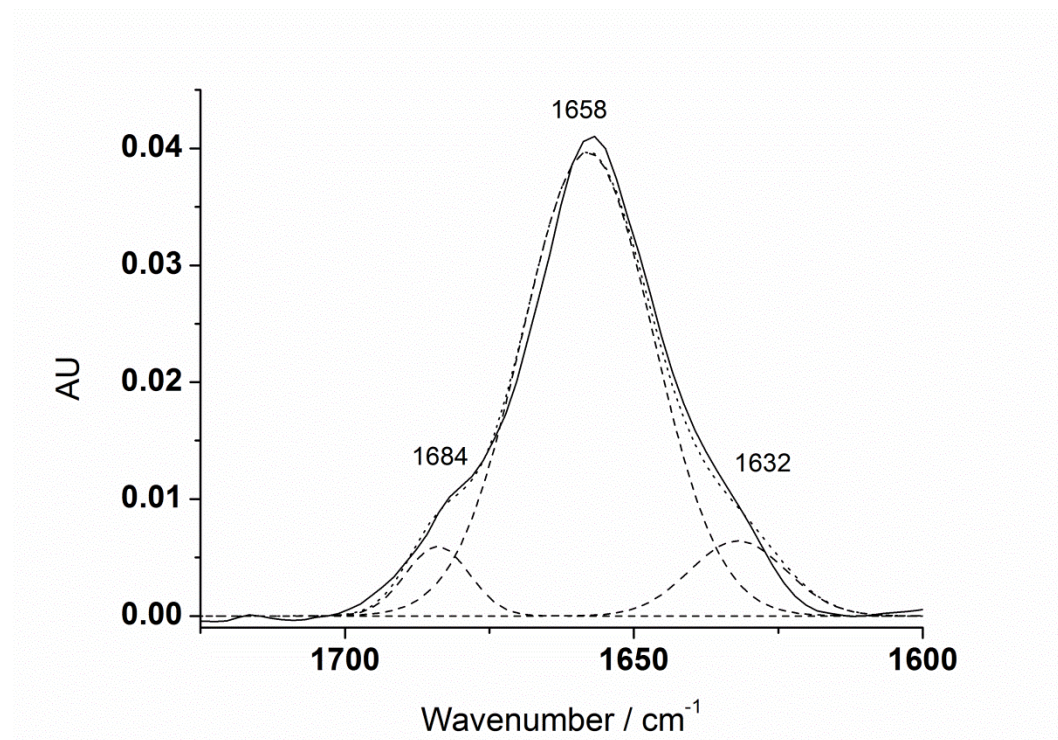


**Figure 44:** Deconvolution of the amide I band of a collagen film adsorbed on gold in contact with the electrolyte solution. The solid line shows the original spectrum, dashed lines correspond to the three major components of the amide I band and the dotted plot is the sum of the single bands. The molecules were adsorbed on gold for 10 min from a solution with a concentration of 0.1 mg/ml.

SPR measurements provided the thickness of the collagen film adsorbed on the gold surface in contact with the PBS solution. For six different samples the obtained thicknesses of adsorbed collagen films ranged from 2.7 nm to 5.6 nm with an average of  $4.3 \text{ nm} \pm 1.1 \text{ nm}$  (Tab. 13). These values are comparable to the thickness of dry collagen films on gold as determined by ellipsometry above. Again, the variability of the results points to the formation of inhomogeneous films with partial surface coverage.

**Table 13:** Thicknesses of collagen films adsorbed on gold surfaces in contact with the electrolyte solution. The results were provided by SPR measurements.

<i>Sample number</i>	<i>Thickness of collagen film /nm</i>
090918_1400	2.7
090918_1535	3.5
090918_1720	4.8
090921_1823	4.1
090923_1228	4.9
090923_1434	5.6

## 4.2.2 Capacitance and Ellipsometry Measurements of Collagen Films on the Gold Electrode Surface

The capacitance of the electrochemical double layer at the gold|electrolyte interface was measured for an unmodified, clean gold electrode (Fig. 45, solid line) and for a collagen-covered gold surface (dashed line). In the potential range from 0.4 V to -0.7 V the collagen-covered sample shows a significantly decreased capacitance. The insulating collagen layer on the surface decreases the thickness of the electrochemical double layer and reduces the capacitance of the gold surface. At potentials  $E < -0.7$  V the capacitances of both samples start to increase strongly. This is an artifact introduced by the onset of H<sub>2</sub>O electrolysis. If the results are compared to other biomimetic systems, which are applied in research, e.g. lipid bilayers <sup>[ 121, 122]</sup> (Fig. 45, dotted line), some differences are observed. The capacitance of a collagen-covered gold electrode is ca. 20  $\mu\text{F}/\text{cm}^2$ . Compared to a transferred lipid bilayer (2-5  $\mu\text{F}/\text{cm}^2$  <sup>[ 121]</sup>) this indicates that the collagen film does not completely cover the gold surface. It appears less homogenous with defects, which allow the incorporation of the electrolyte into the film. Another important difference is that the capacitance of a collagen-covered sample does not coincide with the capacitance of an unmodified surface at potentials  $E < -0.7$  V. Both plots behave independently in almost the whole potential region and overlap only around  $E = -1.0$  V, when the H<sub>2</sub>O electrolysis starts. For a lipid bilayer adsorbed on gold, a potential exists at which the capacitance suddenly changes and starts to resemble an unmodified gold surface <sup>[ 122]</sup>. This is attributed to a complete desorption of the bilayer from the electrode surface. Because collagen

does not show this feature in its capacitance curves it can be concluded, that no potential-induced desorption takes place.

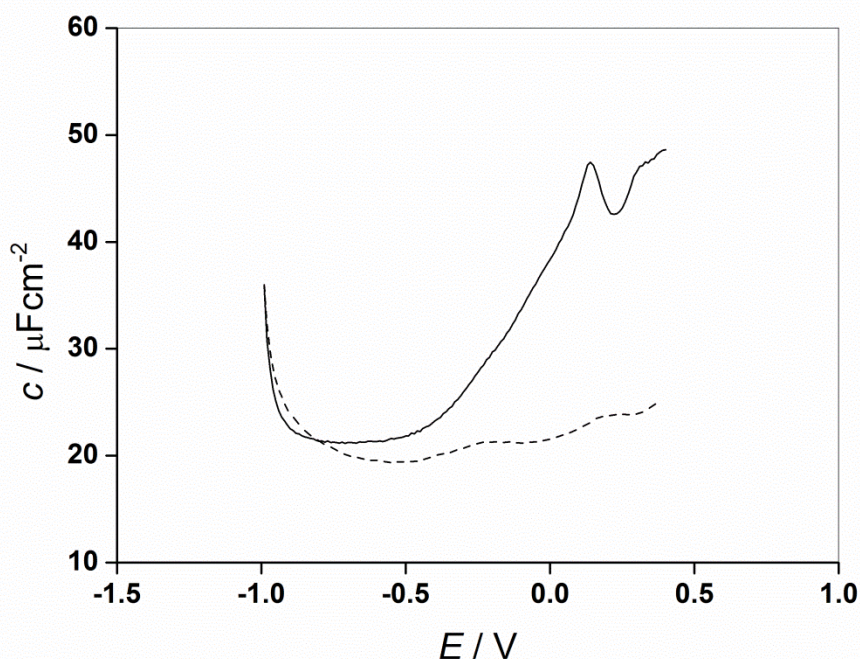


**Figure 45:** Capacitance of an unmodified gold surface (solid line) and a collagen covered gold surface (dashed line) in 0.1 M NaF solution. The molecules were adsorbed on gold for 10 min from a solution with a concentration of 0.1 mg/ml.

Ellipsometry enables *in situ* and real time observation of the sample immersed in the electrolyte solution by fitting the experimental data to an optical model. The fitting procedure introduces several parameters. Each parameter is associated with a statistical uncertainty but also with potential systematic errors, because the physical model only approximates the complex structure of a real sample. More complex systems need more parameters for their description (see Fig. 46a-c). It can be said that the more parameters are used for the fitting the higher the statistical uncertainty of the results. Hence, the number of introduced parameters should be kept to a minimum required to reflect the essential sample properties. This can be done either by choosing only the simplest possible models or by determination of some parameters by independent experiments, or literature values. The fitting process itself is limited in its precision, too.

Two sources of systematic errors arise when dealing with very thin films in the monolayer or sub-monolayer range. The systems presented so far assumed homogeneous layers. However, sub-monolayer systems do not fulfil this assumption (Fig. 46d). This means that conventional data treatment would result

in a film thickness  $d_{\text{eff}}$  lower than the molecular diameter (Fig. 46e). A different approach uses a mixed interface layer consisting of the film material and the bulk material (Fig. 46f). The ratio between the two components describes how much of the substrate surface is covered with the film. The second problem is, that the resolution of the instrument is not high enough to determine both  $d$  and  $N$ . Instead only the product  $dN$  can be deduced. For transparent films ( $k = 0$ ) this product becomes  $dn$ , which is often referred to as the optical thickness.

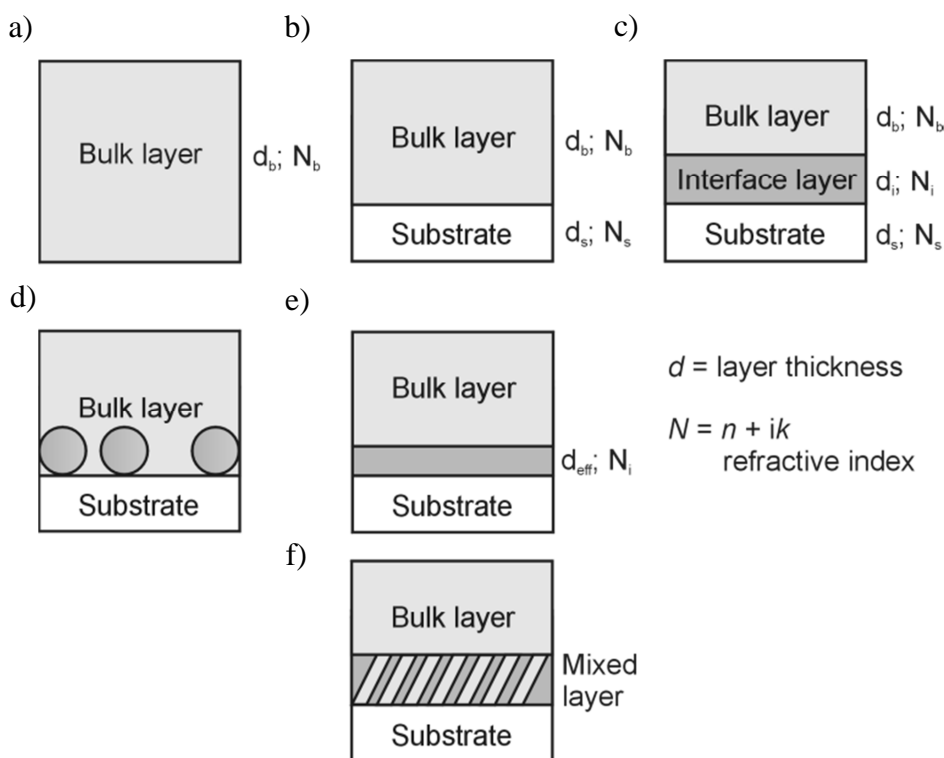


**Figure 46:** a)–c) increase in parameters for more complex optical model systems. d) a sub-monolayer system and possible solutions for modeling e) and f). e) has an effective layer thickness  $d_{\text{eff}}$  smaller than the molecular diameter. f) introduces a mixed layer with variable composition.

In Table 14 the results of the *in situ* ellipsometry experiment are given. The error values in this table correspond to the fitting process and describe the range of values that would fit the tolerance margin of the software.  $\chi^2$  indicates the difference between experimental and calculated curves. The data evaluation was carried out with the help of two different optical models. The first model is composed of a three layer system similar to the illustration in Figure 46c. Upon immersion of the collagen-covered gold surface the thickness of the film seemed to decrease from 6.3 nm in the dry state to 2.5 nm. This would indicate desorption of the collagen from the gold surface. Interestingly, after removal of the

electrolyte and drying of the sample the thickness of the protein film is 6.3 nm, the same as at the beginning of the experiment. The contradiction of experimental data and chosen optical model system lead to the development of the model shown in Figure 46f, consisting of bulk electrolyte and substrate layers and a mixed protein-electrolyte layer at the interface. The thickness of the collagen film was assumed to be constant and equal to 6.3 nm, because no substantial desorption took place. The  $x^2$  values corresponding to the fits of both models are comparable but the second model is physically more reasonable. With the help of this model, the experimental data can be explained as an incorporation of the electrolyte into the protein film.

Ellipsometric results correspond well to the PM-IRRAS analysis presented above. The increased hydration of the collagen molecules due to the incorporation of the electrolyte solution into the protein film explains the shifts of the amide I and amide II bands. In conclusion, IR spectroscopic and ellipsometric data support the model of a disordered, porous collagen film on the substrate that, upon contact, incorporates the electrolyte solution.

**Table 14:** Comparison of two models used to determine collagen film properties for a wet and a dry sample

<i>Optical Model</i>	<i>d/nm</i>	<i>x<sup>2</sup></i>	<i>Electrolyte content / % Vol.</i>	<i>x<sup>2</sup></i>
Three layers dry (Fig. 46c)	6.3 ± 0.2	1.03	-	-
Three layers in electrolyte	2.5 ± 0.3	0.26	-	-
Mixed interface layer in electrolyte (Fig. 46f)	6.3	-	37.1 ± 4.6	0.27

### 4.2.3 Stability of Collagen Adsorbed on Gold in Contact with an Electrolyte Solution

Two spectra were recorded in the spectroelectrochemical cell directly after filling the cell with the electrolyte and after about 300 minutes at open circuit

potential (OCP). Figure 47 shows the amide I bands of both spectra. They are overlapped. Ellipsometric measurements at OCP show no significant change in the electrolyte content within the film over time (Fig. 48).

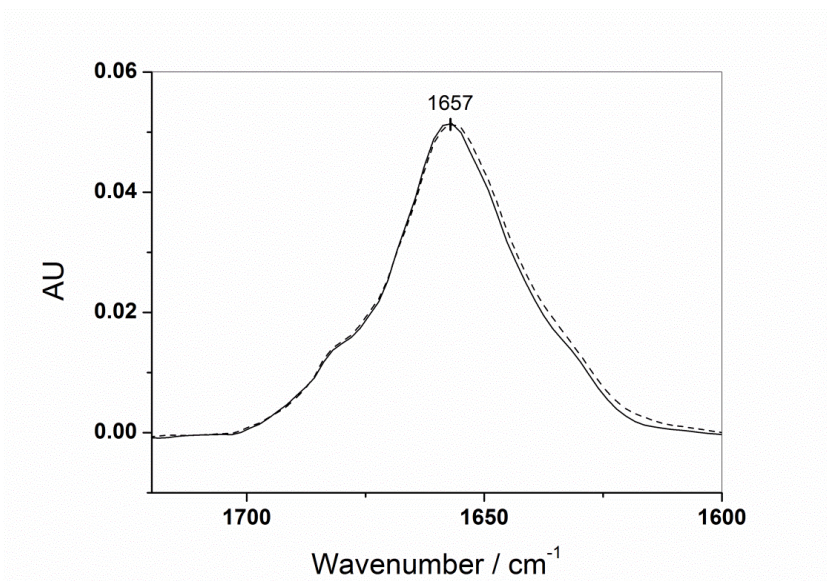


**Figure 47:** Amide I band of a collagen film on gold before (solid line) and after (dashed line) storage in electrolyte solution (NaF/D<sub>2</sub>O) for ca. 300 min. The molecules were adsorbed on the gold surface for 10 min from a solution with a concentration of 0.1 mg/ml.

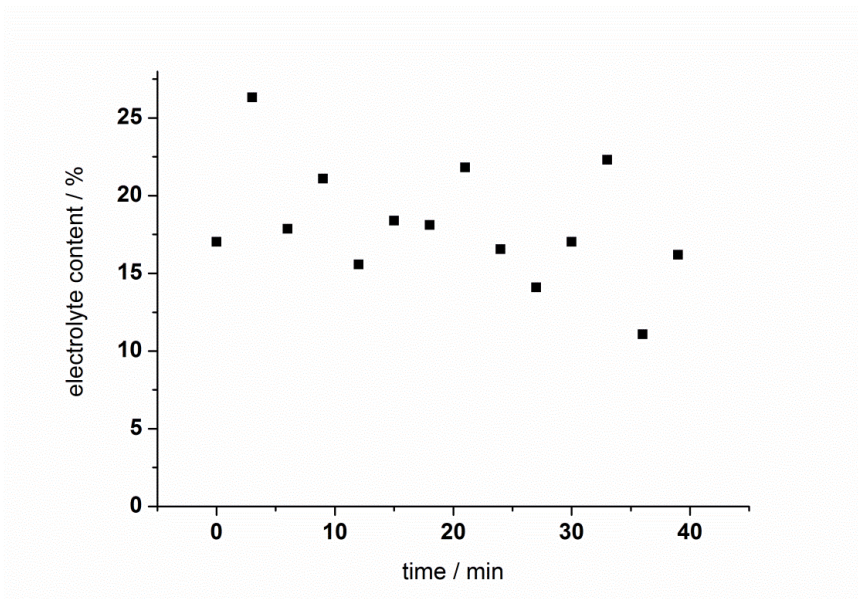


**Figure 48:** Stability of the electrolyte content within a collagen film at OCP over time. The molecules were adsorbed on gold for 10 min from a solution with a concentration of 0.1 mg/ml.

#### 4.2.4 Stability of the Collagen Film on Gold in the Electric Field

PM-IRRA spectra of a collagen film on gold in contact with the electrolyte solution were recorded in dependence of the applied potential. Figure 49 shows a stacked plot of amide I bands recorded using the potential program depicted in Figure 29. A potential range from  $E = 0.4$  V to  $E = -0.8$  V (vs. Ag|AgCl|3M KCl) was covered. Interestingly, all spectra are overlapped (Fig. 49, inset). This indicates that no desorption of collagen molecules and no structural changes in the protein molecule or changes in its hydration occur. The collagen molecules and the formed collagen film appear very stable in contact with the electrolyte solution and under the influence of applied potentials.

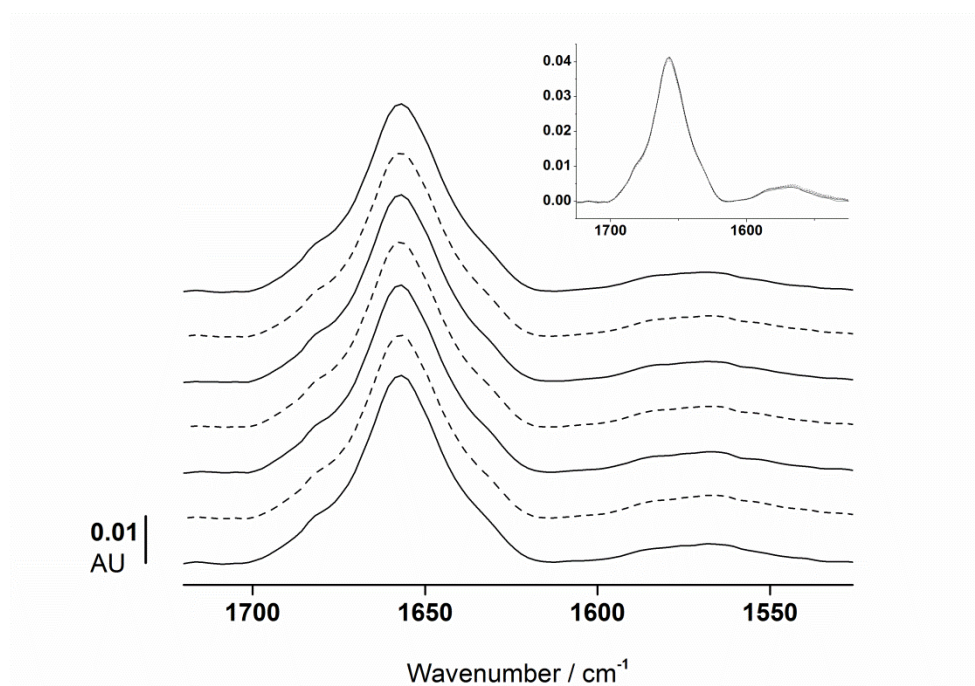


**Figure 49:** Amide I band of a collagen covered gold electrode at 0.4 V (solid) and -0.8 V (dashed). The time between the recording of the spectra was 20 min. The inset shows an overlap of all spectra. The molecules were adsorbed on gold for 10 min from a solution with a concentration of 0.1 mg/ml.

However, capacitance measurements of the collagen-covered gold electrode indicate a potential-dependent change in the protein film. The capacitance of the gold electrode was measured before modification, directly after adsorption of a collagen film and after applying the potential program (Fig. 50). The protein

adsorption is accompanied by a capacitance drop to ca.  $20 \mu\text{F}/\text{cm}^2$  (dashed line). Negative and positive potential steps lead to a change of the capacitance curve of the collagen-covered gold sample to resemble more an unmodified gold electrode (dotted line). This means, that the electrolyte solution comes to some extent in direct contact with the gold surface. Because no changes of the collagen film thickness and structure during this process are observed, these results also support the model of a porous an inhomogeneous film that, like a sponge, incorporates the electrolyte.

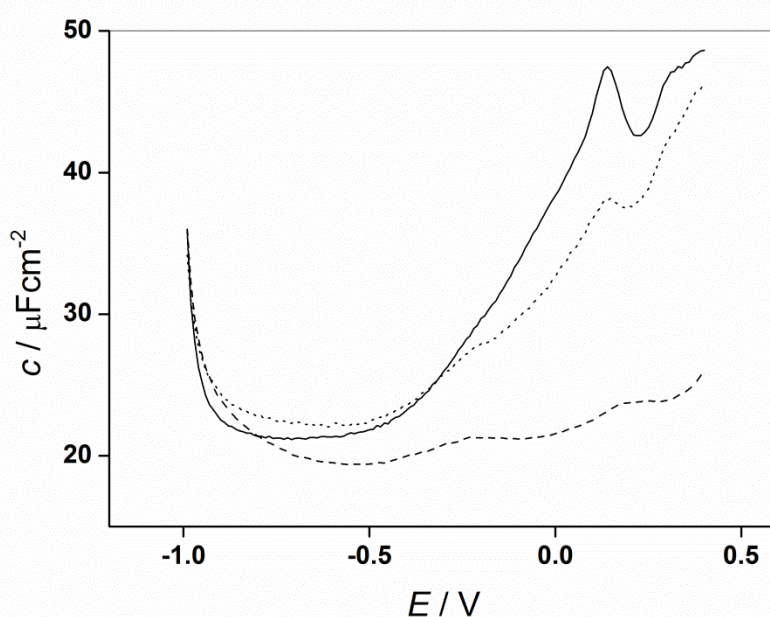


**Figure 50:** Capacitance curves of an unmodified gold electrode (solid) in comparison to a collagen covered one before (dashed) and after (dotted) applying the potential program. The molecules were adsorbed on gold for 10 min from a solution with a concentration of 0.1 mg/ml.

Ellipsometry measurements provide the electrolyte content in the collagen film in contact with the electrolyte at various potentials. Figure 51 shows two exemplary data sets. In one case the experiment started at the OCP ( $E = 0.2 \text{ V}$ ) and the potential was switched to  $E = 0.4 \text{ V}$  (solid line) and in the other case the potential step was from  $E = 0.4 \text{ V}$  to  $E = -0.9 \text{ V}$  (dashed line). The collagen electrolyte ratio at  $E = 0.4 \text{ V}$  does not coincide for both samples, due to the collagen film inhomogeneity. A response of the protein-electrolyte ratio to the potential step is observed within seconds. For potentials higher than the OCP, the electrolyte content in the film decreases. It increases at lower potentials. The electrolyte content stays constant as long as a constant potential is applied. This

effect is reproducible. Figure 52 shows the results of an experiment where the potential was switched several times between  $E = 0.4$  V and  $E = -0.9$  V. Every time the potential is changed the electrolyte content in the film changes as well. There appears to be some degradation of the film induced by the potential changes, because this behaviour is not completely reversible. This corresponds well with results of the capacitance measurements that showed an increased capacitance of a collagen covered gold electrode after experiments with changing potentials. The potential-dependent change of the incorporated electrolyte solution in the collagen film has, to the author's knowledge, never been observed before.

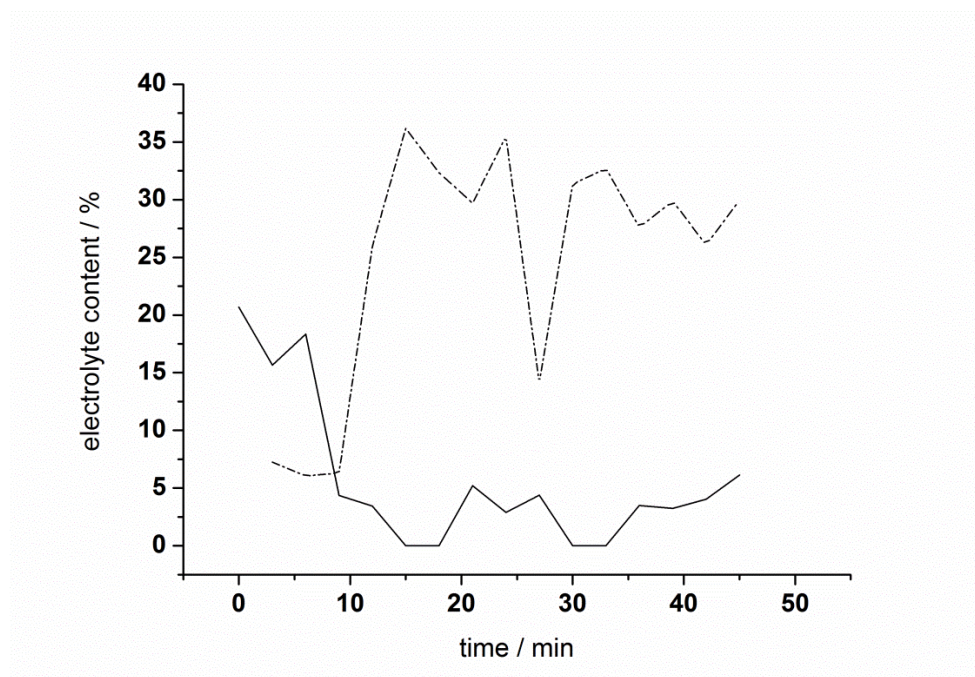


**Figure 51:** Collagen film response to applied potential. The solid line shows the step from the OCP to a potential of 400 mV vs Ag|AgCl|3M KCl at  $t = 8$  min. The dashed line corresponds to the step from 400 mV to -900 mV  $t = 10$  min. The molecules were adsorbed on gold for 10 min from a solution with a concentration of 0.1 mg/ml.

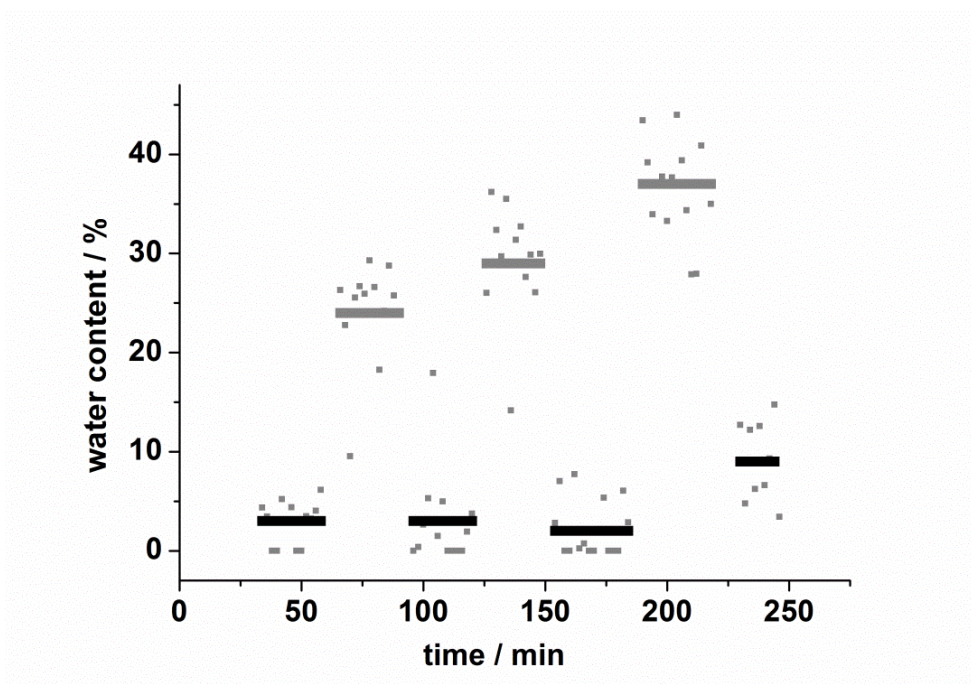


**Figure 52:** Ellipsometric results showing the content of electrolyte solution in the collagen film for one sample during several consecutive potential steps between 0.4 V and -0.9 V. Grey bars show the average electrolyte solution content during one step at 0.4 V, black bars the average electrolyte solution content during one step at -0.9 V. The single data points are also plotted. The molecules were adsorbed on gold for 10 min from a solution with a concentration of 0.1 mg/ml.

Furthermore, investigations of the dependence of the electrolyte content in the collagen film on the applied potential were carried out. A triangular potential wave (Fig. 53, dashed line) was applied to the collagen covered gold electrode. The upper and lower limits of the potential range were the same as for the experiments before (0.4 V to -0.9 V). The ellipsometry spectra documenting the film response were recorded and processed with the mixed interface layer model (Fig. 46f) to obtain the relative collagen content in the interface layer (Fig. 53, solid line). This plot shows clearly that the electrolyte content in the collagen film increases if more negative potentials are applied. Application of potentials higher than OCP leads to a decrease of the electrolyte content in the film.

In conclusion, it was shown that a collagen film adsorbed on gold exhibits a surprisingly dynamic behaviour under the influence of an applied potential. The electrolyte content in the interfacial protein film changes with the change in the applied potential. However, at a constant potential (in the range -0.9 V – 0.4 V) no changes occurred over time.

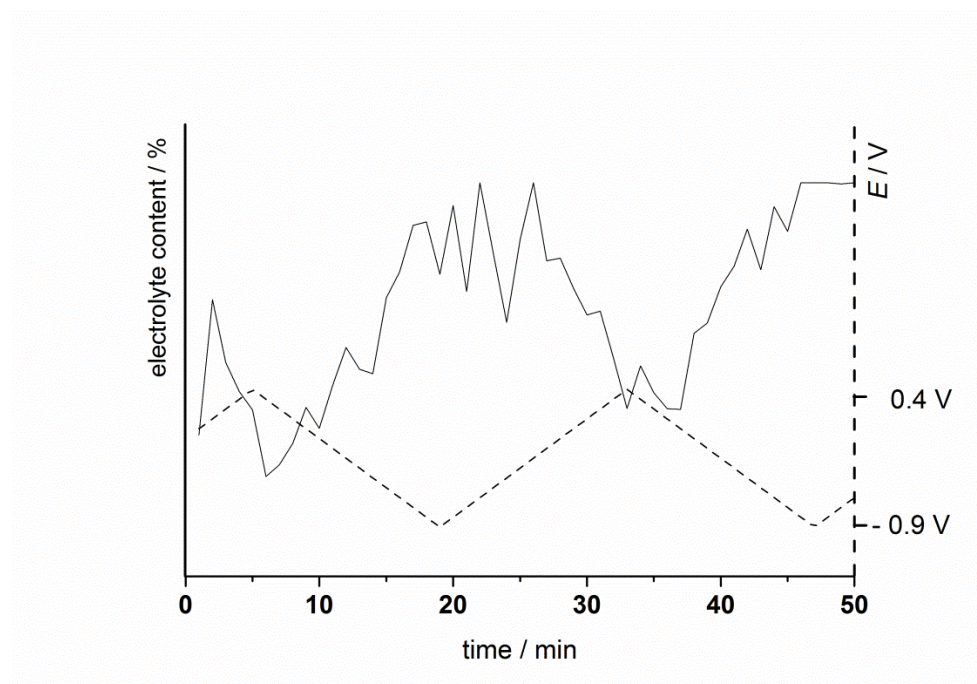


**Figure 53:** Dependence of collagen ratio (solid) on the applied potential (dashed). A triangular potential was applied to a collagen-covered gold surface with a scan rate of 1.5 mV/s. The molecules were adsorbed on gold for 10 min from a solution with a concentration of 0.1 mg/ml.

#### 4.2.5 Model for the Behaviour of a Collagen Film on Gold under the Influence of an Electric Field

The experimental results allow to present the following model of a collagen film adsorbed on a gold surface (Fig. 54). This model consists of a strongly adsorbed collagen film that is stable, but porous and inhomogeneous in a dry environment. Upon contact, the electrolyte is incorporated into the film. The film stability is not changed and neither desorption nor structural changes in the collagen molecules occur after hours of immersion into the electrolyte solution. A dynamic behaviour is observed only under the influence of a changing potential. If a potential is applied to the system that is higher than the OCP (0.2 V vs. Ag|AgCl|3M KCl. This potential is chosen as the reference point, because it describes a system without an applied bias.), the electrolyte content in the film decreases. The electrolyte content increases for potentials lower than OCP. At a constant potential the system reaches an equilibrium and no further changes occur. Removal of the collagen-covered gold electrode from the electrolyte and drying resulted in the reconstitution of the original dry state.

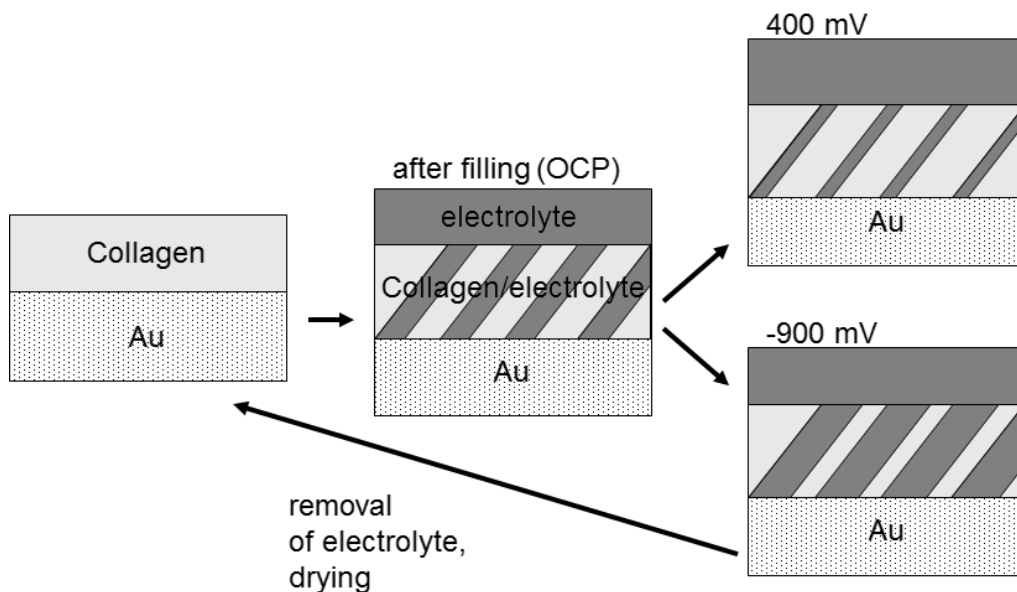


**Figure 54:** Model of a non-desorbing collagen film on gold. The electrolyte content within the film may change depending on the applied potential.

#### 4.2.6 Thermal Stability of Collagen on Gold

All experiments described above were performed at room temperature. In order to study the structure and stability of a collagen film under conditions that resemble physiological systems more closely, experiments were carried out at the following temperatures: 37 °C, 43 °C and 50 °C. The amide I band of the IR spectrum was analysed. As mentioned before, changes in this band can be correlated to structural changes in the protein molecule.

Figure 55 shows the amide I bands of the PM-IRRA spectra at the different temperatures. The band positions do not shift significantly even at the highest temperatures. This is a surprise, because according to literature the disintegration of the triple helix accompanying the denaturation occurs at 43 °C and should lead to a redshift of at least  $20 \text{ cm}^{-1}$  [15]. A plausible explanation of this abnormal high thermal stability is due to the state of adsorbed collagen molecules. In solution single molecules can move freely and the denaturation of the collagen triple helix is not hindered. Adsorbed collagen on the other hand is immobilized on the solid surface and thus unable to unravel. The second observation is that the intensities of the amide I bands change significantly with temperature. However, there is no

correlation between the band intensity and the temperature of the system and this observation might be an artefact due to several potential errors limiting the sensitivity of the PM-IRRAS in the spectroelectrochemical cell. For once, the working distance between the prism and the gold surface is not completely reproducible and may vary by several  $\mu\text{m}$ . Additionally, thermal expansion may introduce an error. Another limiting factor is introduced by the data treatment.

The intensity of the amide I band was measured for a collagen film, which was kept at a certain temperature for a longer period of time. The integral intensity  $I_0$  of the amide I band of the first spectrum is used to normalize the amide I band intensity  $I$  of all following spectra. The  $I/I_0$  ratio at the four different temperatures is plotted in Figure 56. Although there is some fluctuation of the normalized intensities the values do not change much over time. This indicates that the film is

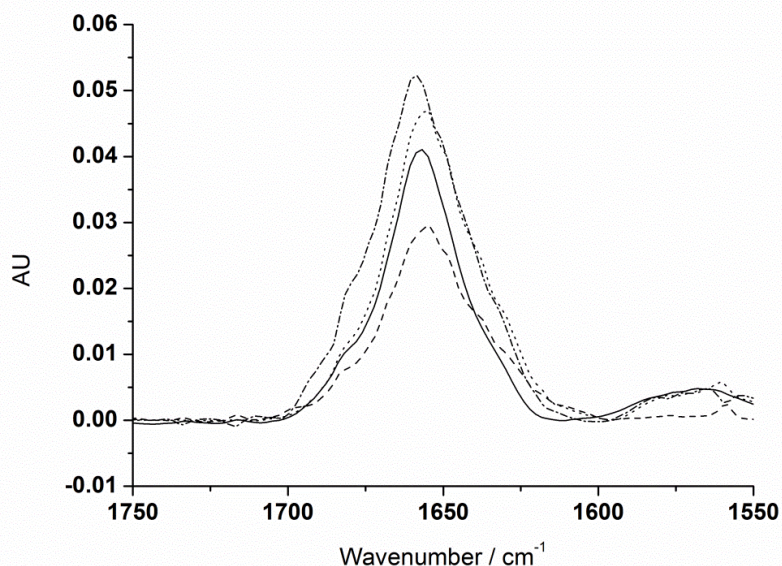


**Figure 55:** Amide I bands of four collagen films on gold in contact with the electrolyte solution at *rt* (solid), 38 °C (dashed), 43 °C (dot) and 50 °C (dash-dot). The molecules were adsorbed on gold for 10 min from a solution with a concentration of 0.1 mg/ml.

very stable and collagen molecules are unlikely to desorb from the gold surface independent of the given temperature. However, if a potential program (Fig. 29) is applied to the electrode, the normalized intensity decreases at higher temperatures (Fig. 57). This effect is strongest at 50 °C. Between 37 °C and *rt* there is no significant difference. Additionally, a changing potential is necessary to observe the intensity loss. If the electrode is kept at a constant potential, the amide I band intensity does not decrease (Fig. 58). The results strongly suggest a destabilization

of the protein film leading to the desorption of collagen molecules from the gold surface at 50 °C.

At room temperature the composition of the film, and probably its morphology, changes, due to incorporation of the electrolyte. But no desorption of collagen is observed. On the basis of these results the following, plausible, but not yet proven, hypothesis can be stated: The changes occurring in a collagen film under the influence of an alternating potential weaken the attractive interactions between the collagen molecules and the gold surface, thus enabling the proteins to desorb more easily at higher temperatures.

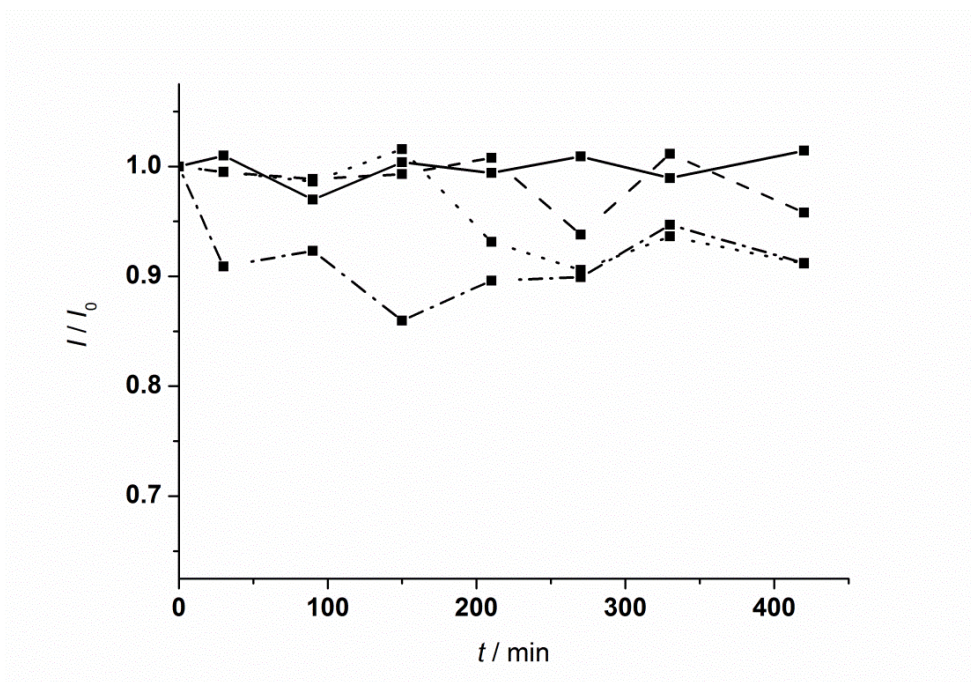


**Figure 56:** Amide I band intensity ratios of collagen on gold at OCP over time for different temperatures: rt (solid), 37 °C (dashed), 43 °C (dotted), 50 °C (dash-dot). The lines just act as a guide to the eye. The molecules were adsorbed on gold for 10 min from a solution with a concentration of 0.1 mg/ml.

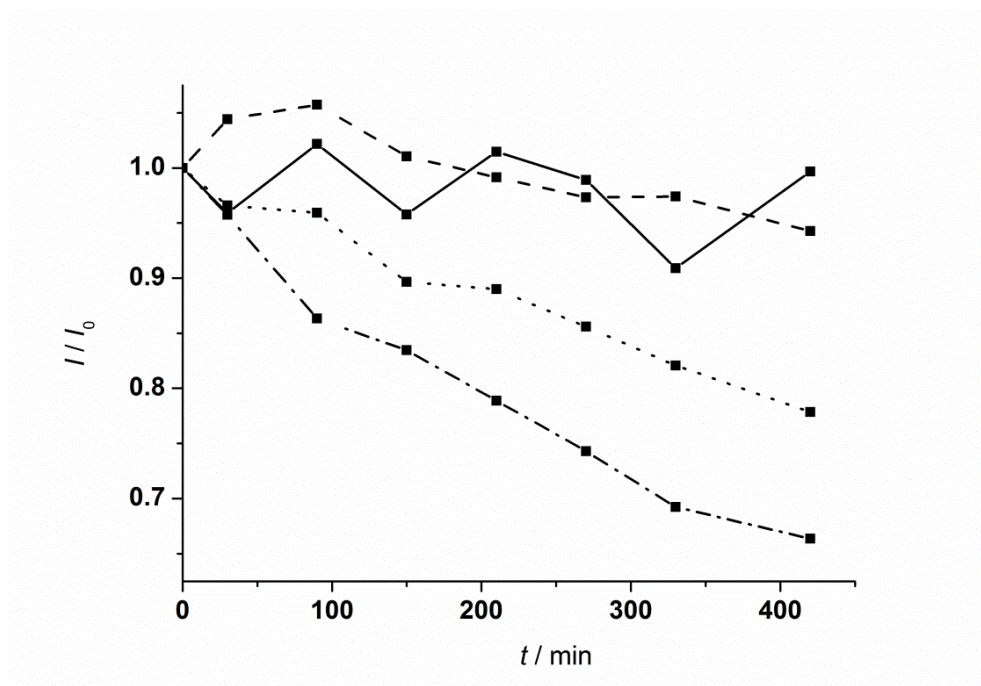


**Figure 57:** Amide I band intensity ratios of collagen on gold with stepwise changing potentials from -0.9 V to 0.4 V over time and for different temperatures: rt (solid), 37 °C (dashed), 43 °C (dotted), 50 °C (dash-dot). The lines just act as a guide to the eye. The molecules were adsorbed on gold for 10 min from a solution with a concentration of 0.1 mg/ml.

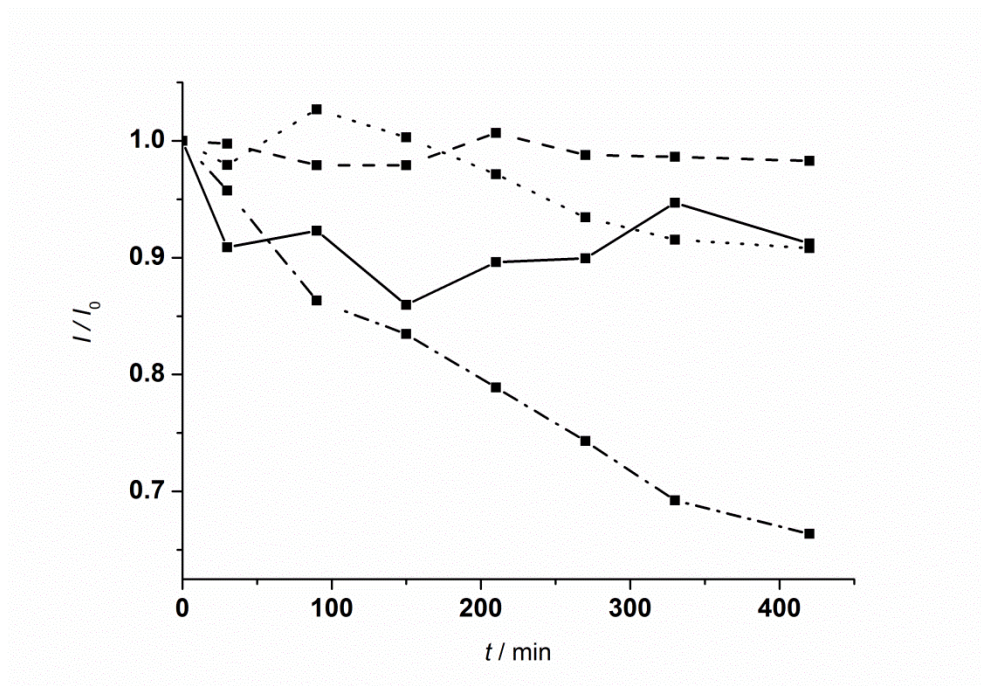


**Figure 58:** Amide I band intensity ratios of collagen on gold at 50 °C for OCP (solid), 0.4 V (dashed), -0.9 V (dotted), potential steps between 0.4 V and -0.9 V (dash-dot) over time. The lines just act as a guide to the eye. The molecules were adsorbed on gold for 10 min from a solution with a concentration of 0.1 mg/ml.

### 4.3 Studies on Collagen/Lipid Bilayer Films on the Gold Electrode Surface

After the successful composition and characterization of a model system for a protein film on a biomaterial surface (Fig. 59a), the next task was to find a model system for the interaction of the protein film with a cell membrane, corresponding to the next step in the bio integration cascade (Fig. 1). Bilayers composed of phospholipids, like DMPC, are a simple and well characterized system, which mimic a cell membrane in its thickness, water permeability, bending rigidity, surface tension and viscosity <sup>[ 123, 124]</sup> (Fig. 59b). Although simple phospholipid bilayers lack the anchoring integrin proteins involved in the ligand receptor binding system of cell membranes to collagen <sup>[ 1]</sup>, they were chosen as a relatively simple starting point. Real systems are much more complex, including not only the integrin proteins but also cytoskeletal connections and intermediate proteins like vimentin <sup>[ 125]</sup>. Future research would involve the addition of more components to the bilayer to mimic a real cell membrane more closely. It was already shown that collagen interacts with lipid monolayers <sup>[ 126]</sup> and bilayers <sup>[ 127]</sup>, stabilizing them in the process, and facilitates the adhesion of cells <sup>[ 128]</sup>. Preliminary results are described in this chapter.

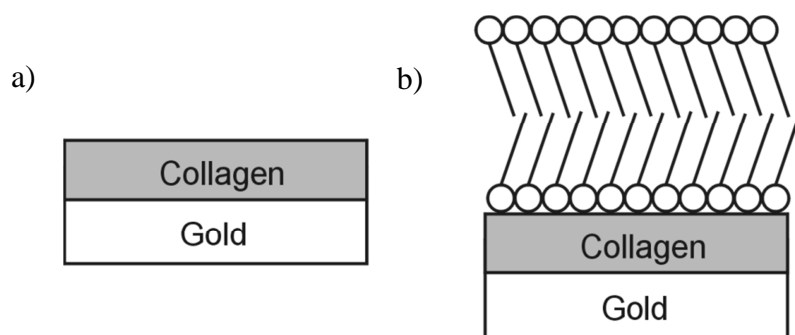


**Figure 59:** a) model system consisting of a gold substrate layer with an adsorbed collagen film. b) expanded model system with a phospholipid bilayer transferred to the collagen film.

### 4.3.1 Formation of the DMPC Monolayer on the Water Surface

A Langmuir isotherm (Fig. 60) was recorded to determine the surface pressure for the transfer of a DMPC layer onto a gold substrate. This is the 2D equivalent to a  $pV$ -diagram in the 3D system. At high areas per molecule ( $>0.9 \text{ nm}^2$ ) there is almost no interaction between the DMPC phospholipid molecules on the water surface and the measured surface pressure  $\pi$  is close to zero. This situation is comparable to a two dimensional gas phase. With decreasing area available per single molecule ( $<0.9 \text{ nm}^2$ ) the surface pressure starts to increase due to intermolecular interactions. The DMPC molecules begin to order themselves with their polar head groups towards the water surface. This is called a 2D fluid-like phase. A further decrease in the area per molecule leads to a phase transition ( $\sim 0.45 \text{ nm}^2$ ). The DMPC molecules are highly ordered and form a 2D solid-like phase. To obtain a stable and ordered solid-like layer the transfer was done at a surface pressure  $\pi = 42 \text{ mN/m}$ .

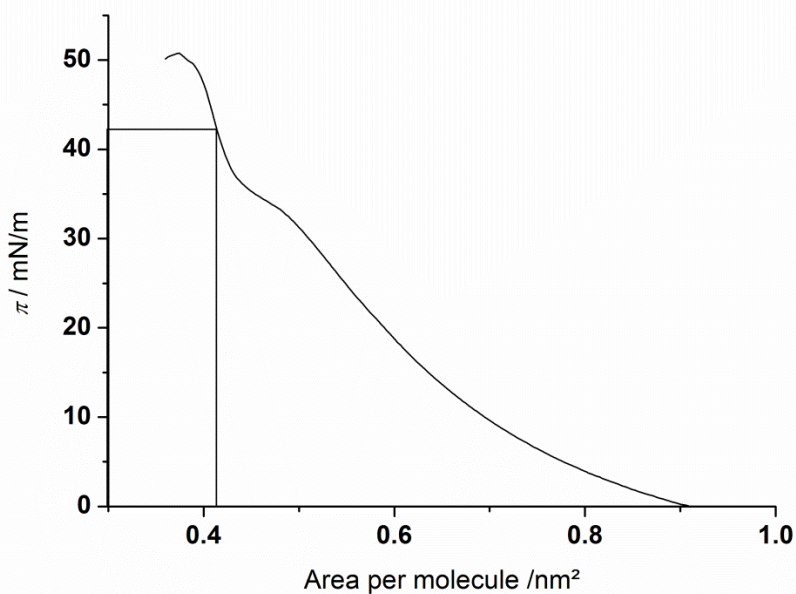


**Figure 60:** Surface pressure vs. area per molecule compression isotherm of DMPC on an aqueous subphase.

### 4.3.2 PM-IRRA Spectra of a DMPC Bilayer on a Gold Surface

After the transfer of the DMPC bilayer to the gold surface PM-IRRA spectra were recorded in air. The CH-stretching modes in the acyl chains (Fig. 61) and the CO-stretching mode of the polar head group (Fig. 63) are of analytical interest. The CO-stretching vibration is found at  $1738\text{ cm}^{-1}$ . In the same spectral region the  $\text{CH}_2$ -scissoring mode in the acyl chain of DMPC is found at  $1468\text{ cm}^{-1}$ . Four different CH-stretching modes can be distinguished (Fig. 61). They can be attributed to the asymmetric  $\text{CH}_3$ -stretching vibration at  $2964\text{ cm}^{-1}$  the asymmetric  $\text{CH}_2$ -stretching vibration at  $2922\text{ cm}^{-1}$  as well as the symmetric  $\text{CH}_3$ - and  $\text{CH}_2$ -stretching vibrations at  $2876\text{ cm}^{-1}$  and  $2853\text{ cm}^{-1}$ . Additionally, the asymmetric  $\text{CH}_2$ -stretching mode has a shoulder at  $2935\text{ cm}^{-1}$  due to the Fermi resonance (FR) between the symmetric  $\text{CH}_3$ -stretching and the asymmetric  $\text{CH}_3$ -bending mode [129]. These bands would be overlapped with the CH-stretching modes on the collagen film (Fig. 35). In order to distinguish between the CH-stretching modes in the protein film and the lipid bilayer, the per-deuterated phospholipid d54-DMPC was used. The CD-stretching modes are shifted by roughly  $-850\text{ cm}^{-1}$  (Fig. 62) compared to the CH-stretching modes, leading to asymmetric  $\text{CD}_3$ - and  $\text{CD}_2$ -stretching modes at  $2219\text{ cm}^{-1}$  and  $2197\text{ cm}^{-1}$ . The symmetric  $\text{CD}_2$ - and  $\text{CD}_3$ -stretching modes are located at  $2093\text{ cm}^{-1}$  and  $2073\text{ cm}^{-1}$  [130, 131].

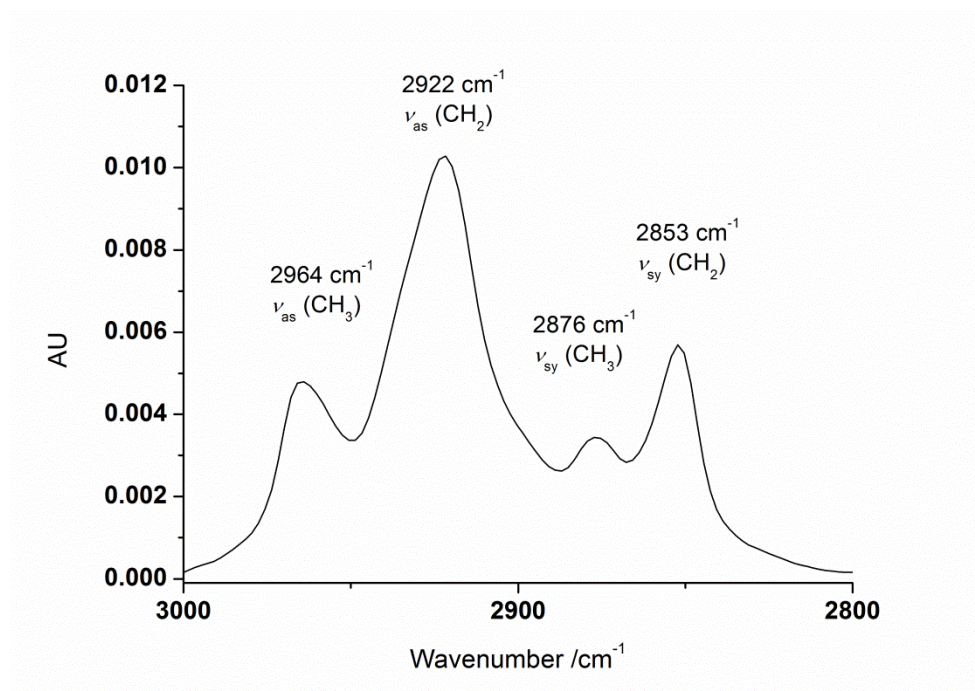


**Figure 61:** PM-IRRA spectra of the CH-stretching modes of a DMPC bilayer on gold transferred at  $\pi = 42$  mN/m.

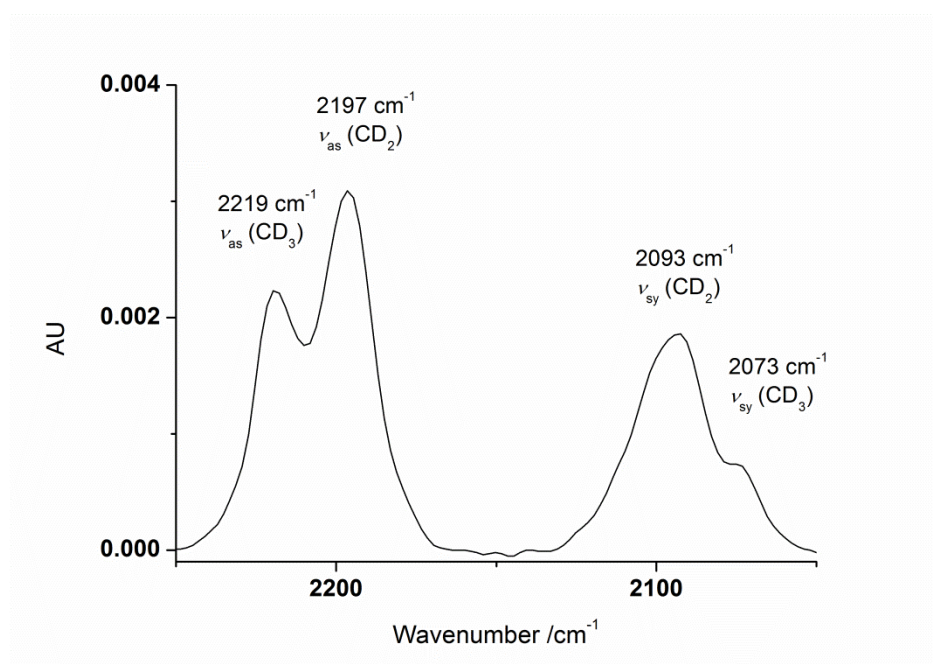


**Figure 62:** CD-stretching modes of a d54-DMPC bilayer on gold. Transferred at  $\pi = 42$  mN/m.

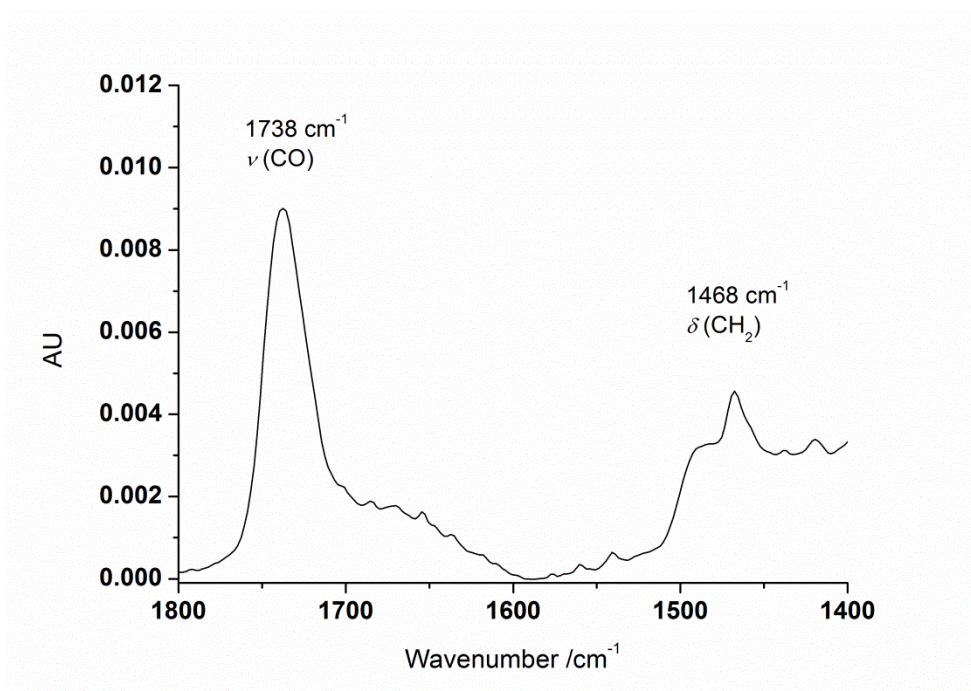


**Figure 63:** CO-stretching and CH<sub>2</sub>-scissoring modes of a DMPC bilayer on gold. Transferred at  $\pi = 42$  mN/m.

### 4.3.3 PM-IRRA Spectra of DMPC-Collagen Films on Gold in Air

The PM IRRA spectra of the DMPC and the d54-DMPC bilayers on collagen-covered gold surfaces in contact with air were measured in the CH-stretching region, the CD-stretching region and the amide I band region (Fig. 64-66). The first and most significant difference in the CH-stretching region (Fig. 64) is the very high intensity of the CH-stretching modes of the DMPC bilayer on collagen (dotted line) in comparison to the collagen CH-stretching signal (solid line). This can be explained by two factors. The collagen layers have been shown to be inhomogeneous and porous instead of being ordered and densely packed like in the case of DMPC. On the other hand DMPC has a much higher number of CH<sub>2</sub>- and CH<sub>3</sub>-groups in relation to the size of the molecule compared to collagen molecules. Both factors result in a comparatively higher density of CH<sub>2</sub>- and CH<sub>3</sub>-groups on the DMPC-covered surface. Furthermore, the CH-stretching signal of the DMPC bilayer on collagen does neither show any significant decrease in the signal intensity nor peak shifts, when compared to the DMPC bilayer transferred

directly on the gold surface (Fig. 61). This indicates, that the collagen adsorbed on the gold surface does not interfere with the DMPC transfer procedure. For the d54-DMPC bilayer on collagen (dashed line) no IR activity was observed in this region, because the CD-stretching modes are shifted to lower wavenumbers.

In the CD-stretching region (Fig. 65) only the d54-DMPC bilayer on collagen (dashed line) has IR absorption bands. Again the signal intensity and peak positions do not change in comparison to a bilayer of d54-DMPC transferred directly on the gold surface (Fig. 62). The adsorbed collagen film has no influence on the DMPC transfer. For the collagen-covered sample (solid line) and the DMPC bilayer on a collagen-covered sample only slight differences are observed, due to the limitations of background correction.

In the PM-IRRA spectra of the amide I region (Fig. 66) all three samples are dominated by the amide I, the amide II and the CH<sub>2</sub>-scissoring bands of the collagen. However, for the DMPC bilayer on collagen (dotted line) and the d54-DMPC bilayer on collagen (dashed line) the additional CO-stretching mode of the polar phospholipid head group at 1738 cm<sup>-1</sup> is clearly visible and blue-shifted by 66 cm<sup>-1</sup> in comparison to the amide I band (Fig. 36). Although both signals overlap slightly, they can be clearly distinguished and are suitable for analytical purposes. The signals of both samples have the same position and intensity, proving that the isotope exchange in the acyl chain has no influence on the CO double bonds in the polar head group.

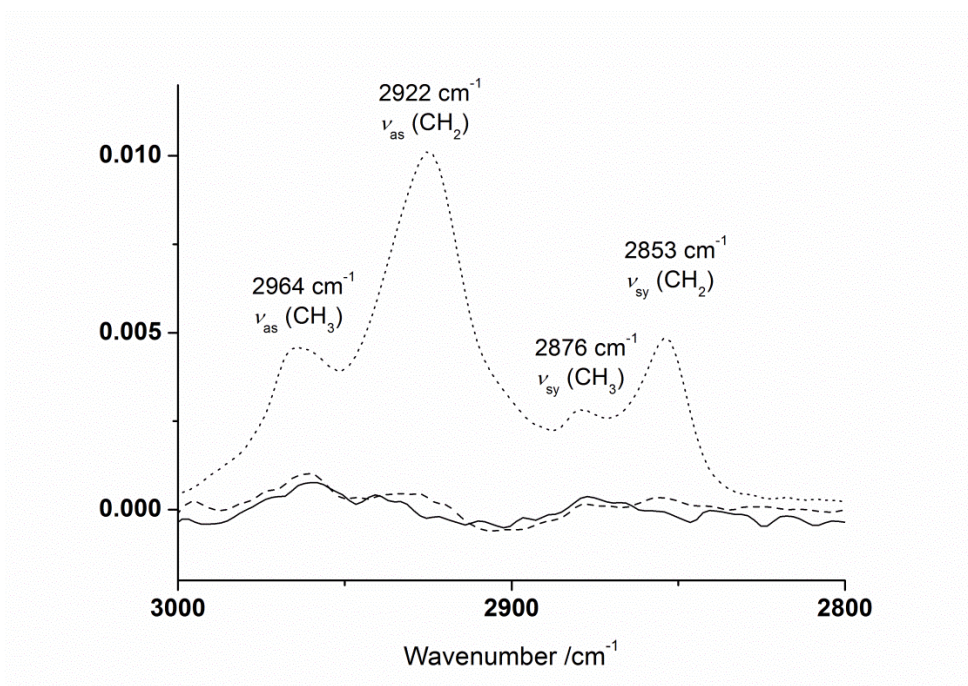


**Figure 64:** Comparison of the CH-stretching region for a collagen covered gold surface (solid line), a gold surface with a d54-DMPC bilayer on the collagen film (dashed line), and one with a DMPC bilayer on the collagen film (dotted line).

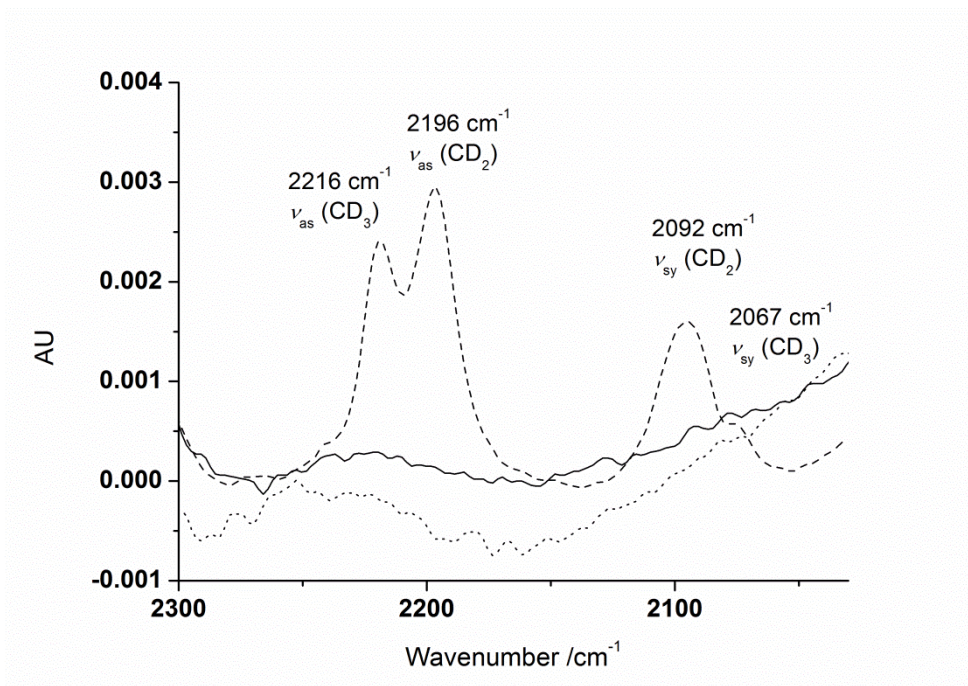


**Figure 65:** Comparison of the CD-stretching region for a collagen covered gold surface (solid line), a gold surface with a d54-DMPC bilayer on the collagen film (dashed line), and one with a DMPC bilayer on the collagen film (dotted line).

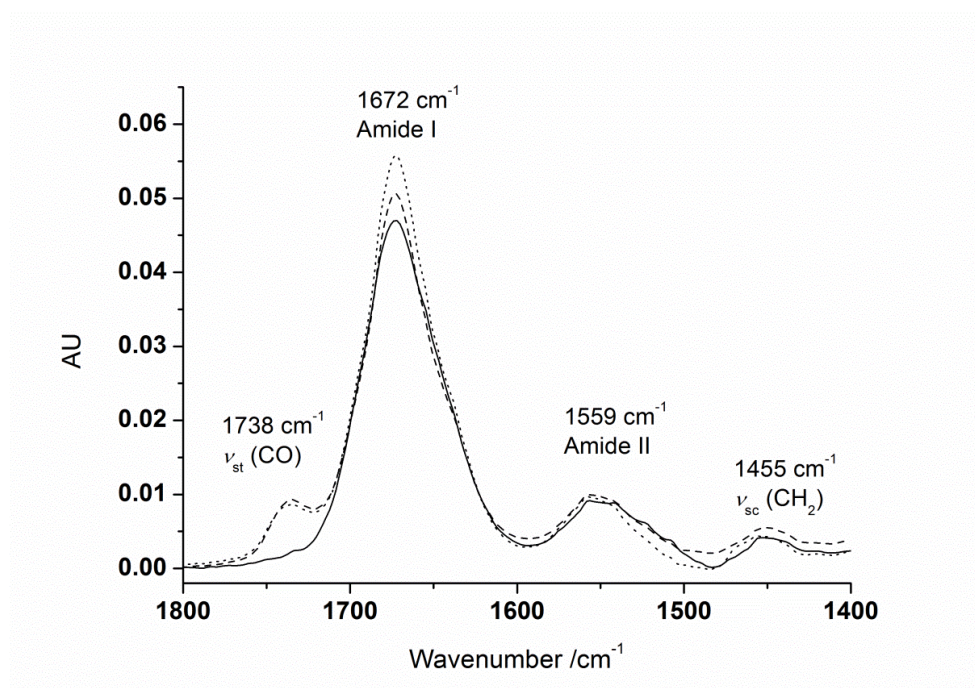


**Figure 66:** PM-IRRA spectra in the 1800-1400  $\text{cm}^{-1}$  region for a collagen-covered gold surface (solid line), a gold surface with a d54-DMPC bilayer on the collagen film (dashed line), and one with a DMPC bilayer on the collagen film (dotted line).

#### 4.3.4 PM IRRA Spectra of a DMPC-Collagen Film on Gold in Contact with Electrolyte

The PM-IRRA spectra of the d54-DMPC bilayer on the collagen-covered gold substrate were recorded in contact with the electrolyte solution. Figure 67 shows the CD-stretching region of the d54-DMPC bilayer on gold (solid line) and of the d54-DMPC bilayer on collagen-covered gold (dashed line). For this experiment  $\text{H}_2\text{O}$  instead of  $\text{D}_2\text{O}$  was used as solvent for the electrolyte, because the OD-vibrations would overlay the CD-stretching modes. The peak positions for both samples do not differ significantly. However, the intensity of the CD-signal was decreased for the d54-DMPC bilayer on collagen-covered gold. The most likely explanation for this is a partial removal of the d54-DMPC bilayer upon immersion in the electrolyte. As proof for this hypothesis PM-IRRA spectra of a d54-DMPC bilayer on a collagen-covered gold sample were recorded in air (Fig. 68) before immersion into the electrolyte (solid line) and after retraction from the electrolyte solution and drying (dashed line). The amide I/II and CH-scissoring band intensities of the protein do not decrease. But CD- and CO-stretching modes

of the d54-DMPC almost vanish after contact with the electrolyte. This points to a removal of the phospholipid bilayer. The destabilization of the bilayer on collagen could be explained by less attractive forces between the polar head groups of the DMPC and the largely unpolar protein compared to the gold surface.

Considering the presented results, it has to be admitted, that the chosen DMPC bilayer is not very well suited as a model system. The films are not sufficiently stable for measurements in contact with electrolyte and especially to model the strong adhesion of cells to biomaterial surfaces. However, it was also shown that the PM-IRRAS is suitable to obtain information about the bilayer and the underlying protein. One possible solution to the issue of bilayer stability and adhesion could be the introduction of additional lipids, e.g. cholesterol, which has been shown to stabilize lipid bilayers [132, 133, 134].

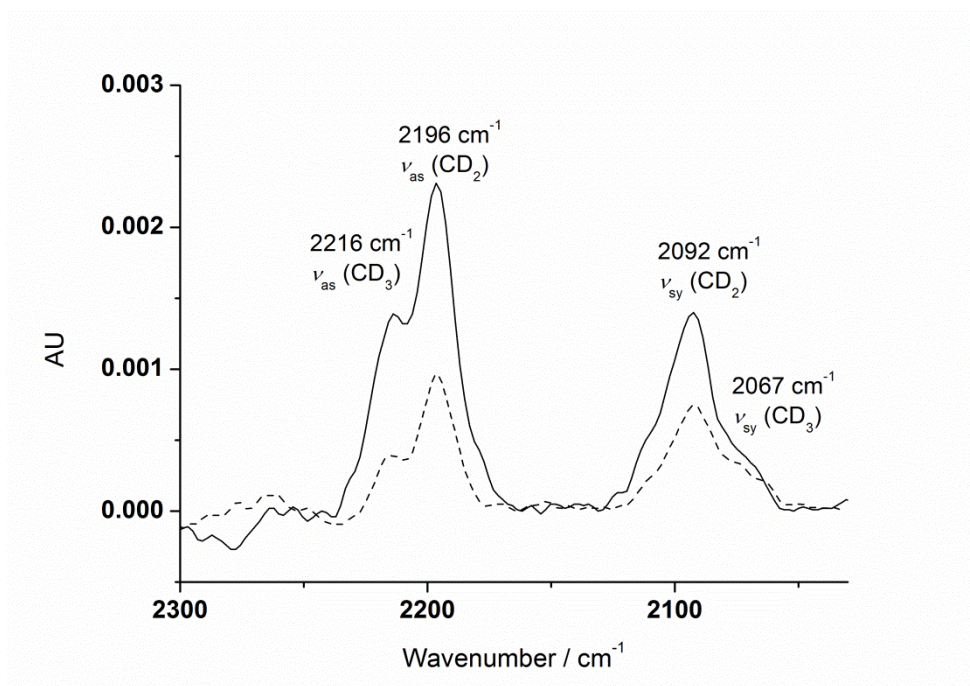


**Figure 67:** CD-stretching modes of a d54-DMPC bilayer on gold in contact with H<sub>2</sub>O/NaF<sub>2</sub> electrolyte (solid line) and of a d54-DMPC bilayer on collagen on gold (dashed line).

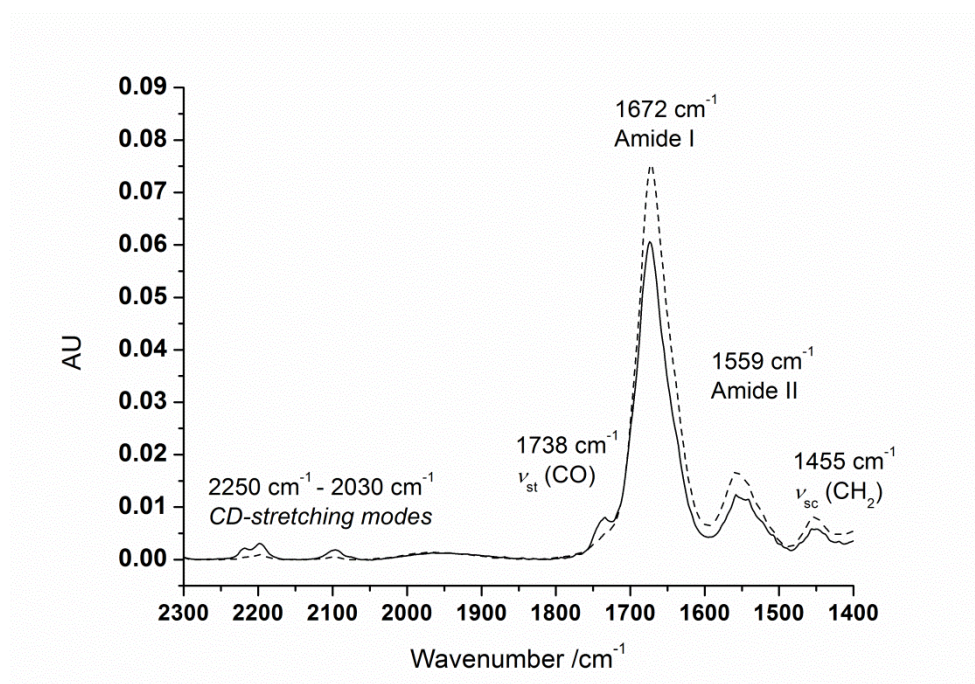


**Figure 68:** Comparison of CD-stretching modes and amide I spectral region of a d54-DMPC bilayer on a collagen film on gold before immersion in electrolyte (solid line) and after retraction from the electrolyte solution and drying of the sample (dashed line).

#### 4.4 $\text{TiO}_2$ and $\text{TiO}_x\text{C}_y$ as a Substitute for the Au Substrate

Gold is not a very common biomaterial and for implants titanium and its alloys are usually used. PM-IRRAS measurements have shown that collagen forms stable films on titanium surfaces, comparable to those on gold (Fig. 69)<sup>[14]</sup>.

However, titanium is not suitable for electrochemical experiments due to the formation of an insulating oxide layer. Capacitance curves (Fig. 70) have shown no significant difference between an unmodified titanium oxide surface and the same surface after adsorption of collagen and transfer of a DMPC bilayer. Additionally, a cyclic voltammogram in a 1 mM ferrocene methanol (FcMeOH) solution in 0.1 M NaF showed no electron transfer reaction (Fig. 70, inset).

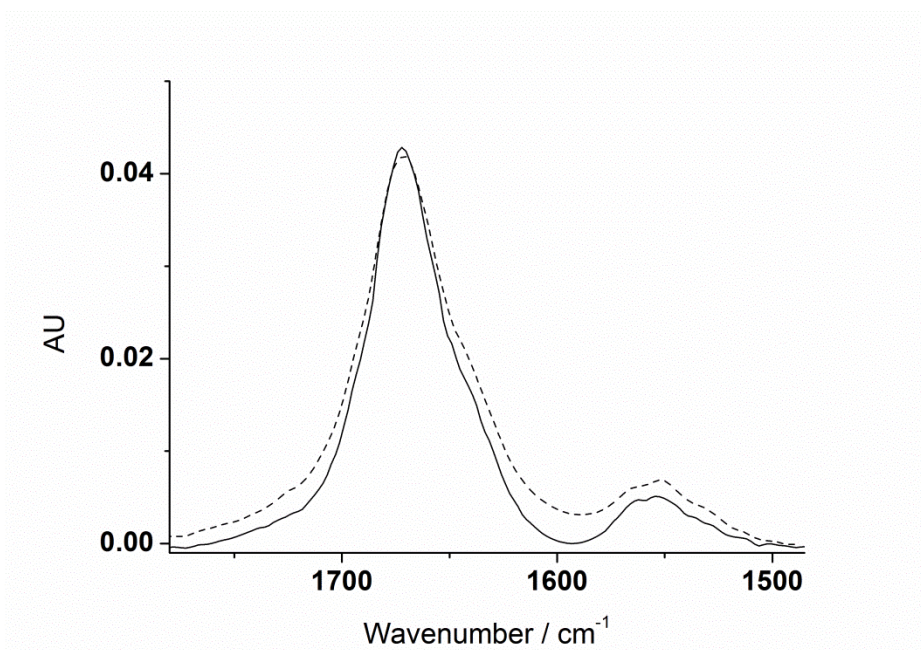


**Figure 69:** Amide I and amide II band of a collagen film on titanium (solid) and of a collagen film on gold (dashed). The molecules were adsorbed for 10 min from a solution with a concentration of 0.1 mg/ml.

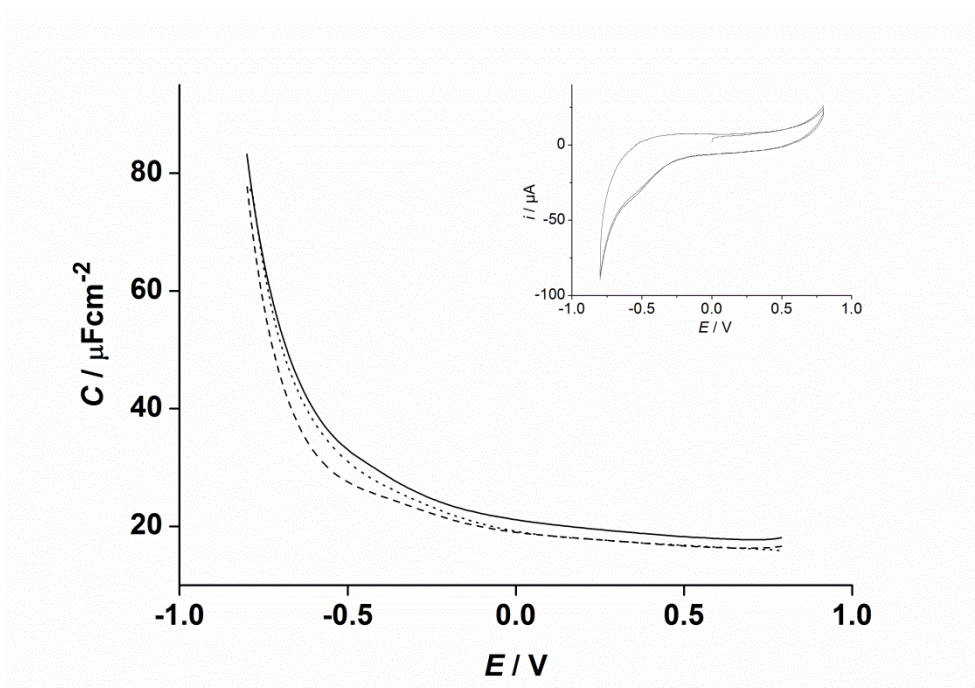


**Figure 70:** Capacitance curves of an unmodified TiO<sub>2</sub> electrode (solid), a collagen-covered TiO<sub>2</sub> electrode (dashed) and a collagen covered TiO<sub>2</sub> electrode with a DMPC bilayer (dotted). The inset shows the CV of a titanium electrode in contact with a 1 mM FcMeOH solution in 0.1 M NaF.

Conductive TiO<sub>x</sub>C<sub>y</sub> surfaces <sup>[107]</sup> were tested as a substitute for TiO<sub>2</sub>. PM-IRRA spectra were recorded in the amide I region from 1400 cm<sup>-1</sup> to 1800 cm<sup>-1</sup>

after the adsorption of collagen (Fig. 71). The integral amide I band intensity decreases by a factor of 10 compared to a collagen-covered gold surface. This is mainly due to two factors: the weak reflectivity of IR light at the  $\text{TiO}_x\text{C}_y$  surface and the scattering effect of the relatively rough surface. Also there might be less collagen adsorbed in the  $\text{TiO}_x\text{C}_y$  surface but this cannot be deduced from the spectra. However, the positions of amide I/II bands at  $1669\text{ cm}^{-1}$  and  $1548\text{ cm}^{-1}$  and their outlines are comparable to a collagen-covered gold surface. The  $\text{TiO}_x\text{C}_y$  surfaces were not suitable for measurements in the spectroelectrochemical cell due to the electrochemical instability of the surfaces. 100 CV's were recorded consecutively of a  $\text{TiO}_x\text{C}_y$  surface in 0.1 M NaF electrolyte solution (Fig. 72). An irreversible oxidation occurs that leads to the passivation of the surface. Due to that fact, it is not possible to perform reproducible electrochemical measurements with freshly prepared  $\text{TiO}_x\text{C}_y$  samples. Another problem originates in the production process of the surfaces. Two surfaces of the same batch have different properties depending on their position within the oven. Because of the irreproducibility of the electrochemical surface properties,  $\text{TiO}_x\text{C}_y$  cannot be used as a conductive model surface for  $\text{TiO}_2$ , yet. However, this material is still under development and may become of more analytical value in the future or even become a suitable biomaterial itself.

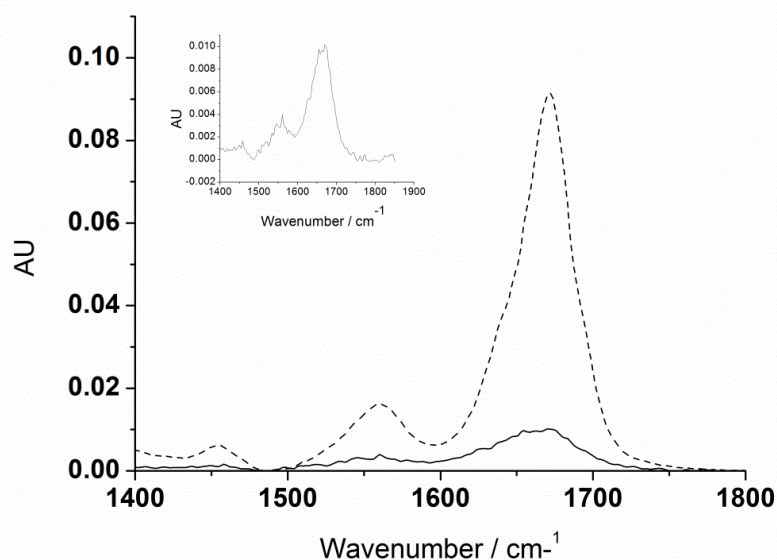


**Figure 71:** PM-IRRA spectra in the amide I region of a collagen covered  $\text{TiO}_x\text{C}_y$  surface (solid) and a collagen covered gold surface (dashed). The inset shows a magnification of the solid curve. The molecules were adsorbed on both materials for 10 min from a solution with a concentration of 0.1 mg/ml.

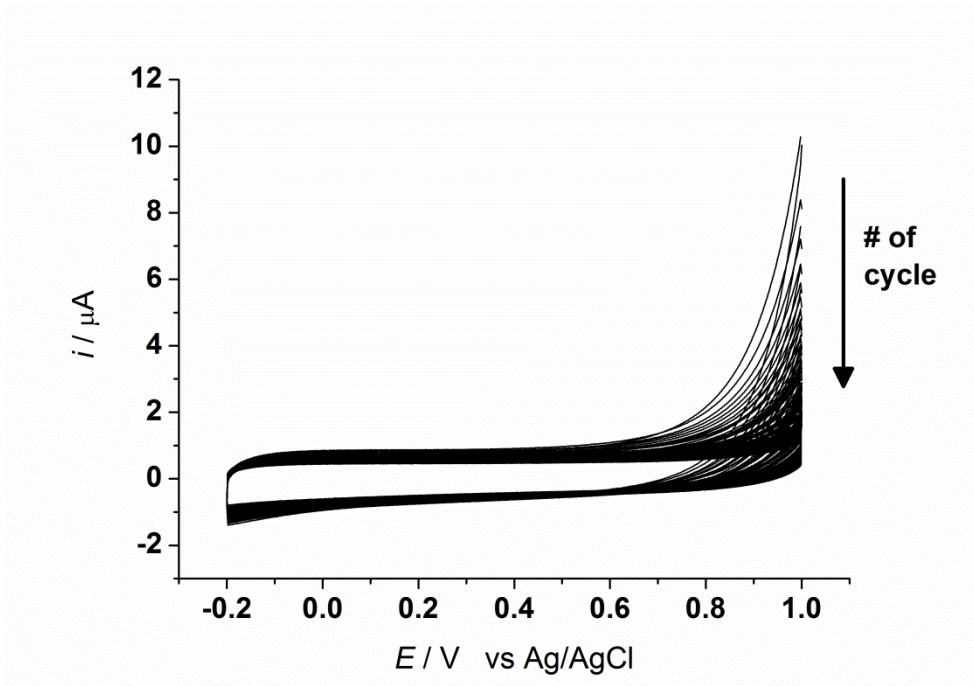


**Figure 72:** 100 consecutive CV's of a  $\text{TiO}_x\text{C}_y$  surface in 0.1 M NaF solution. The scan rate was 0.05 V/s.

## 5 Conclusion and Outlook

The aim of this thesis was the introduction and characterization of a biomimetic model system of a protein film on a biomaterial surface under the influence of electric fields. The chosen materials were collagen as the adsorbed protein and gold as the biomaterial surface. It was shown that stable and ca. 6 nm thick collagen films could be formed on the gold surface. The average thickness determined by ellipsometry varied between a mono- and a triple-layer on the same sample. This film inhomogeneity limits the reproducibility of the conducted experiments.

The application of devices that allowed the combination of different techniques like the spectroelectrochemical cell and its pendant for ellipsometry enabled the in situ monitoring of the collagen film in contact with the electrolyte.

The PM-IRRA spectra of a collagen film adsorbed on gold in contact with an electrolyte solution show a shift of the amide I/II bands compared to a dry film. This is explained by the change in the hydration of the collagen molecules and the formation of H-bonds. The capacitance of the collagen-covered gold surface is close to 20  $\mu\text{F}/\text{cm}^2$  and is significantly lower than the capacitance of a clean gold surface. However, a densely packed film of organic material would reduce the capacity even more, as it is the case for a lipid bilayer on gold (2-5  $\mu\text{F}/\text{cm}^2$ ). This means that the collagen film contains defects and irregularities. Accordingly, the optical model of the system was adjusted to allow the incorporation of the electrolyte solution into the film. It was also shown, that the electrolyte content within the film is dependent on the potential applied to the gold electrode. Potentials higher than the OCP (0.2 V vs. Ag|AgCl|3M KCl) cause a decrease in the electrolyte content while potentials more negative than OCP cause an increase. The observation of electrodynamic changes in the collagen film is important because very little work has been conducted in this field so far. To the author's knowledge this is the first study concerning the behaviour of adsorbed collagen films under the influence of an electric field. Nevertheless, under physiological conditions strong electric fields can be induced locally at cell membrane and protein film interfaces. To fully understand processes like the integration of a biomaterial in the human body the electrodynamics have to be taken into account.

To increase the similarity to physiological systems spectroelectrochemical experiments were conducted at 37 °C, corresponding to the body core temperature. Measurements were also carried out at 43 °C, the temperature at which collagen in solution starts to denaturize, and at 50 °C, corresponding to the complete disintegration of the protein tertiary structure. Surprisingly, adsorbed collagen molecules are stable over the whole temperature range. This shows that the molecules are stabilized by the immobilization process. The application of collagen precoatings for biomaterials would not be possible without this feature. Under the influence of changing potentials at the gold surface, desorption of the collagen is observed at high temperatures (>43 °C). Emphasis lies on the necessity of a changing potential. At constant potentials, no significant desorption is observed. This can be explained by a weakening of the interaction between the collagen molecules and the gold surface but further experiments are required. Especially the dependence on a changing potential needs to be investigated concerning for example the influences of the frequency of change and potential differences.

A further biomimetic modification used in this thesis was the transfer of a DMPC bilayer onto the protein film. This resembles the next step in the biointegration cascade, namely the adhesion of cells. PM-IRRAS experiments showed a promising depth of information because the IR bands of collagen and DMPC can be analyzed separately. In the case of the CH-stretching modes, perdeuterated d54-DMPC was used to distinguish the bands from the CH valence bands of collagen. However, the DMPC bilayer is very unstable on the collagen film when exposed to the electrolyte solution. Conclusive experiments were not possible due to disintegration of the bilayer. The formation of a stable bilayer is a challenge for future research and may be achieved by adding new components such as cholesterol to increase the stability of the lipid bilayer.

The model system based on the components collagen on gold can be further enhanced. Instead of collagen, a protein from the extracellular matrix, a protein of a different physiological environment like the serum proteins fibrinogen or albumin may be analyzed. Mixtures of proteins may also be employed because of the closer resemblance to physiological systems. Gold on the other hand could be replaced by titanium and its alloys with medical applications such as Ti6Al7Nb or Ti6Al4V or other metallic biomaterials like stainless steel or CoCr alloys.

However, these materials form a passivating oxide layer and do not serve well as an electrode. Doping of the oxide layer with carbon would increase the conductivity. However, so far the resulting  $\text{TiO}_x\text{C}_y$  films were unstable under physiological conditions. It is also uncertain if the physical and chemical properties of the material change too much for a close resemblance of the biomaterial. Insulating biomaterials like ceramics are not suitable for the experiments conducted in this thesis.

The used experimental techniques have proven to be very well suited for the analysis of the model system. Their extremely high sensitivity allows the investigation of thin films in the range of molecular monolayers. Especially with the help of PM-IRRAS it is possible to distinguish between different components simultaneously. However, the necessary high reflectivity and amplification of the electric field at the reflecting surface cannot be met by most biomaterials. It is still possible to employ those materials by depositing a very thin film with a thickness of a few nm on a gold substrate as was shown in the case of titanium on gold <sup>[14]</sup> and silica on gold <sup>[135]</sup>. The surface properties correspond to the biomaterial while the reflectivity is almost the same as for an unmodified gold surface.



## 6 Bibliography

1. Zhang, M. Biocompatibility of Materials. In *Biomaterials and Tissue Engineering*; Shi, D., Ed.; Springer Verlag: Heidelberg, 2004; pp 83-144.
2. Breme, H.; Biehl, V.; Helsen, J. Metals and Implants. In *Metals as Biomaterials*; Helsen, J., Breme, H., Eds.; Springer Verlag: Heidelberg, 1998; pp 37-72.
3. Roessler, S.; Scharnweber, D.; Worch, H. *J. Mater. Sci. Let.* **1999**, *18*, 577-579.
4. Kazim, M.; Katowitz, J.; Fallon, M.; Piest, K. *Ophthalm. Plast. Reconstr. Surg.* **1992**, *8*, 94-108.
5. He, H.; Li, G.; Li, B.; Chen, Z. *Appl. Surf. Sci.* **2008**, *255*, 565-567.
6. Roehlecke, C.; Witt, M.; Kasper, M.; Schulze, E.; Wolf, C. H. A.; Funk, R. *Cells Tissues Organs* **2001**, *168*, 178-187.
7. Khan, M.; Williams, R.; Williams, D. *Biomaterials* **1999**, *20*, 631-637.
8. Khan, M.; Williams, R.; Williams, D. *Biomaterials* **1999**, *20*, 765-772.
9. Biswas, A.; Srikant, P.; Manna, I.; Chatterjee, U.; Dutta Majumdar, J. *Surf. Eng.* **2008**, *24*, 442-446.
10. Komotori, J.; Hisamori, N.; Ohmori, Y. *Wear* **2007**, *263*, 412-418.
11. Sittig, C.; Textor, M.; Spencer, N.; Wieland, M.; Valloton, P. *J. Mater. Sci.* **1999**, *10*, 35-46.
12. Tsong, T.; Astumian, R. *Ann. Rev. Physiol.* **1988**, *50*, 273-290.
13. Winterhalter, M. *Colloids Surf. A* **1999**, *149*, 161-169.
14. Ahlers, M. *Hochaufloesende SECM Messugen an Passivschichten* ; Diploma Thesis, 2009.
15. Payne, K. J.; Veis, A. *Biopolymers* **1988**, *27*, 1749-1760.
16. Casal, H.; Koehler, U.; Mantsch, H. *Biochim. Biophys. Acta* **1988**, *957*, 11-20.
17. Fabian, H.; Schultz, C.; Naumann, D.; Landt, O.; Hahn, U.; Saenger, W. *J. Mol. Biol.* **1993**, *232*, 967-981.
18. Rosenbloom, J.; Harsch, M.; Jimenez, S. *Arc. Biochem. Biophys.* **1973**, *158*, 478-484.
19. Jones, D. Cells and Metals. In *Metals as Biomaterials*; Helsen, J., Breme, H., Eds.; John Wiley & Sons: Chichester, 1998; pp 317-336.
20. Lippert, R.; Lamp, B.; Porter, M. In *Modern Techniques in Applied Molecular Spectroscopy*; Mirabella, F., Ed.; John Wiley & Sons: New York, 1998; pp 83-126.
21. Ratner, B. *Biomaterials Science: An Introduction to Materials in Medicine*; Academic Press: San Diego, 1996.
22. Hulbert, S.; Bokros, J.; Hench, L.; Wilson, J.; Heimke, G. *High Tech Ceramics*; Elsevier Science: Amsterdam, 1987.
23. Helmus, M.; Tweden, K. *Encyclopedic Handbook of Biomaterials and Bioengineering*; Marcel Dekker: New York, 1995.
24. Wang, M. Bioactive Materials and Processing. In *Biomaterials and Tissue*

- Engineering*; Shi, D., Ed.; Springer Verlag: Heidelberg, 2004; pp 1-82.
25. Christ, F.; Suchen, S. *Encyclopedic Handbook of Biomaterials and Bioengineering*; Marcel Dekker: New York, 1995.
  26. Peppas, N.; Langer, R. *Science* **1994**, *263*, 1715.
  27. Chen, J.; Chen, C.; Chen, Z.; Chen, J.; Li, Q.; Huang, N. *J. Biomed. Mater. Res.* **2010**, 341-349.
  28. Tengvall, P. *Titanium in Medicine*; Springer Verlag: Heidelberg, 2001.
  29. Deyl, J.-L.; Miksik, I.; Eckhardt, A. *J Chromatography B* **2003**, *790*, 245-275.
  30. Kuehn, K. Struktur und Biochemie des Kollagens. In *Chemie in unserer Zeit*; Wiley, 1974; Vol. 8, pp 97-103.
  31. Wolf-Brandstetter, C. *Adsorptive immobilisation of collagen type I on titanium surfaces*; 2004.
  32. Bruckner-Tuderman, L.; Höpfner, B.; Hammami-Hauasli, N. *Matrix Biol.* **1999**, 43-54.
  33. Nestler, F.; Hvidt, S.; Ferry, J. *Biopolymers* **1983**, 1747-1758.
  34. Fraser, R. D. B.; MacRae, T. P.; Suzuki, E. *J. Mol. Biol.* **1979**, *129*, 463-481.
  35. Rich, A.; Crick, F. H. C. *Nature* **1955**, *176*, 915-916.
  36. Rich, A.; Crick, F. H. C. *J. Mol. Biol.* **1961**, *3*, 483-506.
  37. Ramachandran, G. N.; Kartha, G. *Nature* **1955**, *176*, 593-595.
  38. Yonath, A.; Traub, W. *J. Mol. Biol.* **1969**, *43* (3), 461-477.
  39. Okuyama, K.; Okuyama, K.; Arnott, S.; Takayanagi, M.; M., K. *J. Mol. Biol.* **1981**, *152*, 427-443.
  40. Bella, J.; Eaton, M.; Brodsky, B.; Berman, H. M. *Science* **1994**, *266*, 75-81.
  41. Kramer, R. Z.; Vitagliano, L.; Bella, J.; Berisio, R.; Mazzarella, L.; Brodsky, B.; Zagari, A.; Berman, H. M. *J. Mol. Biol.* **1998**, *280*, 623-638.
  42. Nimni, M. E.; Harkness, R. D. Molecular structure and functions of collagen. In *Collagen*; E., N. M., Ed.; CRC Press: Boca Raton, 1988; Vol. I, pp 1-78.
  43. Ramachandran, G.; Ramakrishnan, C. In *Biochemistry of Collagen*; Ramachandran, G., Reddi, A., Eds.; Plenum Press: New York, 1976; pp 45-84.
  44. Hulmes, D. J.; Wess, T. J.; Prockop, D. J.; Fratzl, P. *Biophys. J.* **1995**, *68*, 1661-1670.
  45. Fraser, R. D.; Macrae, T. P.; Miller, A.; Suzuki, E. *J. Mol. Biol.* **1983**, *67*, 497-521.
  46. Ottani, V.; Martini, D.; Franchi, M.; Ruggeri, A.; Raspanti, M. *Micron* **2002**, *33*, 587-596.
  47. CAPLUS. *Chemical Abstracts Database*; American Chemical Society, 25.09.2012.
  48. Bronco, S.; Cappelli, C.; Monti, S. *J. Phys. Chem. B* **2004**, *108*, 10101-10112.
  49. George, A.; Veis, A. *Biochemistry* **1991**, *30*, 2372-2377.
  50. Gurdak, E.; Booth, J.; Roberts, C.; Rouxhet, P.; Dupont-Gillain, C. *J. Colloid Interface Sci.* **2006**, *302*, 475-484.
  51. Reohlecke, C.; Witt, M.; Kasper, M.; Schulze, E.; Wolf, C.; Hofer, A.; Funk,

- R. *Cells Tissues Organs* **2001**, *168*, 178-187.
52. Stadlinger, B.; Piling, E.; Huhle, M.; Mai, R.; Bierbaum, S.; Bernhardt, R.; Scharnweber, D.; Kuhlisch, E.; Hempel, U.; Eckelt, U. *J. Biomed. Mater. Res. B* **2007**, *83B*, 222-231.
  53. Stadlinger, B.; Piling, E.; Mai, R.; Bierbaum, S.; Bernhardt, R.; Scharnweber, D.; Eckelt, U. *J. Mater. Sci.* **2008**, *19*, 1043-1049.
  54. Kamata, H.; Suzuki, S.; Tanaka, Y.; Tsutsumi, Y.; Doi, H.; Nomura, N.; Hanawa, T.; Morijama, K. *Materials Transactions* **2011**, *52*, 81-89.
  55. Roessler, S.; Scharnweber, D.; Worch, H. *J. Mater. Sci. Let.* **1999**, *18*, 557-579.
  56. Roessler, S.; Scharnweber, D.; Wolf, C.; Worch, H. *Journal of adhesion Science and Technology* **2000**, *14*, 453-465.
  57. He, J.; Huang, T.; Gan, L.; Zhou, Z.; Jiang, B.; Wu, Y.; Wu, F.; Gu, Z. *J. Biomed. Mater. Res.* **2012**, 1706-1715.
  58. Baker, H.; Merschrod, E.; Poduska, K. *Langmuir* **2008**, *24*, 2970-2972.
  59. Graeve, T. Coagulating collagen and means for preparing same. 2011-102011011092, Feb 09, 2012.
  60. Hu, S.; Zhao, H.; Wang, G.; Cao, C.; Liu, H.; Li, W.; Yang, X. *Gongxueban* **2010**, *40*, 67.
  61. Fullana, M.; Wnek, G. *Drug Delivery Transl. Res.* **2012**, *2*, 313-322.
  62. Achilli, M.; Mantovani, D. *Polymers* **2010**, *2*, 664-680.
  63. Hartman, O.; Zhang, C.; Adams, E.; Farach-Carson, M.; Petrelli, N.; Chase, B.; Rabolt, J. *Biomacromol.* **2009**, 2019-2032.
  64. Krishnamoorthy, G.; Krithica, N.; Sehgal, P.; Mandal, A.; Sadulla, S. *Trans. Indian Inst. Med.* **2011**, *64*, 199-204.
  65. Huang, J.; Cebe, P.; Kaplan, D. *Macromol. Rapid Commun.* **2009**, 336-344.
  66. Nose, M. *Pathol. Int.* **2011**, 619-629.
  67. Asquith, D.; Miller, A.; Reilly, J.; Kerr, S.; Welsh, P.; Sattar, N.; McInnes, I. *Ann. Rheum. Dis.* **2011**, 2225-2228.
  68. Tompkins, H. G.; Irene, E. A. *Handbook of Ellipsometry*; Willian Andrew Inc.: Norwich, 2005.
  69. Fujiwara, H. *Spectroscopic Ellipsometry - Principles and Application*; John Wiley & Sons: New York, 2007.
  70. Hinds instruments. <http://www.hindinstruments.com/knowledge-center/technology-primer/pem100photoelastic-modulation/principles-of-operation/> (accessed 2012).
  71. Stuart, B. In *Infrared Spectroscopy: Fundamentals and Applications*; John Wiley & Sons: New York, 2004; pp pp. 1-pp. 1.
  72. Guenzler, H.; Gremlich, H. H. *IR Spectroscopy - An Introduction*; Wiley VCH: Weinheim, 2002.
  73. Greenler, R. *J. Chem. Phys.* **1966**, *44*, 310-315.
  74. Greenler, R. *J. Chem. Phys.* **1969**, *50*, 1963-1968.
  75. Moskovits, M. *J. Chem. Phys.* **1982**, *77*, 4408-4416.
  76. Hansen, W. *J. Opt. Soc. Am.* **1968**, *58*, 380-390.
  77. Golden, W.; Dunn, D.; Overend, J. *J. Catal.* **1981**, *71*, 395.

78. Knoll, W.; Philpott, M.; Golden, W. *J. Chem. Phys.* **1982**, *77*, 219.
79. Golden, W.; Dunn, D.; Overend, J. *J. Catalysis* **1981**, *71*, 395-404.
80. Buffeteau, T.; Desbat, B.; Turlet, J. *Microchim. Acta* **1988**, *2*, 23-26.
81. Buffeteau, T.; Desbat, B. *J. Appl. Spectrosc.* **1991**, *45*, 380-389.
82. Zamlynny, V.; Zwasizza, I.; Lipkowski, J. *Langmuir* **2003**, *19*, 132-145.
83. Zamlynny, V.; Zawisza, I.; Lipkowski, J. *Langmuir* **2003**, *19*, 132-145.
84. Fringeli, U. *Membrane Spectroscopy*; Springer Verlag: New York, 1981.
85. Torii, H. *Spectroscopy of Biomolecules*; John Wiley & Sons: Chichester, 1996.
86. Jakobsen, R.; Wasacz, F.; Brasch, J.; Smith, K. *Biopolymers* **1986**, *25*, 639-654.
87. Wasacz, F.; Olinger, J.; Jakobsen, R. *Biochemistry* **1987**, *26*, 1464-1470.
88. Yamamoto, T.; Tasumi, M. *Can. J. Spectrosc.* **1988**, *7*, 133-137.
89. Yamamoto, T.; Tasumi, M. *J. Mol. Struct.* **1991**, *242*, 235-244.
90. Jackson, M.; Mantsch, H. *Biochim. Biophys. Acta* **1991**, *1078*, 231-235.
91. Jackson, M.; Mantsch, H. *Biochim. Biophys. Acta* **1992**, *1118*, 139-143.
92. Seshadri, S.; Oberg, K.; Fink, A. *Biochemistry* **1994**, *33*, 1351-1355.
93. Stuart, B. *Biological Applications of Infrared Spectroscopy*; John Wiley & Sons: New York, 1994.
94. Arrondo, J.; Muga, A.; Castresana, J.; Goni, F. *Prog. Biophys. Mol. Biol.* **1993**, *59*, 23-56.
95. Mendelsohn, R.; Moore, D. *Chem. Phys. Lipids* **1998**, *96*, 141-157.
96. Byler, D.; Susi, H. *Biopolymers* **1986**, *25*, 469-487.
97. Surewicz, W.; Mantsch, H. *Biochim. Biophys. Acta* **1988**, *952*, 115-130.
98. Jackson, M.; Haris, P.; Chapman, D. *J. Mol. Struct.* **1989**, *214*, 329-355.
99. Mantsch, H.; Casal, H.; Jones, R. *Adv. Spectrosc.* **1986**, *13*, 1-46.
100. Surewicz, W.; Mantsch, H.; Chapman, D. *Biochemistry* **1993**, *32*, 389-394.
101. Dong, A.; Huang, P.; Caughey, W. *Biochemistry* **1990**, *29*, 3303-3308.
102. Lazarev, Y.; Grishkovskii, B.; Khromova, T. *Biopolymers* **1985**, *24*, 1449-1478.
103. Eliades, G.; Palaghias, G.; Vougiouklakis, G. *Dent. Mater.* **1997**, *1997*, 24-33.
104. Nullmeier, M. *Strukturanalyse von adsorbierten Lipidschichten auf Gold und titanmodifizierten Goldoberflaechen*; Diploma Thesis, 2007.
105. Blodgett, K. *J. Am. Chem. Soc.* **1934**, *56*, 495.
106. Langmuir, I.; Schaefer, V. *J. Am. Chem. Soc.* **1938**, *60*, 1351-1360.
107. Ruediger, C.; Maglia, F.; Leonardi, S.; Sachsenhauser, M.; Sharo, I.; Paschos, O.; Kunze, J. *Electrochim. Acta* **2012**, 1-9.
108. Hahn, R.; Ghicov, A.; Salonen, J.; Lehto, V.-P. *S. P. Nanotechnology* **2007**, *18*, 105604/1-105604/4.
109. Magneli, A. *Nature* **1950**, *165*, 356-357.
110. Hahn, R.; Schmidt-Stein, F.; Salonen, J.; Thiemann, S.; Song, Y.; Kunze, J.; Lehto, V.-P.; Schmuki, P. *Angew. Chem. Int. Ed.* **2009**, *48*, 7236-7239.

111. Broch, L.; Johann, L.; N., S.; Zimmer, A.; Beck, R. *Rev. Sci. Instrum.* **2007**, *78*, 064101/1-064101/6.
112. v.1.33 *Delta Psi Software, Software Database*; Jobin Yvon Horiba.
113. Leonard, D. W.; Meek, K. M. *Biophys. J.* **1997**, *72*, 1382-1387.
114. Singh, B. *Infrared Analysis of Peptides and Proteins*; American Chemical Society: Washington, D.C., 2000.
115. Dickertmann, D.; Koppitz, F.; Schultze, J. *Electrochim. Acta* **1976**, *21*, 967-971.
116. Manesse, M.; Sanjines, R.; Stambouli, V.; Jorel, C.; Pelissier, B.; Pisarek, M.; Boukherroub, R.; Szunerits, S. *Langmuir* **2009**, 8036-8041.
117. Wink, T.; van Zuilen, S.; Bult, A.; van Bennekom, W. *Anal. Chem.* **1998**, 827-832.
118. Fringeli, U. *Z. Naturforsch.* **1976**, *32*, 20-45.
119. Kokubo, T.; Takadama, H. *Biomaterials* **2006**, *27*, 2907-2915.
120. Bellamy, L. *The Infrared Spectra of Complex Molecules*. Chapman and Hall: London, 1975; p 433 pp.
121. Nullmeier, M.; Koliwer-Brandl, H.; Kelm, S.; Zaegel, P.; Koch, K.; Brand, I. *Chem Phys Chem* **2011**, *12*, 1066-1079.
122. Kunze, J.; Leitch, J.; Schwan, A.; Faragher, R.; Naumann, R.; Schiller, S.; Knoll, W.; Dutcher, J.; Lipkowski, J. *Langmuir* **2006**, *22*, 5509-5519.
123. Hianik, T. In *Bioelectrochemistry*; Bartlett, P., Ed.; John Wiley & Sons: Chichester, 2008; pp 87-156.
124. Mady, M. *J. Biosci. Bioeng.* **2007**, 144-148.
125. Kim, H.; Nakamura, F.; Lee, W.; Hong, C.; Pérez-Sala, D.; McCulloch, C. *Exp. Cell Res.* **2010**, 1829-1844.
126. Ghannam, M.; Madi, M.; Khalil, W. *Biophys. Chem.* **1990**, 31-40.
127. Horton, M.; Reich, C.; Gast, A.; Raedler, J.; Nickel, B. *Langmuir* **2007**, 6263-6269.
128. Lu, M.; McCarron, R.; Jacobson, B. *J. Cell Sci.* **1992**, 873-883.
129. MacPhail, R.; Strauss, H.; Snyder, R.; Elliger, C. *J. Phys. Chem.* **1984**, 334-341.
130. Tullini, F.; Nivelli, G.; Fusina, L. *J. Mol. Struct.* **1994**, 81-90.
131. Knapp, D.; Brunschwig, B.; Lewis, N. *J. Phys. Chem.* **2011**, 16389-16397.
132. Bin, X.; Horswell, S.; Lipkowski, J. *Biophys J* **2005**, *89*, 592-604.
133. Bin, X.; Zawisza, I.; Goddard, J.; Lipkowski, J. *Langmuir* **2005**, *21*, 330-347.
134. de Almeida, R.; Loura, L.; Prieto, M. *Chem. Phys. Lipids* **2009**, *157*, 61-77.
135. Zawisza, I.; Wittstoc, G.; Boukherroub, R.; Szunerits, S. *Langmuir* **2008**, 3922-3929.
136. Bard, A.; Faulkner, L. *Electrochemical Methods*; John Wiley & Sons: New Delhi, 2004.
137. *660a, ChI Software*; Ch Instruments.
138. Buffeteau, T.; Desbat, B.; Turlet, J. *Appl. Spectrosc.* **1991**, *45*, 380-389.
139. Gericke, A.; Moore, D.; Erukulla, R.; Bittman, R.; Mendelsohn, R. *J. Mol. Struct.* **1996**, *379*, 227-239.

140. Cameron, D.; Casal, H.; Mantsch, H.; Boulanger, Y.; Smith, I. *Biophys. J.* **1981**, *35*, 1-16.
141. Dluhy, A.; Mendelsohn, H.; Casal, H.; Mantsch, H. *Biochemistry* **1983**, *22*, 1170-1170.
142. Sunder, S.; Cameron, D.; Mantsch, H.; Bernstein, H. *Can. J. Chem.* **1978**, *56*, 2121-2126.
143. Sunder, S.; Mendelsohn, R.; Berntsein, H. *Chem. Phys. Lipids* **1976**, *17*, 456-465.
144. Nullmeier, M. *Supramolekulare Strukturveraenderungen in asymmetrischen Lipiddoppelschichten*; PhD Thesis: Oldenburg, 2011.
145. Brand, I.; Nullmeier, M.; Klüner, T.; Jogireddy, R.; Christoffers, J.; Wittstock, G. *Langmuir* **2010**, *26*, 4554.

## 7 Own Publications

M. Ahlers, I. Brand, N. Stein, „*Behavior of a collagen film exposed to electric fields self-assembled on a polycrystalline gold electrode surface*“, J. Electroanal. Chem., **in progress**

### Oral Presentations

- “*Heterogeneous Distribution of Reactivity at the Passive Film of the Biphasic Ti Alloy Ti6Al7Nb*”

Michael Ahlers, Sascha E. Pust, Martina Nullmeier, Dieter Scharnweber, Izabella Zawisza, Gunther Wittstock  
Electrochemistry – Crossing Boundaries, Giessen, Germany, October 6-8, 2008

- “*Potential Dependent Behaviour of Thin Collagen Films on Gold Surfaces*”

Michael Ahlers, Izabella Brand, Nicolas Stein  
BES 2011, XXI International Symposium on Bioelectrochemistry and Bioenergetics, Cracow, May 8-12, 2011

- “*Electric Field Induced Changes in a Protein Film Adsorbed on a Gold Surface – A Model Study*”

Michael Ahlers, Izabella Brand, Nicolas Stein  
62<sup>nd</sup> Annual ISE Meeting, Niigata, Japan, September 11-16, 2011

## Poster Presentations

- *“Heterogeneous Distribution of Reactivity at the Passive Film of the Biphase Ti Alloy Ti6Al7Nb”*

Michael Ahlers, Sascha E. Pust, Dieter Scharnweber, Gunther Wittstock

5<sup>th</sup> Kurt Schwabe Symposium, Erlangen, Germany, May 24-28, 2009

- *“Investigation on the Adsorption of Collagen on Titania Model Surfaces by Means of PM IRRAS “*

Michael Ahlers, Martina Nullmeier, Izabella Brand, Gunter Wittstock

4<sup>th</sup> International Workshop on Vibrational Spectroscopy of Thin Films, Potsdam, Germany, June 3-5, 2009

- *“Investigation on the Adsorption of Collagen on Titania Model Surfaces by Means of PM IRRAS”*

Michael Ahlers, Martina Nullmeier, Izabella Brand, Gunter Wittstock

Bunsentagung 2010, Bielefeld, Germany, May 13-15, 2010

- *“Electrochemical studies of collagen coatings on the surface of Au electrodes“*

Michael Ahlers, Martina Nullmeier, Izabella Brand, Gunther Wittstock

Electrochemistry 2010, Bochum, Germany, September 13-15, 2010

- *“Electric Field Induced Changes in a Protein Film Adsorbed on a Gold Surface – A Model Study”*

Michael Ahlers, Nicolas Stein, Izabella Brand, Gunther Wittstock

Bunsentagung 2012, Leipzig, Germany, May 17-19, 2012

## 8 Appendix – Abbreviations and Symbols

### Abbreviations

2D, 3D	two/three dimensional
AFM	atomic force microscopy
CCD	charge coupled device
CE	auxiliary electrode (informal: counter electrode)
DMPC	1,2-Dimyristoyl-sn-glycero-3-phosphocholin
d54-DMPC	per deuterated 1,2-Dimyristoyl-sn-glycero-3-phosphocholin
FWHM	full width at half maximum
Gly	glycine, an amino acid
Hyp	hydroxyproline, an amino acid
IR	infrared
IRS	infrared spectroscopy
IRRAS	infrared reflection absorption spectroscopy
OCP	open circuit potential
PBS	phosphate buffered saline
PEM	photoelastic modulator
pH	negative decadic logarithm of the H <sup>+</sup> concentration in a solution
PM-IRRAS	polarization modulation infrared reflection absorption spectroscopy
Pro	proline, an amino acid
RCE	rotating compensator ellipsometer
RE	reference electrode
RTSRCE	real time spectroscopic rotating compensator ellipsometer
SBF	simulated body fluid
SPR	surface plasmon resonance spectroscopy
WE	working electrode

## Symbols

$A$	area
$C$	capacitance
$d$	thickness
$E$	electric field, potential
$E_{x0,y0}$	amplitude of the electric field
$\mathbf{E}$	electric field vector
$f$	frequency
$F$	phase amplitude
$i$	complex number
$I$	intensity
$J_{1,2}$	first and second order Bessel function
$\hat{J}$	Jones matrix
$k$	attenuation coefficient
$\hat{M}$	Mueller matrix
$n$	real part of the refractive index
$N$	complex refractive index
$p$	propagation number
$r$	reflectivity coefficient
rt	room temperature
$R$	reflectivity, resistance
$\hat{R}$	rotation matrix
$S$	Stokes vector
$t$	time, transmission coefficient
$T$	transmittance, temperature
$\alpha$	angle
$\delta_{x,y}$	initial phase of a wave
$\delta_{PEM}$	phase difference of a PEM
$\delta^r$	phase shift of the electric field after reflection
$\Delta$	phase difference, one of the so called ellipsometric angles
$\varepsilon$	dielectric constant
$\theta$	angle of incidence

$\lambda$	wavelength
$\mu$	magnetic permeability
$\xi$	refraction coefficient
$\psi$	one of the ellipsometric angles
$\omega$	angular frequency, resonance frequency, excitation frequency
$\phi$	azimuth



# Curriculum Vitae

## Michael Ahlers

Date of birth July, 8, 1983  
Place of birth Bremen, Germany  
Nationality German

### Education

1990-1994 Primary school, Habbruegge  
1994-2003 Gymnasium Ganderkesee  
Graduation „Abitur“ (German university entrance qualification)

### Mandatory Military Service

2003-2004

### Graduation

10/2004-09/2006 Philipps University Marburg (Study of Chemistry, till “Vordiplom”)  
10/2006-12/2008 Carl vom Ossietzky Universität Oldenburg (Study of Chemistry)  
01/2009 Graduation: “Diplom Chemiker” (graduate chemist)  
Since 02/2009 PhD student at the Carl von Ossietzky University Oldenburg

Ich versichere hiermit, dass ich diese Arbeit selbstständig verfasst und nur die angegebenen Quellen und Hilfsmittel benutzt habe. Aus der Dissertation ist die zuvor genannte Veröffentlichung hervorgegangen. Die Dissertation hat weder zu Teilen noch in Gänze einer anderen wissenschaftlichen Hochschule zur Begutachtung in einem Promotionsverfahren vorgelegen.

Oldenburg, 20. März 2013

Michael Ahlers